

High-reflectivity Photonic Crystal Membranes for Optomechanical Applications

Simon Bernard, Physics Department
McGill University, Montréal
August 2015

A thesis submitted to McGill University in partial fulfillment of the requirements of the
degree of
Master of Science

© Simon Bernard, 2015

Abstract

Several pursuits in the field of cavity optomechanics rely on an object that is mechanically compliant and highly reflective so that it can be strongly influenced by the radiation pressure exerted by laser light. These requirements are typically at odds, but in principle it is possible to satisfy both by fabricating a photonic crystal (PhC) membrane. By patterning an array of wavelength-scale holes into a ~ 100 -nm-thick silicon nitride (SiN) membrane, for example, we can simultaneously reduce its mass, increase its compliance, and achieve a reflectivity beyond what is possible with an unpatterned membrane alone. The reflectivity enhancement is resonant in nature, and in this case occurs within a few nanometers of a wavelength that is highly sensitive to the geometry of the crystal. To reflect light from our lowest-noise lasers (which can emit only one wavelength) this imposes stringent tolerances on our fabrication. In this thesis, we present a gentle and predictable technique for fabricating a PhC membrane and then iteratively tuning its resonant wavelength by thinning it with hydrofluoric (HF) acid dips, thus relaxing fabrication requirements. We use this technique to create a crystal with a resonance within ~ 0.2 nm of our target wavelength ($\lambda = 1550$ nm). We begin by reporting finite-difference time-domain optical simulations of this structure, focusing in particular on how thinning the membrane and widening the holes should tune its resonant wavelength. We then report a process flow to fabricate an actual ~ 100 -nm-thick SiN PhC membrane, and present preliminary characterization of its normal incidence transmission spectrum. Importantly, we observe a resonance at approximately the predicted wavelength, and successfully demonstrate that it can be tuned from 1565.6 nm (as initially fabricated) to 1550.1 nm with three subsequent HF acid dips. Note our characterization apparatus was assembled to rapidly locate the resonance during fabrication, but it can also place a lower bound on the reflectivity of 31 %. The next step is to position this object in an optical cavity, wherein transmission, reflection, and loss coefficients can be measured with ppm accuracy. This fabrication technique will be of general use to our group as well as others interested in creating silicon nitride structures requiring precisely tuned dimensions.

Abrégé

Plusieurs poursuites dans le domaine de l’optomécanique reposent sur un objet qui est à la fois mécaniquement docile et hautement réfléchissant afin qu’il puisse être fortement influencé par la pression de radiation exercée par la lumière. Ces exigences vont typiquement l’une à l’encontre de l’autre, mais en principe il est possible de les satisfaire conjointement en fabriquant une membrane percée par un cristal photonique. En définissant une maille de trous de l’ordre de la longueur d’onde dans une membrane de nitrure de silicium dont l’épaisseur est de 100 nm, nous pouvons simultanément réduire sa masse, accroître sa flexibilité, et réaliser une réflectivité au-delà de ce qui est possible avec une simple membrane. Cette amélioration de la réflectivité est un phénomène résonant, et dans ce cas se produit dans l’espace de quelques nanomètres autour d’une longueur d’onde qui est très sensible à la géométrie du cristal. Pour refléter la lumière de nos lasers bas bruit (qui émettent une seule longueur d’onde), cela impose des tolérances strictes sur notre fabrication. Dans cette thèse, nous présentons une technique douce et prévisible pour la fabrication d’une membrane percée par un cristal photonique et ensuite régler sa longueur d’onde de résonance en l’amincissement à l’aide d’une baignade dans l’acide fluorhydrique, détendant ainsi les exigences de fabrication. Nous utilisons cette technique pour créer un cristal avec une résonance au sein de ~ 0.2 nm de la longueur d’onde ciblée ($\lambda = 1550$ nm). Nous débutons avec des simulations de la performance optique de cette structure en utilisant la méthode des différences finies dans le domaine temporel. En particulier, nous nous concentrons sur la façon dont l’amincissement de la membrane et l’élargissement des trous devraient affecter sa longueur d’onde de résonance. Nous rapportons ensuite un procédé pour fabriquer une membrane (~ 100 nm d’épaisseur) de nitrure de silicium percée par un cristal photonique, et présentons une caractérisation préliminaire de son spectre de transmission à incidence normale. Nous observons une résonance approximativement à la longueur d’onde prédite, et démontrons avec succès qu’elle peut être réglée de 1565.6 nm (fabriqué initialement) à 1550.1 nm avec trois bains successifs d’acide fluorhydrique. Notez que notre appareil de caractérisation a été assemblé pour localiser rapidement la résonance lors de la fabrication, mais il peut également placer une limite inférieure de 31 % pour la réflectivité. La prochaine étape consiste à positionner cet objet dans une cavité optique, dans laquelle les coefficients de transmission, réflexion, et perte peuvent être mesurés avec une précision ppm. Cette technique de fabrication sera utile pour notre groupe ainsi que d’autres intéressés par la création de structures de nitrure de silicium nécessitant des dimensions précisément réglées.

Acknowledgments

When I arrived at the Sankey Lab, our laboratory was an empty room. My first task under the supervision of Jack was to assemble an Ikea table with Christoph. Jack finished assembling his table before we did, and at that moment I realized I was in the hands of a competent supervisor. On a more serious note, I would like to express my deepest gratitude to Jack for the time and efforts he put in this project. Whether it was in the lab or in the office, Jack has always been willing to help. I learned a great deal from Jack, and working with him has been a privilege.

Thanks to my fellow lab mates, without whom this experience would not have been nearly as enjoyable. To Christoph, for his willingness to always help, and for the good times away at conferences. I take this opportunity to mention that Christoph developed the first iterations for the fabrication of unpatterned membranes, designed the sample holder, and provided assistance when I started fabrication. Thank you Tina for your patience, I must have asked you at least five questions a day over the last two years. I admire your work ethic, and working with you on the silicon fab project was enriching. To Alex, for his enthusiasm and his way of finding a solution to every problem. Alex provided critical help for writing the program interfacing the optical spectrum analyzer. To Abeer, for being great to talk to and always in a good mood. To Max, for his motivation and helpful suggestions. To Vincent for being crazy.

I would like to thank Don, Lino, John, Seddik, Matthieu and Sasa for the McGill clean-room trainings, David for the scanning electron microscope training, as well as Paul and Marie-Hélène from École Polytechnique de Montréal for the electron-beam machine training. Thanks to Yves-Alain Peter and Alireza Mesgar for fruitful discussions.

To my friends Simon and Pericles for the countless laughs. Finally, to the people that matter to me the most: Isabelle, Roxanne, Brigitte and Gilles, thank you. None of this would have been possible without you.

Contents

Abstract	i
Abrégé	ii
Acknowledgments	iii
List of Figures	vii
List of Tables	ix
1 Cavity Optomechanics and Photonic Crystal Membranes	1
1.1 Cavity Optomechanics	1
1.1.1 Introduction	1
1.1.2 Canonical Model for an Optomechanical System	2
1.2 Motivation	6
1.3 Photonic Crystal Membranes	10
1.4 Thesis Outline	11
2 Photonic Crystal Membrane Design via Numerical Simulations	13
2.1 Operating Principles of Meep	13
2.1.1 Solving Maxwell's Equations with the Finite-Difference Time-Domain Method	14
2.1.2 Terminating the Computational Cell with Boundary Conditions	15
2.1.3 Transmission and Reflection Spectra	15
2.2 Parameters Regulating the Computational Cell and the Computational Time	16
2.2.1 Computational Cell	16
2.2.2 Computational Time	18
2.3 Results	19
2.3.1 Frequency Domain	19
2.3.1.1 Square Lattice, 100 nm thick	19
2.3.1.2 Hexagonal Lattice, 100 nm thick	21
2.3.1.3 Hydrofluoric Acid Tuning of the Resonance	23
2.3.1.4 Material Absorption	24

2.3.2	Time Domain	25
3	Photonic Crystal Membrane Fabrication	28
3.1	Fundamentals of Photolithography and Electron Beam Lithography	28
3.2	Process Flow	29
3.2.1	Membrane Fabrication	29
3.2.2	ZEP520A Resist Spin-coating	34
3.2.2.1	Sample Cleaning	34
3.2.2.2	Spin-coating	35
3.2.3	Defining the Photonic Crystal with Electron Beam Lithography	36
3.2.3.1	Optimized Settings	36
3.2.3.2	Mask Files and Sample Preparation	38
3.2.3.3	Procedure	38
3.2.3.4	Development	40
3.2.4	Dry Etching of the Photonic Crystal	40
3.3	Alternative and Improvements	43
4	Photonic Crystal Membrane Optical Characterization	44
4.1	Experimental Setup	44
4.1.1	Beam Shape Control	44
4.1.2	Beam Path	46
4.2	Method	47
4.2.1	Laser Control	48
4.2.2	Graphical User Interface	50
4.2.3	Optical Spectrum Analyzer	52
4.2.4	Photonic Crystal Membrane Mounting	54
4.2.5	Photonic Crystal Membrane Alignment	54
4.3	Data Treatment	55
4.4	Transmission Spectrum of Photonic Crystal Membranes	60
4.4.1	Hexagonal Slab	61
4.4.2	Resonance Tuning	62
5	Conclusions and Outlook	65
	Appendix	66

List of Figures

1.1	Canonical Model for an Optomechanical System	3
1.2	Membrane-in-the-middle Setup	7
1.3	Fano Line Shape	11
1.4	Graphical Overview of Thesis	11
2.1	Computational Cell	17
2.2	Square Lattice Slab Transmission Spectrum	20
2.3	Hexagonal Lattice Slab Transmission Spectrum	22
2.4	Effect of Polarization on Hexagonal Lattice Slab Transmission Spectrum	22
2.5	HF Acid Tuning	23
2.6	Material Absorption	24
2.7	Band Structure and Electric Field Distribution	26
3.1	Fundamentals of Photolithography	29
3.2	Fabrication Process Flow	30
3.3	Front Side Pattern and Back Side Pattern	32
3.4	Sample Holder and KOH Etching	34
3.5	ZEP520A Spin-coating	35
3.6	EBL Parameters	37
3.7	EBL Procedure	39
3.8	Dry Etching Mask	40
3.9	Dry Etching of the PhC	41
3.10	Optical and SEM Characterization of the PhC Membrane	42
4.1	Experimental Setup	45
4.2	Laser Control	49
4.3	Graphical User Interface	51
4.4	OSA Spectrum	52
4.5	OSA Characterization	53
4.6	PhC Membrane Alignment	55
4.7	Data Acquisition	56
4.8	Photodiode Signals	57
4.9	Half-wave Plate Rotation	58

4.10 Dark Voltage	59
4.11 Measured Hexagonal Lattice Slab Transmission Spectrum	61
4.12 Tuning the Spectral Position of the Resonance	63
A.1 Preliminary Reflection Spectrum	66

List of Tables

3.1	Windows RIE Recipe	33
3.2	PhC RIE Recipe	41

Chapter 1

Cavity Optomechanics and Photonic Crystal Membranes

Our research group aims to control the motion of solid mechanical systems with the radiation forces exerted by laser light. Since radiation forces are quite weak (i.e. only $\sim 6.7 \times 10^{-9}$ N/W), it is advantageous to use small, lightweight mechanical elements, that are highly reflective. In this thesis we discuss our efforts to realize a technology that achieves both of these aims, namely photonic crystal (PhC) membranes. In short, by punching an appropriate set of holes in a thin (i.e. ~ 100 -nm-thick) dielectric membrane, we can increase its reflectivity beyond what is possible with a membrane (of any thickness) alone.

The present chapter provides the relevant background information in an effort to motivate the work and put it in the context of the field. In Sec. 1.1 we introduce the field of cavity optomechanics and the basic properties of a canonical model for an optomechanical system. Then, in Sec. 1.2 we motivate the use of high-reflectivity PhC membranes to contribute to the achievement of the goals pursued by our group. In Sec. 1.3 we explain the operating principle of PhC membranes. Finally, we outline the rest of the thesis in Sec. 1.4.

1.1 Cavity Optomechanics

1.1.1 Introduction

Cavity optomechanics is the branch of physics that studies the interaction between radiation pressure from light and the motion of mechanical resonators. This field possesses a number of technological applications ranging from macroscale gravitational wave interferometers to nano- or micro-scale cantilevers used in force sensing [1, 2]. On the other hand, coupling between optical and mechanical degrees of freedom also grants access to a variety of fundamental physical phenomena: radiation forces can be used to laser cool a solid object's motion to the quantum mechanical ground state [3, 4], levitate it [5–7], or partially levitate it to increase its mechanical quality factor [8–10]. Furthermore, the optomechanical interaction

enables the transfer of quantum states between photons of different energies (e.g. a mechanical oscillator could be the bridge between a microwave cavity coupled to a superconducting qubit and an optical cavity) [11–13]. Hence this field simultaneously contributes to the advancement of fundamental knowledge, and to the development of innovative technologies. To understand how radiation forces can affect the motion of a mechanical oscillator and vice versa, we study a generic model for an optomechanical setup in the next section.

1.1.2 Canonical Model for an Optomechanical System

A canonical model for an optomechanical system is a Fabry-Pérot cavity consisting of two parallel highly reflective mirrors, with one mirror being movable as shown in Fig. 1.1a. The movable mirror constitutes the mechanical oscillator whose motion modulates the frequency of the light circulating inside the cavity. This coupling imprints the mechanical element’s motion upon the light leaving the cavity, and conversely, the light circulating inside the cavity applies a radiation force which acts back upon the mechanical element [1]. To begin, we shall determine the power transmission coefficient of the cavity \mathcal{T} which relates the input power P_{in} to the output power P_{out} via $P_{out} = \mathcal{T} \cdot P_{in}$. Obtaining \mathcal{T} will allow us to introduce the relevant parameters that characterize the Fabry-Pérot cavity, and to derive the “mirror-position-dependent” radiation force $F(x)$ acting on the mechanical oscillator. The form of $F(x)$ will give insight on how the phenomena mentioned in Sec. 1.1.1 can be realized, and the intuitive results we obtain from this simple model can be generalized to most other optomechanical systems, regardless of geometry.

First, we assume that the right mirror is fixed (i.e. the right mirror position is $x = 0$) so that the distance separating the two mirrors is L . To obtain \mathcal{T} , we follow the treatment of chapter 7 of Saleh and Teich [14]. The Fabry-Pérot cavity is modeled as a three-layer stack: a left mirror, a propagating medium (i.e. the cavity space), and a right mirror. Each layer is described by a “scattering matrix” \mathbf{S} that relates outgoing electric fields to incoming electric fields, as shown in Fig. 1.1b. The elements of \mathbf{S} are directly related to the physical parameters of the layer. For our 3-layer system, this formalism involves eight fields in total, two of which (the inputs from either end) are specified, and the rest of which need calculating. This translates to a 6-equations 6-unknowns situation (which gets even worse for more elements). A simpler approach is to express each layer in terms of a “transfer matrix” \mathbf{M} , which relates the fields on *either side* of the layer in question. The transfer matrix has the advantage that it can be concatenated for a multilayer system: $\mathbf{M}_{\text{system}} = \mathbf{M}_N \dots \mathbf{M}_2 \cdot \mathbf{M}_1$, where N denotes

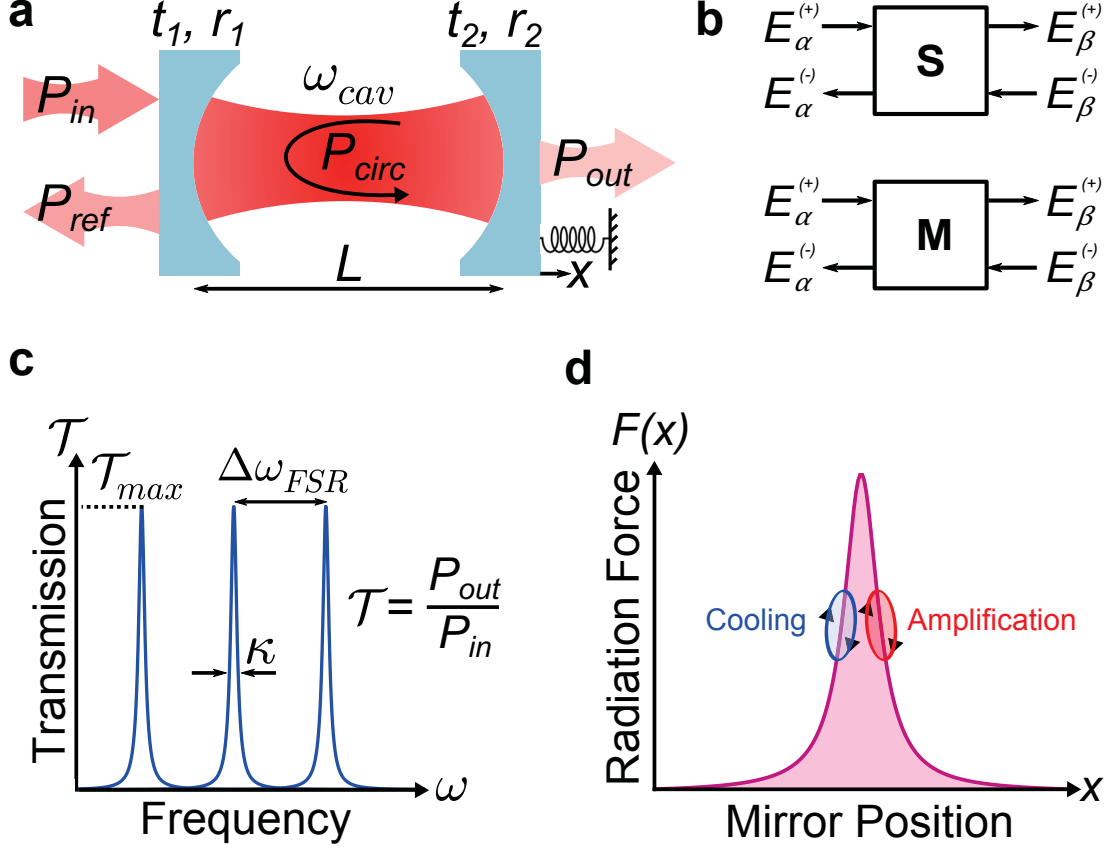


Figure 1.1: Canonical model for an optomechanical system. **a**, A movable mirror of a Fabry-Pérot cavity modulates the frequency of the light circulating inside the cavity, and conversely, the circulating light applies a “back-action” force upon the movable mirror. **b**, The scattering matrix \mathbf{S} relates outgoing electric fields to incoming electric fields. On the other hand, the transfer matrix \mathbf{M} relates the fields on either side of the layer being modeled. \mathbf{M} is a convenient way to treat a multilayer system since it can be cascaded. Its elements are linked to the elements of \mathbf{S} through Eq. 1.2. **c**, Power transmission coefficient of the cavity as a function of drive frequency. The cavity displays a set of equally spaced resonant frequencies. **d**, Position-dependent radiation pressure force acting on the movable mirror. The finite lifetime of the cavity leads to dynamical back-action effects.

the layer number in order of appearance from the left. However, unlike \mathbf{S} , the elements of \mathbf{M} are not intuitively related to the physical parameters of the layer. Fortunately, one can

link the elements of \mathbf{S} to the elements of \mathbf{M} via:

$$\begin{pmatrix} E_\beta^+ \\ E_\beta^- \end{pmatrix} = \mathbf{S} \cdot \begin{pmatrix} E_\alpha^+ \\ E_\alpha^- \end{pmatrix} = \begin{pmatrix} t_{\alpha\beta} & r_{\beta\alpha} \\ r_{\alpha\beta} & t_{\beta\alpha} \end{pmatrix} \cdot \begin{pmatrix} E_\alpha^+ \\ E_\alpha^- \end{pmatrix}, \quad (1.1)$$

$$\begin{pmatrix} E_\beta^+ \\ E_\beta^- \end{pmatrix} = \mathbf{M} \cdot \begin{pmatrix} E_\alpha^+ \\ E_\alpha^- \end{pmatrix} = \frac{1}{t_{\beta\alpha}} \begin{pmatrix} t_{\alpha\beta}t_{\beta\alpha} - r_{\alpha\beta}r_{\beta\alpha} & r_{\beta\alpha} \\ -r_{\alpha\beta} & 1 \end{pmatrix} \cdot \begin{pmatrix} E_\alpha^+ \\ E_\alpha^- \end{pmatrix}. \quad (1.2)$$

The subscript $\alpha\beta$ indicates that a wave is traveling from medium α to medium β (see Fig. 1.1b), and the elements $t_{\alpha\beta}$ ($t_{\beta\alpha}$) and $r_{\alpha\beta}$ ($r_{\beta\alpha}$) are the complex electric field transmission and reflection coefficients for the forward (backward) directions. The superscripts (+) and (−) refer to right- and left-moving waves. For the Fabry-Pérot cavity, we assume that the electric field transmission and reflection coefficients for both mirrors are independent of the propagation direction (forward or backward). Therefore, the physical parameters describing mirror i ($i = 1, 2$) are $t_i = t_{\alpha\beta} = t_{\beta\alpha}$ and $r_i = r_{\alpha\beta} = r_{\beta\alpha}$. The propagating medium is characterized by a refractive index n and length L so that the phase accumulated by the electric field after a cavity trip from left to right is $\phi = nk_0L$, where k_0 is the vacuum wavenumber. If we further assume lossless mirrors, we have $|t_i|^2 + |r_i|^2 = 1$, and $\arg\{t_i\} - \arg\{r_i\} = \pm\frac{\pi}{2}$. Under these assumptions, the Fabry-Pérot cavity is described by the transfer matrix

$$\mathbf{M}_{\text{Fabry-Pérot}} = \mathbf{M}_{\text{mirror2}} \cdot \mathbf{M}_{\text{propagation}} \cdot \mathbf{M}_{\text{mirror1}} \quad (1.3)$$

$$= \begin{pmatrix} \frac{1}{t_2^*} & \frac{r_2}{t_2} \\ \frac{r_2^*}{t_2} & \frac{1}{t_2} \end{pmatrix} \cdot \begin{pmatrix} e^{i\phi} & 0 \\ 0 & e^{-i\phi} \end{pmatrix} \cdot \begin{pmatrix} \frac{1}{t_1^*} & \frac{r_1}{t_1} \\ \frac{r_1^*}{t_1} & \frac{1}{t_1} \end{pmatrix}. \quad (1.4)$$

As can be seen in Eq. 1.2, the lower-right element of a transfer matrix, $\mathbf{M}^{(22)}$, relates the rightward outbound light to the rightward inbound light, meaning the power transmission coefficient for the whole cavity (see Eq. 1.4) is the absolute square of the inverse of the element $\mathbf{M}_{\text{Fabry-Pérot}}^{(22)}$:

$$\mathcal{T} = \left| \frac{1}{\mathbf{M}_{\text{Fabry-Pérot}}^{(22)}} \right|^2 = \frac{|t_1 t_2|^2}{|1 - r_1 r_2 e^{2i\phi}|^2}, \quad (1.5)$$

where we picked the phase associated with mirror reflection to be π (to produce our “usual” intuition about reflected waves inverting at mirror surfaces) so that the phase associated with mirror transmission is $\frac{\pi}{2}$. Defining the maximum value $\mathcal{T}_{\max} = \frac{(1-|r_1|^2)(1-|r_2|^2)}{(1-|r_1 r_2|^2)}$ and a new quantity $\mathcal{F} = \frac{\pi\sqrt{|r_1 r_2|}}{1-|r_1 r_2|}$, \mathcal{T} is written

$$\mathcal{T} = \frac{\mathcal{T}_{\max}}{1 + \left(\frac{2\mathcal{F}}{\pi}\right)^2 \sin^2 \phi}. \quad (1.6)$$

The quantity \mathcal{F} is called the “cavity finesse”, a strictly increasing function of the product $r_1 r_2$. As we will see below, \mathcal{F} is proportional to the lifetime τ of the energy inside the cavity. Equation 1.6 is a periodic function of ϕ with period π . Writing $\phi = nk_0 L = \frac{\omega}{c} L$, \mathcal{T} is plotted versus ω in Fig. 1.1c. The periodic nature of \mathcal{T} translates to the cavity admitting a set of equally spaced resonant frequencies which are given by $\omega_c = q \pi \frac{c}{L}$, where q is an integer labeling a longitudinal mode. The spacing between resonant frequencies is called the free spectral range: $\Delta\omega_{FSR} = \frac{\pi c}{L}$. The full width at half maximum of each resonance is $\kappa = \frac{\Delta\omega_{FSR}}{\mathcal{F}}$, where $\kappa = \tau^{-1}$ is the energy decay rate of the cavity.

To derive the radiation force $F(x)$ acting on the movable mirror, we assume that the cavity is driven by constant amplitude monochromatic light of frequency ω_L near the q^{th} resonance. In this case, the argument of the sine in Eq. 1.6 takes the form $\phi = q\pi \frac{\omega_L}{\omega_c}$, and Taylor expanding $\sin^2 \phi$ near $\frac{\omega_L}{\omega_c} = 1$ yields

$$\mathcal{T} \simeq \frac{\mathcal{T}_{max}}{1 + \left(\frac{2\mathcal{F}}{\pi}\right)^2 \left(\frac{\pi q}{\omega_c}\right)^2 (\omega_L - \omega_c)^2} = \frac{\mathcal{T}_{max}}{1 + \left(\frac{2\mathcal{F}}{\Delta\omega_{FSR}}\right)^2 \Delta^2} = \frac{\mathcal{T}_{max}}{1 + \left(\frac{2\Delta}{\kappa}\right)^2}, \quad (1.7)$$

where we have introduced the detuning $\Delta = \omega_L - \omega_c$. Assuming a high-finesse cavity, (i.e. $\frac{\Delta\omega_{FSR}}{\kappa} \gg 1$), this approximation is valid over the full line shape of the q^{th} resonance. Now, if we allow the end mirror to move, the resonant frequency of the cavity depends on the position of the latter:

$$\omega_c(x) = \omega_c + \partial_x \omega_c(x) x + \dots \quad (1.8)$$

As a result, $\Delta \rightarrow \Delta - gx$, where $g = \partial_x \omega_c(x)$ is the “linear optomechanical coupling”, and Eq. 1.7 becomes

$$\mathcal{T}(x) = \frac{\mathcal{T}_{max}}{1 + \left(\frac{2(\Delta - gx)}{\kappa}\right)^2}. \quad (1.9)$$

Ultimately, we want to use $\mathcal{T}(x)$ to estimate the radiation force applied on the movable mirror. The force is $\frac{2P_{circ}}{c}$, where P_{circ} is the power circulating inside the cavity. Given P_{circ} incident on the right hand mirror and a transmission coefficient t_2 , $P_{out} = |t_2|^2 P_{circ}$ so that $P_{circ} = \frac{1}{|t_2|^2} \mathcal{T} \cdot P_{in}$ and

$$F(x) = \frac{2P_{in}}{c|t_2|^2} \times \frac{\mathcal{T}_{max}}{1 + \left(\frac{2(\Delta - gx)}{\kappa}\right)^2}. \quad (1.10)$$

Figure 1.1d shows the line shape of $F(x)$. In the next paragraph, we inspect $F(x)$ to link this canonical model to some of the physical effects mentioned in Sec. 1.1.1.

Cooling of the mechanical oscillator can be understood in terms of the finite lifetime τ of the cavity which prevents $F(x)$ from responding instantaneously to mirror displacements [15]. Suppose that the mirror sits on the red-detuned side of $F(x)$ (see Fig. 1.1d). Thermal fluctuations (or an external drive) move the mirror around its equilibrium position. When the mirror is displaced toward the optical resonance, $F(x)$ should increase as light enters the cavity, but will be smaller than expected because of the time it takes for the circulating power to build up. Alternatively, when the mirror is displaced away from the resonance, it takes time for the circulating power to leak out so that $F(x)$ is larger than expected. After a complete cycle, the work done on the mirror (i.e. the area of the loop) is negative, causing damping, as illustrated in Fig. 1.1d. This damping reduces the average thermal energy without adding significant additional fluctuations, lowering the effective temperature. Placing the mechanical element on the blue-detuned side of the resonance gives rise to anti-damping.

The dependence of the radiation pressure force on x also modifies the spring constant of the mechanical oscillator. The potential for the mechanical motion is

$$V(x) = \frac{m\Omega_m^2}{2}x^2 + V_{rad}(x), \quad (1.11)$$

where m is the oscillator’s mass, Ω_m is the unperturbed mechanical frequency, and $V_{rad}(x)$ is the radiation pressure potential. In the simplest case where the cavity responds adiabatically to the mirror motion, $F(x) = -\partial_x V_{rad}$. The modified spring constant is

$$k_{eff} = \partial_x^2 V(x_0) = m\Omega_m^2 - \partial_x F(x_0) \quad (1.12)$$

where x_0 is a position such that $\partial_x V(x_0) = 0$. The term $-\partial_x F(x_0)$ is the “optical spring” [1], which has been used to tune the frequency of mechanical elements by orders of magnitude [9] (even for gram-scale mirrors [16]). The full optical spring is derived using a set of differential equations for the light in the cavity and motion [1], but the physics is essentially the same.

1.2 Motivation

Section 1.1 above describes a few of the basic new functionalities that are possible in the field of optomechanics. In the context of our laboratory, one way to achieve this is to use the “membrane-in-the-middle” setup, where a dielectric membrane of sub-wavelength thickness is placed inside an optical cavity instead of having the end mirror move, as shown

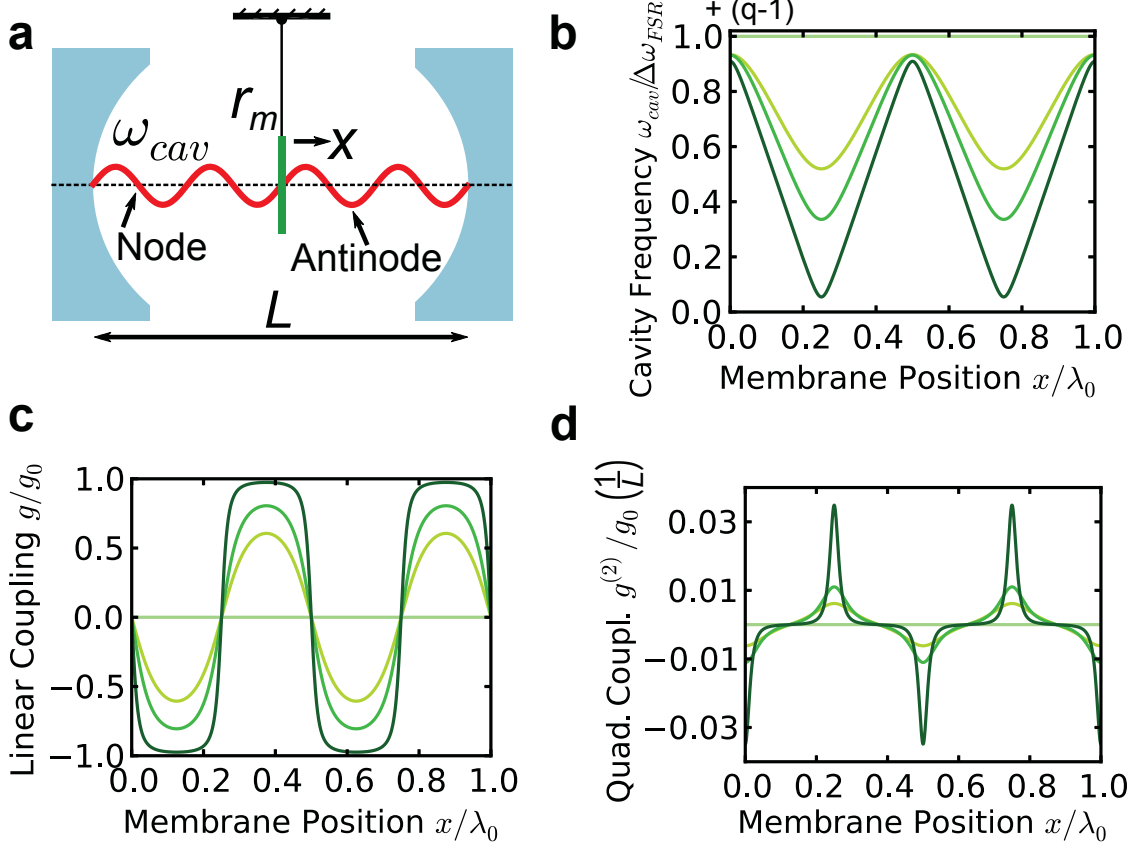


Figure 1.2: “Membrane-in-the-middle” setup, cavity detuning, and optomechanical coupling. **a**, Schematic of the membrane-in-the-middle setup, where a dielectric membrane of sub-wavelength thickness and reflectivity $|r_m|^2$ is placed inside a high-finesse cavity. **b**, The position of the membrane modulates the resonant frequency of the cavity. Different curves correspond to different membrane reflectivities: lightest to darkest, $|r_m|^2 = \{0, 0.37, 0.65, 0.95\}$. Increasing $|r_m|^2$ affects more the cavity frequency, which translates to a greater optomechanical coupling. **c**, The linear optomechanical coupling increases with membrane reflectivity. **d**, Near cavity field antinodes, the membrane experiences an optical spring characterized by the quadratic optomechanical coupling, which also increases with membrane reflectivity.

in Fig. 1.2a. The displacement of the membrane modulates the cavity frequency ω_{cav} , and the cavity field in turn influences the motion of the mechanical resonator [17]. With a transfer matrix treatment similar to Sec. 1.1.2, and assuming a lossless system with perfectly reflective mirrors, one can show that the scaled cavity resonant frequency in the presence of a dielectric membrane near its center is given by [18]

$$\frac{\omega_{cav}}{\Delta\omega_{FSR}} = \frac{1}{\pi} \left(-\arg\{r_m\} + \arccos\{-|r_m| \cos(2k_0 x)\} \right), \quad (1.13)$$

where k_0 is the empty cavity resonant wavenumber, x is the membrane's displacement with respect to the center of the cavity, and r_m is the membrane's electric field reflection coefficient: [18]

$$r_m = \frac{(n_m^2 - 1) \sin(k_0 n_m d)}{2in \cos(k_0 n_m d) + (n_m^2 + 1) \sin(k_0 n_m d)}. \quad (1.14)$$

The refractive index of the dielectric membrane is n_m , and its thickness is d . Figure 1.2b shows the resonant frequency for the $q = 10^5$ longitudinal mode of a laser driven ($\lambda_0 = 1550$ nm) cavity of length $L = 7.75$ cm with a membrane thickness $d = 50$ nm. The different membrane power reflectivities $|r_m|^2$ are obtained by varying the refractive index in Eq. 1.14. Since we are looking at the q^{th} mode of the cavity, the scaled (by the empty cavity free spectral range) resonant frequency is given by $\frac{\omega_{cav}}{\Delta\omega_{FSR}} + (q - 1)$. When the membrane sits at a node of the cavity field, the resonant frequency approaches the empty cavity frequency. This is the case because the field is minimal inside the membrane so it does not perturb the empty cavity mode. The perturbed curves do not touch the empty cavity horizontal curve due to the finite thickness of the membrane. Note that if we were instead looking at an odd cavity mode $q = 2l + 1$ where $l \in \mathbb{Z}$, the curves would be shifted by 0.25 along the x axis.

As the membrane reflectivity is increased, it pulls down the cavity frequency. Notice that the slope $\partial_x \omega_{cav}$ (i.e. the “linear” optomechanical coupling) is larger for higher reflectivity. In this case, the expression for the linear optomechanical coupling is

$$g = \partial_x \omega_{cav} = -\frac{2k_0 |r_m| \sin(2k_0 x)}{\pi \sqrt{1 - |r_m|^2} \cos^2(2k_0 x)} \times \Delta\omega_{FSR}. \quad (1.15)$$

Figure 1.2c shows the linear optomechanical coupling scaled by the “maximum possible” optomechanical coupling that could be achieved with an infinitely-reflective membrane (making a cavity of length $L/2$), $g_0 = 2\omega_0/L$, where ω_0 is the empty cavity resonant frequency. In addition, when the membrane is positioned near a cavity field antinode g vanishes, and the so-called “quadratic” optomechanical coupling dominates:

$$g^{(2)} = \partial_x^2 \omega_{cav} = \frac{4k_0^2 |r_m| (|r_m|^2 - 1) \cos(2k_0 x)}{\pi (1 - |r_m|^2 \cos^2(2k_0 x))^{\frac{3}{2}}} \times \Delta\omega_{FSR}. \quad (1.16)$$

Figure 1.2d reveals that increasing the membrane reflectivity leads to a more pronounced curvature (described by $\partial_x^2 \omega_{cav}$) of ω_{cav} , meaning the membrane is drawn by a stiffer optical spring (the electromagnetic energy in the cavity is $U(x) \propto \partial_x^2 \omega_{cav} x^2$) toward the cavity field antinodes. This enables tuning of the membrane's mechanical frequency, which can lead to an enhancement of its mechanical quality factor, a figure of merit in sensing applications [9, 10].

Furthermore, quadratic coupling allows for a direct measurement of the membrane’s average *squared* position (i.e. its energy) [17, 19], so that higher reflectivity is desirable if one wishes to search for evidence of quantization of the membrane’s mechanical energy.

Another direction pursued in our laboratory is to explore a strong “dissipative” coupling, predicted by Ref. [20]. In this case, the mechanical element’s motion modulates the rate at which light leaks into and out of the cavity. This coupling has only recently been explored in detail by one group experimentally using a different geometry [21]. In our case, since a high-reflectivity membrane can more strongly affect the cavity modes, its motion could be engineered to strongly modulate the cavity energy decay rate by shuffling the cavity mode back and forth between mirrors of different reflectivities. This type of coupling allows for a novel cooling scheme of the mechanical oscillator in which the ground state could be reached outside of the so-called “good cavity” limit $\kappa \ll \Omega_m$ [20].

Importantly, all optomechanical pursuits will benefit from a higher-reflectivity mechanical element. For example, Ref. [22] suggests that an array of several dielectric membranes carefully positioned within an optical cavity could localize the cavity mode within the array, pushing outward on a collective “breathing” mode with sufficient strength that a single photon could detune the cavity frequency enough to reject a subsequent photon. In essence the photons would “bounce off” one another. The number of membranes required to achieve this level of localization is quite high (> 5), set primarily by the reflectivity that can be achieved with each dielectric membrane ($\sim 15\%$). On the other hand, if the reflectivity of the membranes exceeds 99 %, only ~ 5 membranes (i.e. a much more feasible technical challenge) would be enough to approach the single-photon strong coupling regime. Because this unprecedented single-photon nonlinearity would be based on radiation forces (rather than, e.g., an atomic resonance), it could be engineered to occur at an arbitrary design wavelength, which is an outstanding challenge in the photonics and quantum information communities. Within this regime, it would also be possible to generate non-classical mechanical states [22, 23].

At this point, a natural question that arises is how can one increase the reflectivity of the mechanical element while ensuring it remains mechanically compliant and lightweight. One way to do this is to pattern a lattice of holes into a thin free-standing dielectric membrane to realize a surface that is much more reflective (e.g. $> 99\%$ at the design wavelength, [24–27])

than can be achieved with just a dielectric membrane (typically $\sim 15\%$). Furthermore, such a patterned membrane retains its mechanical properties [28]. Similar devices have been realized for other applications [29, 30], but PhC membranes remain novel for optomechanics [24, 25, 28] because they can in principle satisfy the simultaneous requirements of high reflectivity and high mechanical compliance. The only other objects that possess comparable reflectivities are Bragg mirrors, formed by stacking multiple layers of alternating materials with varying refractive index. These objects are rigid, heavy, and generally have a high level of mechanical dissipation. In the next section, we introduce the basic features of the PhC membrane.

1.3 Photonic Crystal Membranes

A photonic crystal is a low-loss medium displaying a periodic refractive index [31]. Reflections and refractions from interfaces formed by the modulated refractive index give rise to photonic band gaps, a range of frequencies for which electromagnetic waves cannot propagate along certain directions in the crystal, allowing for control and manipulation of light [31]. PhC membranes consist of a dielectric layer of finite thickness into which a 2D periodic refractive index is introduced [32, 33]. This can be achieved by punching holes into the high-index dielectric layer, as shown in the inset of Fig. 1.3. PhC membranes support “guided modes”, which have frequencies below the “light line” $\omega = c|\mathbf{k}_{\parallel}|$, where \mathbf{k}_{\parallel} is the wave vector in the plane of the slab. Guided modes decay exponentially away from the slab, and do not couple to the continuum of free-space modes [31, 33]. Contrary to guided modes, PhC membranes also support “leaky modes” (or guided resonances) with frequencies $\omega > c|\mathbf{k}_{\parallel}|$, that are not as strongly confined to the slab. As a result, leaky modes can couple to external radiation incident on the slab, producing Fano line shapes in the transmission and reflection spectra of the PhC membrane [33–35], as shown in Fig. 1.3. The normalized Fano line shape is described by [36]

$$\mathcal{L}(\xi) = \frac{1}{1+f} \frac{(\xi+f)^2}{1+\xi^2}, \quad (1.17)$$

where f is a dimensionless Fano factor, and $\xi = \frac{2(\omega-\omega_r)}{\gamma}$ with resonant frequency ω_r and linewidth γ . The quality factor of the resonance is $Q = \frac{\omega_r}{\gamma}$. In Sec. 2.3.2, we explore in greater detail the cause of the Fano line shape by inspecting the electric field distribution in the PhC slab in the time domain.

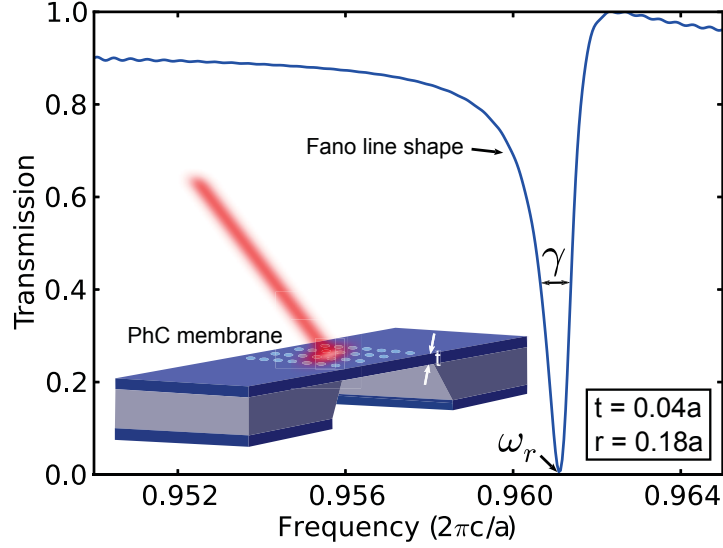


Figure 1.3: Transmission spectrum of a square lattice PhC membrane under normally-incident plane wave illumination. The PhC membrane supports leaky modes that interfere with incident radiation, giving rise to a Fano line shape. The transmission spectrum is obtained by the finite-difference time-domain method, and details can be found in Chapter 2. The lattice constant of the PhC crystal is denoted by a whereas r denotes the radius of the holes and t the membrane thickness.

1.4 Thesis Outline

The objective of the work presented in this thesis is to design, fabricate, and characterize a PhC membrane that is highly reflective at the wavelength of our low-noise lasers, and sufficiently lightweight / mechanically compliant to be strongly influenced by radiation pressure. Figure 1.4 is an overview of the thesis. Chapter 2 covers simulations of the optical

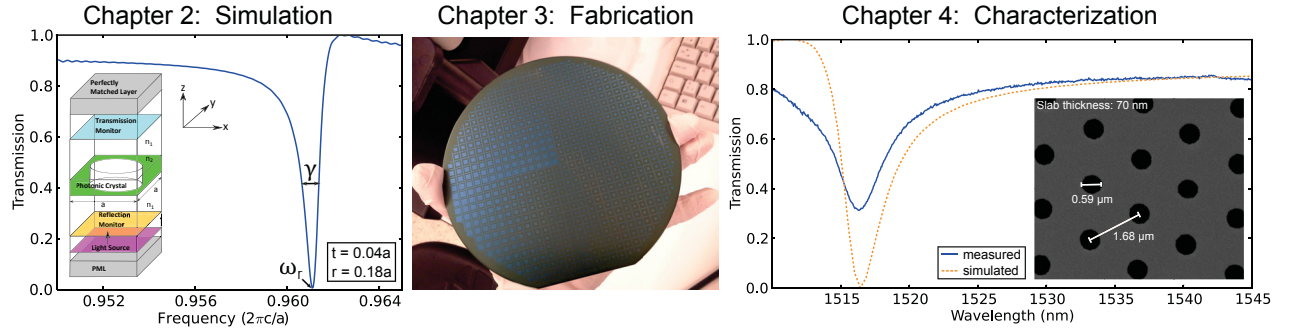


Figure 1.4: Graphical overview of the thesis.

performance of PhC membranes. The results of the simulations are used as a guide to carry

out the fabrication of PhC membranes. The fabrication process flow is reported in Chapter 3. Chapter 4 describes the method to optically characterize the fabricated devices, and presents the main result of this thesis; our ability to tune the spectral position of the PhC's resonance at the wavelength of our low-noise lasers.

Chapter 2

Photonic Crystal Membrane Design via Numerical Simulations

Before starting the fabrication of a PhC membrane, it is imperative to simulate its optical performance to determine physical parameters such as lattice geometry, hole radius, and membrane thickness that yield a high reflectivity near the target wavelength ($\lambda = 1550$ nm) of our low-noise lasers. The effects of structural tuning on the guided resonances supported in a PhC slab have been investigated before [28, 33, 35, 37–39]. By varying these parameters, it is possible to adjust the spectral position and linewidth of the resonance. The simulations are performed with Meep, a free software using the finite-difference time-domain (FDTD) method for solving electromagnetism problems [40]. Meep is available online at <http://ab-initio.mit.edu/meep>, and readily runs on Unix-like operating systems.

In Sec. 2.1 we describe the operating principles of Meep to understand how the transmission and reflection spectra of a structure are generated. Then, in Sec. 2.2 we introduce some of the parameters over which the user has control, and we describe the optimal settings that produce trustworthy results while maintaining a reasonable computational time. Finally, in Sec. 2.3 we report the simulation results that will guide the fabrication of PhC membranes in Chapter 3.

2.1 Operating Principles of Meep

In this section, we introduce the FDTD method (Sec. 2.1.1) and the boundary conditions supported in Meep (Sec. 2.1.2), and we describe how the transmission and reflection spectra from a structure are obtained (Sec. 2.1.3).

2.1.1 Solving Maxwell’s Equations with the Finite-Difference Time-Domain Method

The first step for Meep is to solve Maxwell’s equations, which give the time evolution of the displacement field \mathbf{D} and the magnetic flux density \mathbf{B} :

$$\frac{\partial \mathbf{D}}{\partial t} = \nabla \times \mathbf{H} - \mathbf{J} \quad (2.1)$$

$$\frac{\partial \mathbf{B}}{\partial t} = -\nabla \times \mathbf{E}. \quad (2.2)$$

\mathbf{H} and \mathbf{E} are the magnetic and electric fields respectively, with $\mathbf{D} = \epsilon_r \mathbf{E}$ and $\mathbf{B} = \mu_r \mathbf{H}$ for a linear medium. ϵ_r and μ_r are the relative permittivity (dielectric constant) and relative permeability, respectively. \mathbf{J} is the current density. Meep solves the initial value problem for which the fields and current are zero for $t < 0$. For $t \geq 0$, the latter are evolved in response to $\mathbf{J}(\mathbf{x}, t)$ [40].

The FDTD method discretizes space and time into a grid. The spatial resolution Δx is related to the temporal resolution Δt via the “Courant factor” \mathcal{S} : $\Delta t = \mathcal{S} \Delta x$. To ensure the stability of the method, \mathcal{S} must satisfy $\mathcal{S} < n_{min}/\sqrt{d}$, where n_{min} is the smallest refractive index, and d is the dimensionality [41]. For $d = 1, 2, 3$, and $n_{min} = 1$, $\mathcal{S} = 1/2$ meets this requirement, and so this is the default value in Meep. A finer resolution improves accuracy, but increases computational time, thus imposing a trade-off (see Sec. 2.2.2).

In the finite-difference method, derivatives appearing in Eq. 2.1 and Eq. 2.2 are replaced by the appropriate numerical differentiation formulas, which involve the step size $\mathbf{h} = (\Delta x, \Delta t)$. The error $\mathcal{E}(\mathbf{h})$ of the finite-difference method is defined to be the difference between the numerical approximation and the exact solution to the differential equation being solved [42]. $\mathcal{E}(\mathbf{h})$ comes from the round-off inherent to the way decimal numbers are treated in a computer, and from the discretization of the domain of the function appearing in the differential equation. Meep discretizes Maxwell’s equations with second-order accuracy, meaning $\mathcal{E}(\mathbf{h}) \propto h^2$ [41, 42]. To achieve second-order accuracy, Meep uses the “Yee lattice” discretization [41].

The Yee lattice is tiled with a cube of size $\Delta x \times \Delta x \times \Delta x$, where the components of \mathbf{E} and \mathbf{H} are stored at different spatial locations [43]. For computations that require \mathbf{E} and

\mathbf{H} at the same spatial location (e.g. the transmitted power through a structure involves the Poynting vector $\mathbf{S} = \mathbf{E} \times \mathbf{H}$), Meep interpolates the fields [43]. For more information on the Yee lattice, we refer the reader to Refs. [40, 43].

2.1.2 Terminating the Computational Cell with Boundary Conditions

Meep supports finite rectangular computational cells. The latter is discretized according to Δx , and can be terminated using three types of boundary conditions: Bloch-periodic boundaries, perfectly matched layers (PMLs), and metallic walls [41]. The Bloch-periodic boundary condition applies to systems with discrete translational symmetry. In this case, an eigenmode $\mathbf{A}_{\mathbf{k}}$ of the electromagnetic field is labeled by a Bloch wave vector \mathbf{k} lying in the first Brillouin zone, and is written

$$\mathbf{A}_{\mathbf{k}} = e^{i\mathbf{k}\cdot\mathbf{r}} \mathbf{u}_{\mathbf{k}}(\mathbf{r}), \quad (2.3)$$

where $\mathbf{u}_{\mathbf{k}}(\mathbf{r}) = \mathbf{u}_{\mathbf{k}}(\mathbf{r} + \mathbf{R})$ is a periodic function of \mathbf{R} , a lattice vector [31]. For systems with discrete translational symmetry, \mathbf{k} is conserved modulo the addition of reciprocal lattice vectors. The PMLs boundary condition is an open boundary condition. PMLs are an artificial material absorbing incident light, and are reflectionless [41]. The metallic wall boundary condition simulates a perfect metal, for which \mathbf{E} and \mathbf{H} are zero at the interface. For the case of PhC membranes, a combination of Bloch-periodic boundary conditions and PMLs are used to terminate the computational cell (see Sec. 2.2.1).

2.1.3 Transmission and Reflection Spectra

To obtain the transmission and reflection coefficients of a structure as a function of the frequency of the incident fields on the structure, one can apply a short pulse in the time domain (contains all frequencies), and apply a Fourier transform to the response of the system.

For an electromagnetic field with frequency ω passing through a surface S , the transmitted power is given by the integral of the Poynting vector over S [40, 41]:

$$P(\omega) = \text{Re} \left\{ \hat{\mathbf{n}} \cdot \int_S \tilde{\mathbf{E}}(\omega, \mathbf{x})^* \times \tilde{\mathbf{H}}(\omega, \mathbf{x}) \, d^2\mathbf{x} \right\}, \quad (2.4)$$

where $\hat{\mathbf{n}}$ denotes the normal to S , and $\tilde{\mathbf{E}}(\omega, \mathbf{x})$, $\tilde{\mathbf{H}}(\omega, \mathbf{x})$ are the Fourier transformed fields for $\mathbf{x} \in S$. In practice, S is a plane placed on the side of the structure opposite to the

source. To calculate $\tilde{\mathbf{E}}(\omega, \mathbf{x})$ and $\tilde{\mathbf{H}}(\omega, \mathbf{x})$, Meep performs a discrete-time Fourier transform (DTFT) [40]:

$$\tilde{\mathbf{E}}(\omega, \mathbf{x}) = \sum_n e^{i\omega n\Delta t} \mathbf{E}(n\Delta t, \mathbf{x}) \Delta t, \quad (2.5)$$

where n is fixed by the total time of the simulation, $\tau = n\Delta t$. The total time of the simulation is in turn determined by a condition chosen by the user. For example, the user can specify to run the simulation until the squared amplitude of the transmitted fields has decayed by a chosen factor of its maximum previous value. This condition is checked after each increment Δt . To obtain the normalized transmission, one runs the simulation with and without the structure, taking the ratio of Eq. 2.4 acquired with each run.

For the reflection spectrum, the plane constituting S is placed on the same side of the structure as the source. In this case, Eq. 2.4 cannot be used since it would return the contribution of both the reflected and incident power. One must subtract the Fourier transform of the incident fields, by running the simulation with and without the structure [41]:

$$P(\omega) = \text{Re} \left\{ \hat{\mathbf{n}} \cdot \int_S (\tilde{\mathbf{E}}(\omega, \mathbf{x})^* - \tilde{\mathbf{E}}_0(\omega, \mathbf{x})^*) \times (\tilde{\mathbf{H}}(\omega, \mathbf{x}) - \tilde{\mathbf{H}}_0(\omega, \mathbf{x})) d^2\mathbf{x} \right\}, \quad (2.6)$$

where the subscript zero refers to the incident fields. Again, Eq. 2.6 is normalized by the incident power obtained when no structure is present.

2.2 Parameters Regulating the Computational Cell and the Computational Time

We introduce the parameters that define the computational cell in Sec. 2.2.1, and the parameters that determine the computational time (i.e. the actual time it takes for a computer to perform a simulation) in Sec. 2.2.2.

2.2.1 Computational Cell

The starting point for a Meep simulation is a control file, written with the programming language Scheme. The structure geometry, sources, and quantities to be calculated are specified with the control file. To facilitate the operation of the control file, we wrote a Python script (a user-friendly programming language compared to Scheme) which communicates with the control file. The script allows the user to input parameters and implement loops,

and takes care of data sorting, handling, and plotting.

The computational cell is sketched in Fig. 2.1 for the case of a square lattice PhC slab. In Meep, constants such as the speed of light (c) are dimensionless and equal to 1, and the structure is defined in terms of a characteristic length, a [41]. In this case, a is the lattice constant of the PhC. The computational cell is terminated with Bloch-periodic boundaries along the x and y directions to simulate an infinite lattice of holes. The refractive index of

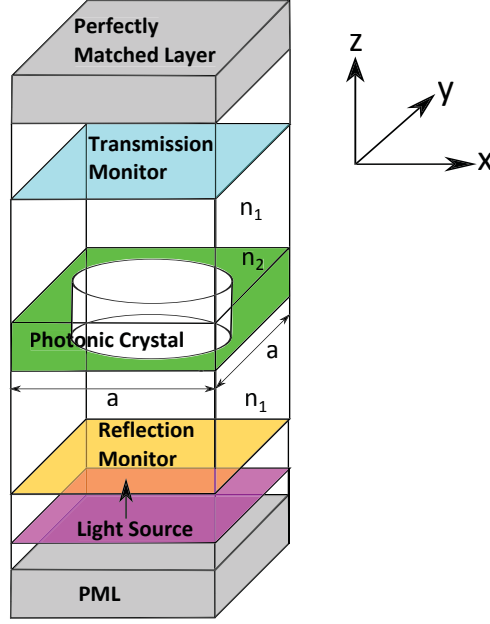


Figure 2.1: Computational cell to calculate the transmission and reflection spectra of an infinite square lattice PhC slab.

air (white region) is $n_{air} = 1.0$, and the material of the crystal is assumed to be silicon nitride (SiN) with index $n_m = 2.0$ [19, 44]. Silicon nitride is investigated owing to its low absorption near $\lambda = 1550$ nm ($\text{Im}[n_m] \sim 10^{-6}$ [19, 25, 44]), and to its compatibility with standard microfabrication processes. The transmission and reflection plane monitors are positioned at $(0, 0, 2a)$ and $(0, 0, -2a)$ respectively, with the origin corresponding to the center of the PhC hole. This distance is chosen so that for the wavelength range investigated ($\lambda \in 1500 - 1600$ nm) $\lambda < 2a$, thereby avoiding near-field effects. The PMLs live inside the computational cell, and are located at $(0, 0, 4a)$ and $(0, 0, -4a)$ with a thickness a to mimic free space. The light source at $(0, 0, -2.5a)$ is a pulse with a center frequency f_c and a Gaussian envelope. The pulse width δf determines the frequency range investigated. The polarization of the electric field is specified to be linear and along y . Since a square lattice looks the same along the two directions forming the $\{\hat{\mathbf{e}}_1, \hat{\mathbf{e}}_2\}$ basis, any polarization $\mathbf{E} = E_x \hat{\mathbf{e}}_1 + E_y \hat{\mathbf{e}}_2$ is expected

to yield the same transmission and reflection spectra [26–28, 45].

2.2.2 Computational Time

The computational time T_c for a simulation of the transmission and reflection spectra of a PhC slab is governed by three parameters:

- resolution (Δx);
- number of frequencies at which power is computed (N);
- time specified for the simulation to run (τ).

For example, if Δx is halved, T_c increases by a factor of 2×2^3 (there are three spatial dimensions, and the time step size is $\Delta t = \frac{\Delta x}{2}$). As for the two other parameters, T_c scales linearly with N and τ . In principle, Δx and τ should be chosen according to the so-called “sampling theorem” [46]. When dealing with a signal with zero spectral content above a cutoff value b , there is no benefit to sampling at a rate faster than $(2b)^{-1}$, where $2b$ is called the “Nyquist frequency”. However, we will see in the next paragraph that there is a subtlety that prevents a direct application of the sampling theorem.

Here, the signal corresponds to the source electric field. The temporal width of the Gaussian envelope δt is proportional to $\frac{1}{\delta f}$, and the start/stop of the source is controlled by a cutoff parameter (\mathcal{C}) which fixes the number of temporal widths the current decays for before it is set to zero [47]. This start/stop scheme implies that the signal is not truly band limited. In that regard, trying to determine the Nyquist frequency is irrelevant. Instead, setting a large enough \mathcal{C} ensures that the amount of high-frequency components introduced by the start/stop of the source is suppressed [47]. Given the nature of the source, any sampling rate $(\Delta t)^{-1} = (\frac{\Delta x}{2})^{-1}$ will never satisfy the criteria for perfect fidelity. However, with an appropriate \mathcal{C} , it is possible to choose a sampling rate which allows for the recovery of the relevant Fourier components of the signal. More precisely, ~ 20 spatial pixels per wavelength in the high-dielectric region (corresponding to $\Delta x \simeq 40$ for the parameters investigated) and $\mathcal{C} = 5.0$ yield a smooth transmission spectrum devoid of artifacts. Non-physical features usually manifest themselves as sharp lines or wiggles near the edges of the transmission spectrum. In practice, a good sanity check is to increase the resolution and verify that it does not change the results of the simulation.

The relation between τ and \mathcal{C} is $\tau = 2\mathcal{C} \times \delta t + \tau_0$, where τ_0 is chosen to be the time it takes for the squared electric field amplitude to decay by 10^{-6} at the transmission monitor. This condition ensures that we wait long enough for the Fourier transforms in Eq. 2.4 and Eq. 2.6 to be accurate [48]. In addition, τ_0 allows for investigation of the frequencies and decay rates of the modes that are excited in the PhC slab with Meep’s Harminv package [49] (see Sec. 2.3.2). Finally, N is chosen to be largest number which satisfies $\frac{\delta f}{N} \geq \frac{1}{\Delta t}$ to avoid aliasing.

2.3 Results

The results presented below are valid for infinite lattices. In practice, the PhC area on the membrane is finite. Nevertheless, the results of the simulation are expected to be an accurate description of the experimental characterization of the PhC membrane under the following conditions. Firstly, the $\frac{1}{e^2}$ beam intensity diameter should be smaller than the lateral dimension of the PhC area, but large compared to the hole size to approach the limit of an infinite plane wave. Secondly, the PhC membrane should be characterized at the waist of the beam, where light behaves the most as a plane wave. Within these requirements, the results of the simulation are relevant. Finally, it is worth pointing out that Meep implements subpixel averaging [40] so that varying a structural parameter by an amount smaller than the quantity $\frac{a}{\Delta x}$ still affects the result of the simulation.

2.3.1 Frequency Domain

In this section, we present the transmission spectrum of a PhC slab for different structural parameters. We attempt to find parameters that are compatible with fabrication and that yield a high reflectivity at $\lambda = 1550$ nm. Our nitride is 100-nm-thick (set by our existing wafers), so we first consider devices of this thickness, finding that the square lattice would be difficult to fabricate (Sec. 2.3.1.1), and that a hexagonal lattice would be sturdier, but would not achieve as high a reflectivity for all polarizations (Sec. 2.3.1.2). However, we can also in principle tune the thickness of our nitride with hydrofluoric (HF) etching (Sec. 2.3.1.3), which ultimately provides a sturdy and highly reflective system at the target wavelength.

2.3.1.1 Square Lattice, 100 nm thick

Fig. 2.2 shows the normal incidence transmission spectrum of a square lattice PhC membrane with lattice constant $a = 1500$ nm, thickness $t = 100$ nm, refractive index $n_m = 2.0$,

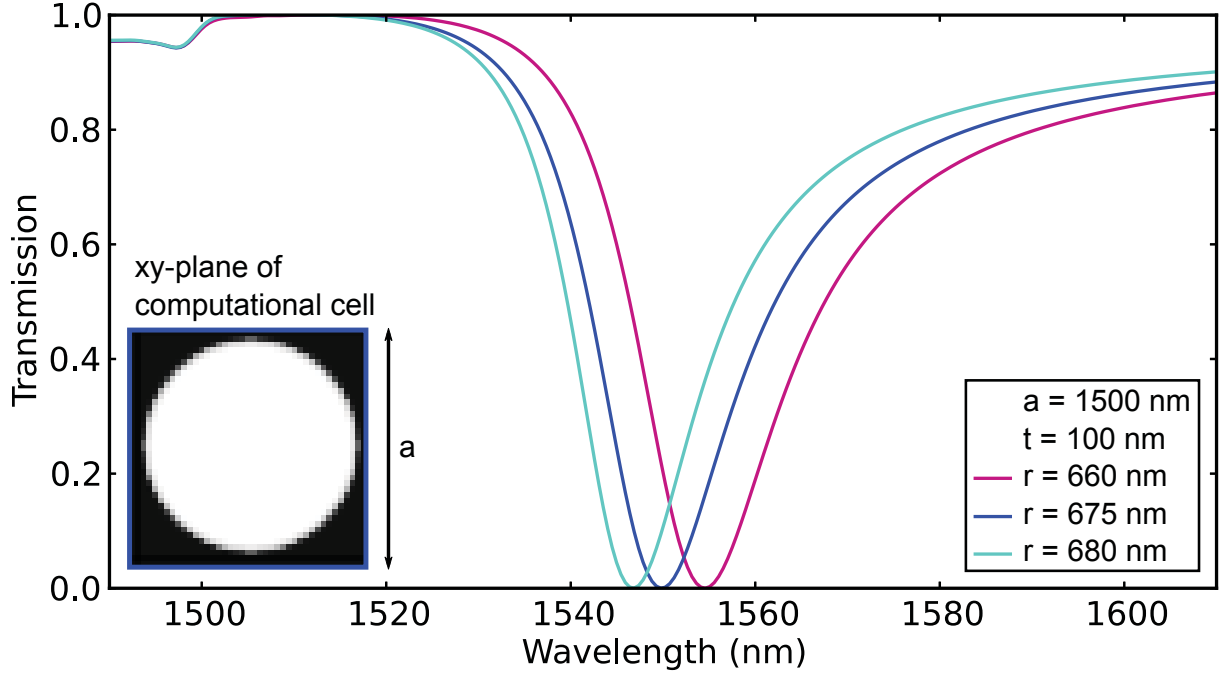


Figure 2.2: Normal incidence transmission spectrum of a square lattice PhC slab with different radii. The inset shows the xy plane of the computational cell at $z = 0$ for the blue curve.

and radius $r \in \{660, 675, 680\}$ nm. As can be seen, near $\lambda = 1550$ nm there is a resonant dip in transmission that reaches zero. This simulation does not include loss, so the reflected power at this point is 100 %. The radius is varied since it is a parameter that can be readily modified in the fabrication process flow. In this parameter regime, a larger radius is found to decrease the average refractive index of the PhC slab, causing the resonance to occur at a smaller wavelength [38]. This wavelength shift is not a linear function of r in general, even for small fractional changes (the resonance shift is half as much from 675-680 nm as for 660-675 nm).

The quality factor Q of the resonance is extracted by fitting the simulation data to Eq. 1.17. For the curves displayed in Fig. 2.2, $Q \in \{76, 77, 87\}$. The increase in Q with r is unexpected because conventional wisdom states that leaky modes should become guided (high- Q) modes as the radius is made smaller. In fact, previous work [33, 35, 38] show that Q decreases with increasing radius, contradicting the effect observed here. We have not developed an intuition for this result, but it is worth noting that our devices are substantially thinner than Refs. [33, 35, 38] (i.e. $t = 0.07a$ as opposed to $t = 0.4a$), and possess a larger radius (we vary r close to $\frac{r}{a} = 0.45$ as opposed to $\frac{r}{a} < 0.45$). To confirm that our result

is sensible, we looked at the Q dependence of the leaky mode for a smaller $\frac{r}{a}$ ratio, and we were able to reproduce the effect observed in Refs. [33, 35, 38]. Indeed, for $t = 0.07a$ and $r \in \{0.2a, 0.27a\}$ we obtain $Q \in \{158, 84\}$. This suggests that the inspected guided resonance eventually becomes a true guided mode as the radius approaches zero. Given t , there exists a $\frac{r}{a}$ cutoff for which, above it, decreasing r decreases Q , whereas below it, decreasing r increases Q . A possible explanation could be that varying a structural parameter can change the electric field distribution of the leaky mode in such a way that it favors or opposes coupling to external radiation, as reported in Ref. [38]. To ensure the validity of our observations, we increased the resolution to $\Delta x = 60$ and the results were quantitatively unchanged. As a sanity check, we also ran a simulation for $t = 0.04a$ and $r \in \{0.18a, 0.36a\}$, and obtained $Q \in \{990, 241\}$, which further validates the reversed dependence for the thin-crystal limit.

Under the assumption of negligible absorption, this result translates to a high-reflectivity device at $\lambda = 1550$ nm for $r = 675$ nm. A device with these parameters is practically impossible to fabricate since the aspect ratio $\frac{2r}{a}$ approaches 1, and results in the membrane collapsing in the etching / releasing fabrication step (see Sec. 3.2.4). Thus, another lattice type offering a sturdier geometry is investigated in the next section.

2.3.1.2 Hexagonal Lattice, 100 nm thick

Figure 2.3 shows the transmission spectrum of a hexagonal lattice with lattice constant $a = 1675$ nm, thickness $t = 100$ nm, and radius $r \in \{400, 420, 440\}$ nm. As for the square lattice, increasing the radius shifts the resonance toward smaller wavelengths. In contrast to the square lattice discussed above, increasing the radius decreases the lifetime ($Q \in \{64, 59, 54\}$), in agreement with the effect observed in Ref. [33, 35, 38]. The first advantage of a hexagonal lattice is that the aspect ratio is fabricable. Secondly, the hexagonal lattice type displays a resonance with a greater linewidth, allowing for more flexible fabrication tolerances. As opposed to the square lattice, the hexagonal lattice is polarization dependent. Indeed, this lattice has a different periodicity along the two directions forming the $\{\hat{\mathbf{x}}, \hat{\mathbf{y}}\}$ basis. The effect of an incident electric field linearly polarized along $\hat{\mathbf{x}}$, $\hat{\mathbf{y}}$, or a combination of both is shown in Fig. 2.4. This polarization dependence can be convenient for shifting the location of the resonance by a few nanometers. On the other hand, when polarization is mixed, it limits the achievable reflectivity.

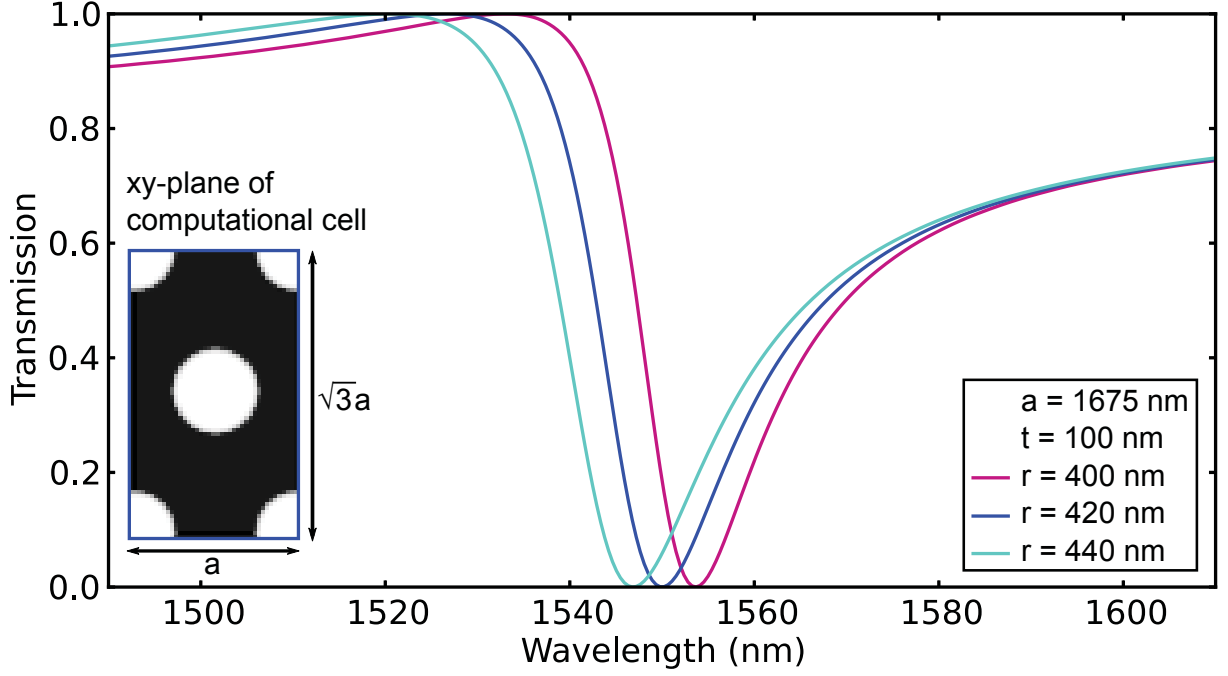


Figure 2.3: Normal incidence transmission spectrum of a hexagonal lattice PhC slab with different radii. The inset shows the xy plane of the computational cell at $z = 0$ for the blue curve.

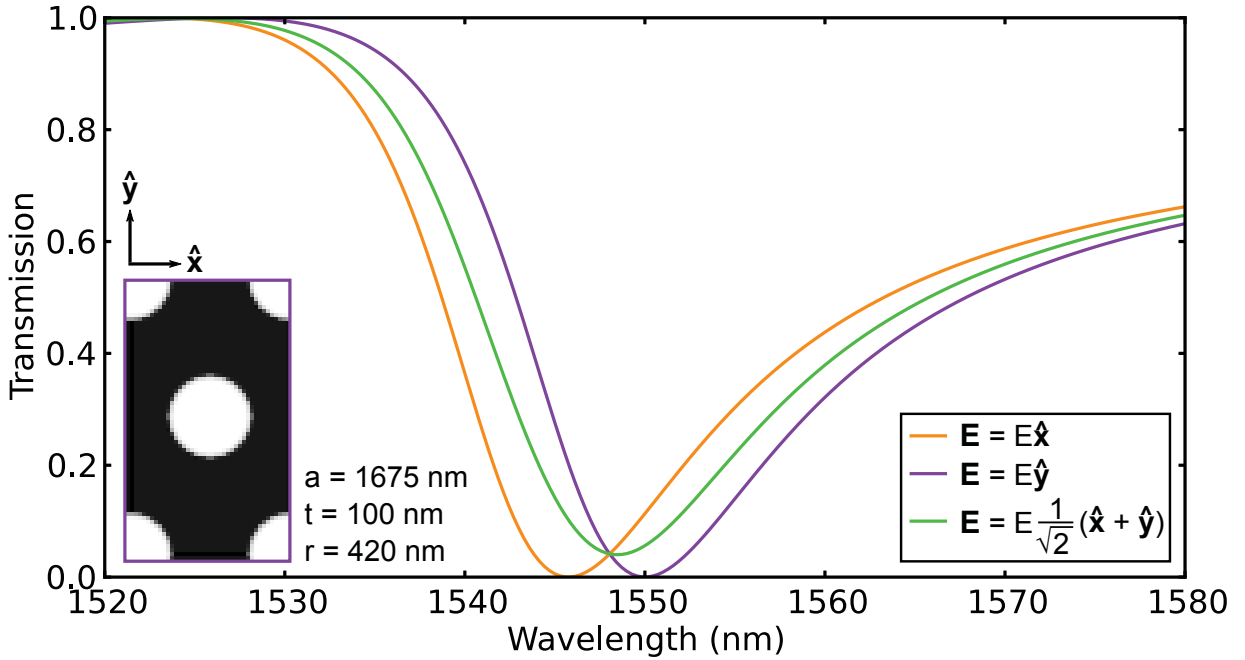


Figure 2.4: Normal incidence transmission spectrum of a hexagonal lattice PhC slab for different electric field polarizations. The inset shows the xy plane of the computational cell at $z = 0$ for the purple curve.

2.3.1.3 Hydrofluoric Acid Tuning of the Resonance

An alternative to using a hexagonal lattice for designing a device with a reasonable aspect ratio is tuning the thickness of the PhC membrane. For SiN, HF acid can be used to thin the SiN device layer at the beginning of the fabrication process flow. Likewise, once the PhC membrane is fabricated, HF acid can be used to tune the location of the resonance by simultaneously thinning the membrane and widening the hole diameter (see Sec. 4.4.2). A similar approach has been employed within the context of SiN microdisk resonators [50]. Fig. 2.5 shows the transmission spectrum of a square lattice for different time spent in HF acid. The initial thickness of the released membrane is $t = 60$ nm, and the initial hole radius

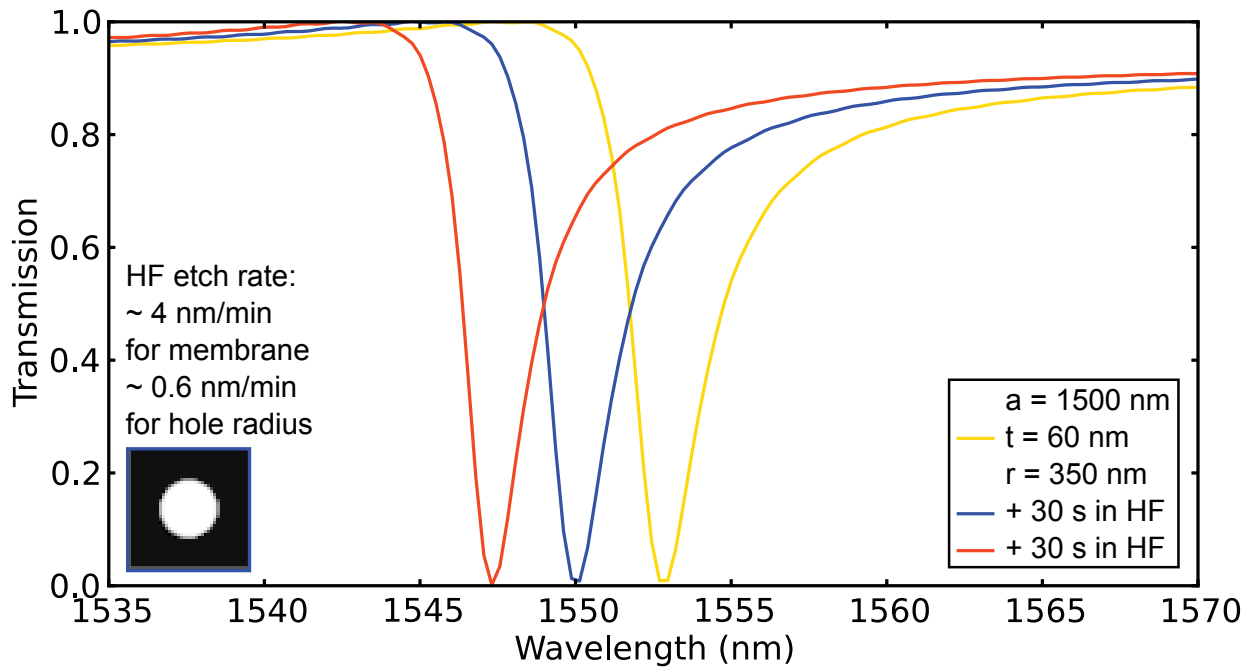


Figure 2.5: Normal incidence transmission spectrum of a square lattice PhC slab for different time spent in HF acid. The geometries are set by the etch rate of SiN in HF. The inset shows the xy plane of the computational cell at $z = 0$ for the blue curve.

is $r = 350$ nm. The subsequent geometries are set by the etch rate of SiN in HF: during fabrication (Chapter 3), we measured ~ 4 nm/min for the thickness and ~ 0.6 nm/min for the radius. The timescale associated with the shift of the resonance can be readily achieved during fabrication. For the chosen geometrical parameters, the resonance shift is ~ 5.5 nm/min toward smaller wavelengths. Indeed, for smaller thicknesses the electric field distribution of the mode extends further into free space, thereby lowering its effective refractive index [38]. Furthermore, the decrease in thickness paired with smaller radius results in a higher Q res-

onance. For comparison, the Q factors of the resonances in Fig. 2.5 are approximately eight times larger than the ones displayed in Fig. 2.2.

At this point, the simulations indicate that a reasonable approach would be to fabricate a hexagonal lattice PhC slab with $t \sim 100$ nm, and a square lattice PhC slab with $t \sim 60$ nm. So far our results have not taken into account material absorption. To make sure that the absorption of SiN near $\lambda = 1550$ nm does not invalidate our findings, we consider material absorption in the next section.

2.3.1.4 Material Absorption

Meep supports material absorption by mimicking a complex dielectric function through the conductivity σ_D [51]: $\text{Im}(\epsilon_r) = \text{Re}[\epsilon_r]\sigma_D/\omega$, where σ_D is related to the conventional conductivity σ via $\sigma_D = (a/c)\sigma/\epsilon_r\epsilon_0$. This approach is dispersionless so that absorption only takes place in a narrow bandwidth about the specified frequency ω . Alternatively, it is also possible to specify a frequency-dependent dielectric function via the Lorentz model [51].

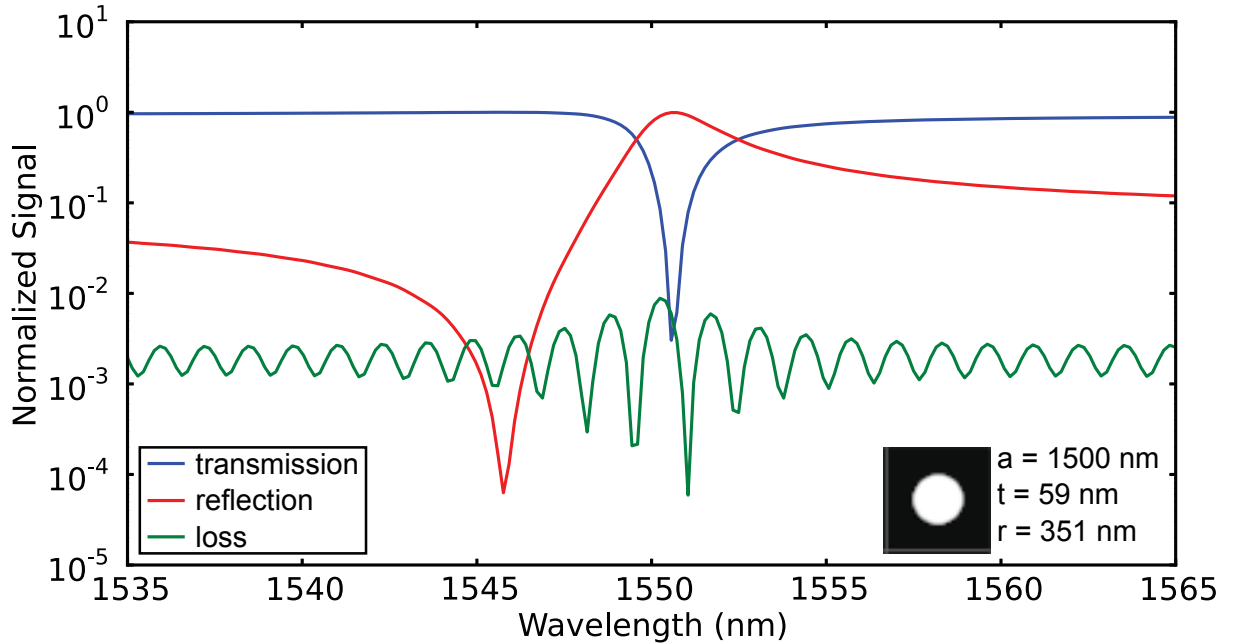


Figure 2.6: Normal incidence transmission spectrum on a logarithmic scale for a square lattice PhC slab set with $\text{Im}[n_m] = 1.5 \times 10^{-6}$. The small absorption of SiN around $\lambda = 1550$ nm is not adequately captured by the simulation.

We did not adopt this model because we did not have the parameters to accurately reproduce a frequency-dependent dielectric function for SiN. Therefore, the former heuristic method

is applied in what follows. Previous work set an upper bound for the absorption of SiN in the vicinity of 1550 nm: $\text{Im}[n] \leq 1.5 \times 10^{-6}$ [19]. Using this value, the transmission (T), reflection (R) and loss ($1 - R - T$) are plotted on a logarithmic scale in Fig. 2.6. The loss curve is spurious and reveals that the absorption of SiN is not properly modeled by the current settings of the simulation. A thorough analysis would require a higher resolution (and hence a longer computational time) and possibly the Lorentz model to capture the absorption of SiN. At this stage of the project we decided to move on with the fabrication and characterization of our devices before worrying about absorption. Prior to presenting the fabrication process flow (Chapter 3), we lastly explore in the time domain the leaky mode responsible for the PhC’s resonance in the next section.

2.3.2 Time Domain

In this section, we further investigate the guided resonance causing the Fano line shape in the transmission spectrum of the PhC slab by calculating a region of its band structure, and looking at its electric field distribution in the time domain.

Meep can output the spatial distribution of the amplitude of the electric field for different planes of the computational cell as a function of time. Furthermore, Meep enjoys a package (Harminv) [49] that computes the frequency, lifetime, amplitude, and phase of the sinusoids composing a finite-length time signal [52]. This algorithm is known as “harmonic inversion”. In this case, the time signal corresponds to the electric field generated by exciting a source inside the PhC slab and letting it decay. These two features of Meep allow for the investigation of the leaky mode supported by the PhC slab responsible for the Fano line shape observed in the transmission spectrum. Fig. 2.7a shows the band structure along the high-symmetry line $\Gamma \rightarrow X$ for a PhC slab with $t = 0.04a$ and $r = 0.18a$. Discrete translational symmetry in the xy plane ensures that the x and y components of the wave vector \mathbf{k} are conserved modulo the addition of reciprocal lattice vectors. The addition of a reciprocal lattice vector to a mode with \mathbf{k} does not change the properties of the latter [31]. Therefore, for light normally-incident to the PhC slab, $\mathbf{k} = k\hat{\mathbf{z}}$ so that the relevant point in the band structure is Γ . The y -axis in Fig. 2.7a covers a frequency range above the light line, and in the vicinity of the resonance observed in Fig. 2.7c. In this region, the PhC slab supports two modes at the Γ point with $\omega_- = 0.9504 (2\pi c/a)$ and $\omega_+ = 0.9601 (2\pi c/a)$. Inspection of the spectrum in Fig. 2.7c reveals that only the mode at ω_+ manifests itself. Refs. [28, 35] show that the mode at ω_- does not couple to plane waves propagating normal

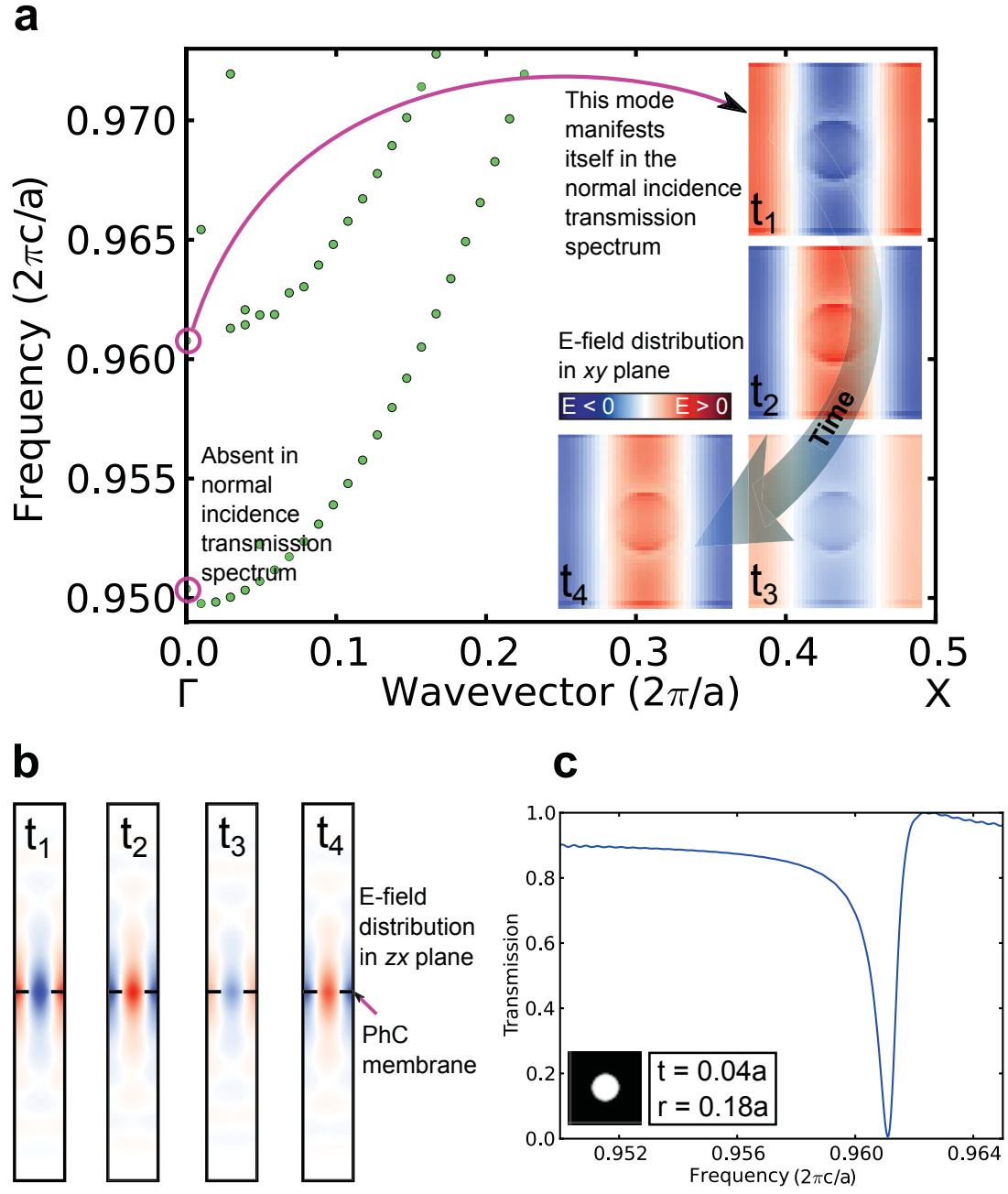


Figure 2.7: Band structure and mode profile of the guided resonance causing the Fano line shape. **a**, Band structure along the high-symmetry line $\Gamma \rightarrow X$ for a PhC slab with $t = 0.04a$ and $r = 0.18a$. The inset shows the time evolution of the electric field distribution of the mode at $\omega_+ = 0.9601$ ($2\pi c/a$) in the xy plane of the computational cell. **b**, The electric field distribution of the mode at ω_+ in the zx plane indicates that it is weakly confined to the slab. **c**, The transmission spectrum reveals that only the mode at ω_+ manifests itself.

to the slab due to symmetry mismatch. The inset of Fig. 2.7a shows the spatial distribution of the electric field amplitude of the mode at ω_+ in the xy plane for different times, after the source has been turned off. The corresponding distribution is illustrated in Fig. 2.7b for the zx plane and reveals that the mode is weakly confined to the slab. Coupling between this mode and normally-incident plane waves gives rise to a Fano line shape in the transmission spectrum [33–35]. Finally, it is a good sanity check to compare the mode’s resonant frequency and Q factor obtained with harmonic inversion to the transmission spectrum. The first method yields $\omega_0 = 0.9601 (2\pi c/a)$ and $Q = 1392$ whereas the second method gives $\omega_0 = 0.9611 (2\pi c/a)$ and $Q = 990$, showing reasonable agreement.

The results presented in Sec. 2.3 are used as a guide for the fabrication of the PhC membranes. The fabrication process flow is the topic of the upcoming chapter.

Chapter 3

Photonic Crystal Membrane Fabrication

This chapter summarizes the method to fabricate a thin (50 - 100 nm) free-standing SiN membrane incorporating a 2D PhC that is highly reflective at the wavelength ($\lambda = 1550$ nm) of our low-noise lasers. The wavelength-scale features of the PhC require fabrication with sub-micron precision, and so the array of holes is achieved by electron beam lithography (EBL) and dry etching. As for the free standing membranes, they are constructed using photolithography, dry etching, and wet etching. We begin with Sec. 3.1 to outline the basic principles of photolithography and EBL. Then, we summarize each step of the fabrication process flow in Sec. 3.2. Finally, in Sec. 3.3 we discuss how the process flow could be improved.

3.1 Fundamentals of Photolithography and Electron Beam Lithography

Before embarking into the details of the fabrication process flow, we outline the fundamentals of photolithography and EBL techniques. Photolithography relies on the use of a photomask, an opaque plate with transparencies that allows for the transfer of geometrical patterns with a resolution of ~ 1 μm onto a substrate (wafer). A generic photolithography process is depicted in Fig. 3.1. The patterns are transferred as ultraviolet (UV) light is shone through the mask and onto a thin layer of light-sensitive chemical (photoresist) deposited on the wafer. The areas of the resist subjected to exposure undergo a chemical change which allows a solution (referred to as developer) to remove them. After immersion in the developer, the photoresist layer is imprinted with the desired pattern, and the latter can be further transferred to the substrate with etching techniques.

EBL is similar to photolithography, but the exposure method is different. Indeed, geometrical patterns are written by scanning a focused beam of electrons onto an electron-sensitive

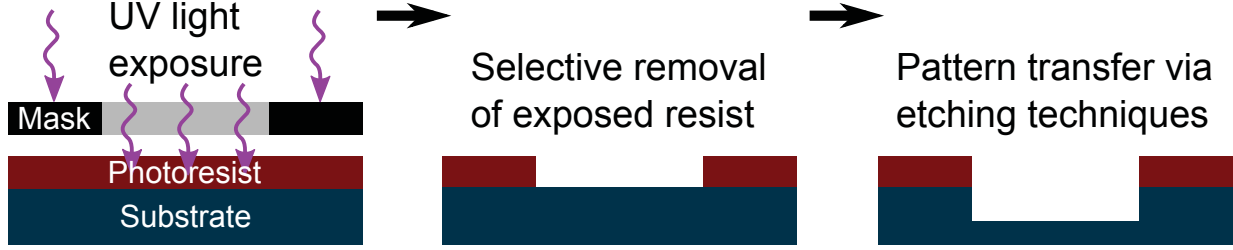


Figure 3.1: Generic photolithography process. Geometrical patterns are first transferred to a light-sensitive layer called photoresist by exposing it with UV light through a photomask. For the case of positive resist, the exposed areas are selectively removed by a chemical solution, as shown in the middle diagram. For the case of negative resist, it is the unexposed areas that are selectively removed. Once the photoresist is shaped, etching techniques allow for transfer of the pattern to the substrate.






film (EBL resist) so that a photomask is not required. The exposure patterns are instead stored into files that the EBL machine can read. In our case, the files are created with Raith NanoSuite, and the details are provided in Sec. 3.2.3.2. The achievable resolution is about two orders of magnitude greater in comparison to photolithography, but EBL is a lower throughput technique.

3.2 Process Flow

The process flow is sketched in Fig. 3.2, and we walk through each step in the ensuing subsections. The fabrication starts with a 150 mm diameter stoichiometric SiN wafer. The thickness of the nitride layer is 100 nm for both sides of the wafer, and the front side is polished. The bulk of the wafer is $\langle 100 \rangle$ type Si (650 μm thick). $\langle 100 \rangle$ refers to the crystal orientation of Si. In this case, crystal planes possessing (100) Miller indices are parallel to the plane of the wafer [53].

3.2.1 Membrane Fabrication

The goal of step 1 \rightarrow 2 (referring to Fig. 3.2) is to deposit a gold pattern consisting of a grid of 5×5 mm dies with alignment marks on the front side of the wafer for two purposes. First, the alignment marks are used to position the membranes in the center of each die in step 2 \rightarrow 3. Second, the gold grid, having an excellent visibility when imaging with the EBL tool, allows for alignment of the PhC with the underlying membrane. This gold pattern

 Silicon nitride (Si_3N_4).	 Photoresist S1813.	Wafer specs: $\langle 100 \rangle$, 150 mm.	Note: The sketches below represent a transversal cut through the wafer (not to scale).
 Silicon (Si).	 E-beam resist ZEP520A.	Device = 100 nm, polished.	
	 Ti/Au.	Handle = 650 μm .	

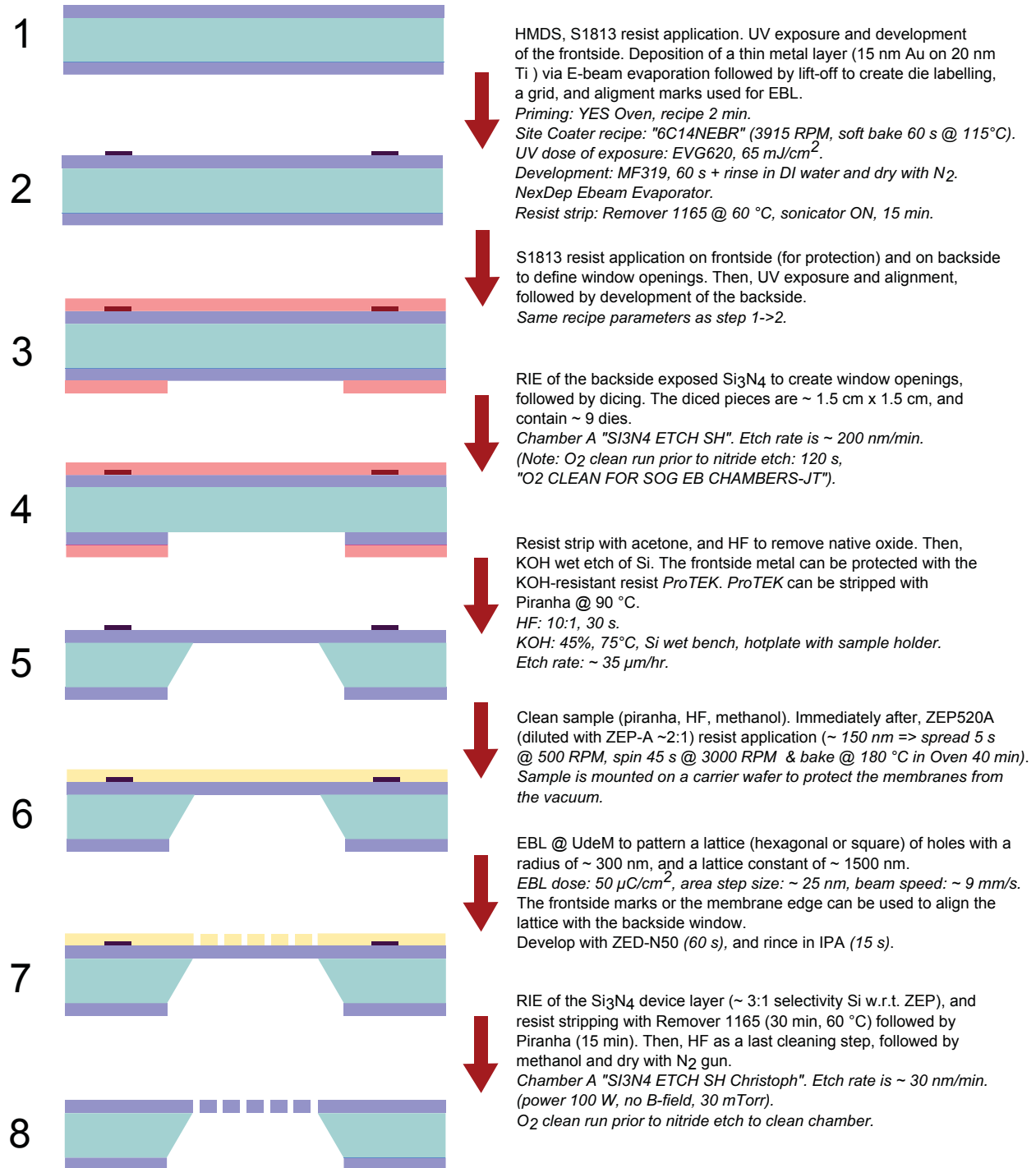


Figure 3.2: PhC membrane fabrication process flow.

is defined by our front mask, designed with GdsSpy, a Python module that creates GDSII format files used for writing masks. We use KLayout to view the geometries encoded in the GDSII format files. To begin, the wafer is dehydrated and primed in an oven for 120 s with hexamethyldisilazane (HMDS) to improve photoresist adhesion. Afterwards, the front side of the wafer is spin-coated (3915 rpm) with 1.4 μm Shipley S1813 positive resist, and soft baked on a hotplate at 115 °C for 60 s. The front mask is then loaded in a machine (EVG620) set in soft contact mode (50 μm separation between mask and wafer), and the exposure dose is 65 mJ/cm². The areas of the resist subjected to exposure are removed with MF319 developer. The wafer is immersed in a beaker of MF319 for 60 s while it is gently agitated, and subsequently rinsed in a beaker of deionized (DI) water. During drying, the wafer is held vertically so that its flat edge rests on a wipe, and a N₂ spray gun is used to guide liquid toward the wipe. Then, metal (15 nm Au on 20 nm Ti) is deposited on the frontside of the wafer via electron beam evaporation (EBE)¹. Titanium serves as an adhesion layer between the dielectric substrate and the gold. To complete the pattern transfer, the resist is cleared away in Remover 1165 at 60 °C for 10 min, without sonication. This process is commonly known as a “lift-off”. The result is shown in Fig. 3.3a. The pattern consists of a grid (25 μm wide lines) of 5 mm x 5 mm dies. Each corner of a die is provided with a number (quadrant - column - row) for device tracking, and with a combination of cross and vernier lines for alignment with the back mask.

In step 2 \rightarrow 3, the front side is immediately coated with a dummy layer of resist for protection. Then, we use a back mask consisting of an array of windows of various sizes to create openings for the membranes. The photolithography parameters are the same as in the previous step, with the exception of EVG620 being set in hard contact mode where the mask is in contact with the wafer during exposure. Hard contact ensures that the alignment of a window opening on the back side with the center of the corresponding die defined by the metal grid on the front side falls within a few microns precision.

In step 3 \rightarrow 4, the exposed nitride is removed by reactive ion etching (RIE, Applied Materials P5000). RIE is a type of dry etching where ions of a plasma are accelerated toward a sample to chemically attack it or physically drill it (or both). The recipe used to etch SiN is based on the reactive gases CHF₃ (fluoroform) and CF₄ (tetrafluoromethane). These

¹EBE is a form of physical vapor deposition for which an electron beam bombards a target, causing the atoms of the target to evaporate and condensate onto the substrate area.

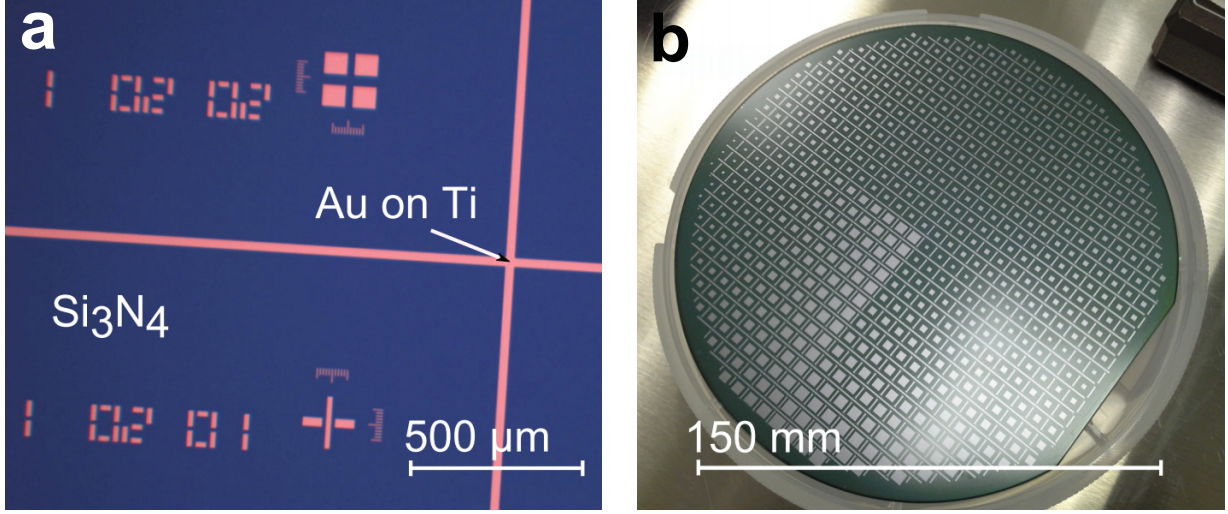


Figure 3.3: **a**, Au (15 nm) on Ti (20 nm) on the front side SiN. The pattern consists of a grid of 5 x 5 mm dies with crosses and vernier lines for back side alignment, and numbers for device identification. **b**, Back side of the wafer after SiN has been removed with RIE to form windows of various sizes. After KOH wet etching, the windows lead to membranes with lateral dimensions ranging from a few mm down to a few hundred μm .

gases provide F and CF_x ions to decompose silicon nitride according to [54]:



Etch characteristics are governed by gas species, gas flows, power, magnetic field, chamber pressure and etch time. These parameters are interlinked in a complex manner. In the event of a delicate etch step (e.g. step 7 \rightarrow 8), it is important to understand the role of each parameter. The ideal method to investigate their effect is to systematically vary one at the time. Non-reactive gases such as Ar can also be used to dilute the reactive gases to control the etch rate, and contribute to sample bombardment [55]. The momentum of the ions is set by the power and mostly affects etch anisotropy (i.e. directionality). The magnetic field strength controls the plasma density and predominantly influences the etch rate. Low chamber pressures offer a larger mean free path for the ions, thus favoring a vertical bias in the etch. On the other hand, higher chamber pressures allow for a better control over the gas flows, translating to more constant etch rates. The RIE in step 3 \rightarrow 4 is straightforward since it involves removing 100 nm of SiN to create mm-size windows on the back side of the wafer. Therefore, the RIE machine's default SiN recipe was used. However, as we will see in Sec. 3.2.4, this recipe cannot be used for delicate structures. The etch rate is measured

(with a reflectometer, Nanospec) to be in the range 200 - 250 nm/min, and resist selectivity is not an issue. The recipe parameters are tabulated in Table 3.1, and the back side of the wafer after etching is pictured in Fig. 3.3b.

Etch time (s)	Power (W)	B-field (G)	Chamber pressure (mTorr)
60	500	70.0	30
Gas	CHF ₃	CF ₄	Ar
Flow (sccm)	30	70	7

Table 3.1: Parameters for the RIE recipe used in step 3 \rightarrow 4.

Afterwards, the wafer is diced with the help of a diamond scribe and pliers in $\sim 1.5 \times 1.5$ cm samples, each containing ~ 9 dies. The dicing lanes on the wafer's back side are used as a guide for the scribe. The next step is to remove the resist from the chips, and use wet etching to go through the bulk Si.

In step 4 \rightarrow 5, the resist is stripped with acetone at 40 °C, and a 10:1 HF acid dip (60 s) is performed to remove leftover oxide or nitride on the bulk silicon of the windows. Then, the samples are placed in a 45 % potassium hydroxide (KOH) solution with a sample holder for ~ 20 hr at 75 °C to etch anisotropically through the $\langle 100 \rangle$ silicon. Different crystal planes have different etch rates, leading to an angle of $180 - \arctan \sqrt{2} = 125.3^\circ$ between the membrane and the sidewalls [53]. Contact profilometer (Ambios XP200) measurements reveal that the etch rate is within 30 - 35 $\mu\text{m/hr}$. The sample holder maintains the chips vertically (see Fig. 3.4a) so that bubbles can escape by minimally shaking the membranes, thus improving their survival. To protect the front side metal, a KOH-resistant resist (ProTEK) can be applied. Alternatively, we found that it is possible to do EBL without the front side metal; the suspended membrane can instead be used to position the array of holes (see Sec. 3.2.3.3). Nevertheless, metal is still deposited on the front side in case one desires to pattern the holes before releasing the membrane, as discussed in Sec. 3.3. Figure 3.4b shows the back side of a membrane after the KOH etch and a cleaning procedure described in Sec. 3.2.2.1.

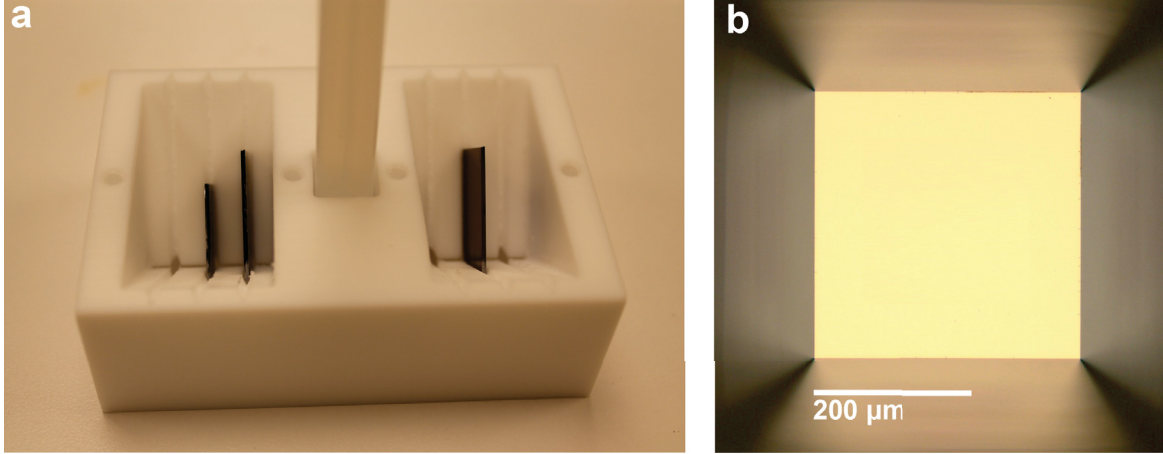


Figure 3.4: **a**, Sample holder for maintaining chips vertically and facilitating handling during wet etching and wet cleaning. **b**, Back side of a 100 nm thick SiN membrane after KOH etching and cleaning.

3.2.2 ZEP520A Resist Spin-coating

Still referring to Fig. 3.2, in step 5 \rightarrow 6 the released membrane must be coated with an EBL resist to pattern the PhC. In this section, we describe the spin-coating procedure. ZEP520A positive resist (Zeon Chemicals) is used because it provides high resolution and better dry etch resistance when compared to PMMA.

3.2.2.1 Sample Cleaning

The sample must be cleaned prior to spin-coating to ensure a uniform resist layer. The chips never leave the sample holder throughout the cleaning procedure to prevent the released membranes from breaking, and time spent outside liquid is minimized so that debris cannot stick to the membranes. First, the chips are removed from the KOH beaker and rinsed successively in two prepared beakers of DI water. Second, the chips are cleaned for 120 s in piranha solution, a mixture of sulfuric acid (H_2SO_4) and hydrogen peroxide (H_2O_2) with a 3:1 ratio. Then, the membranes are rinsed successively in two beakers of DI water. Third, the chips are transferred to a 10:1 HF solution for 30 s, and again rinsed twice in DI water. Finally, the chips are removed one by one from the immersed sample holder in DI water with tweezers, rinsed in methanol, and immediately dried with a N_2 spray gun. The chip is held at an angle so that methanol flows away in a single direction toward the tweezer's contact point as it is sprayed. This way, methanol residues accumulate near the tweezer's contact point, which is away from the membranes.

3.2.2.2 Spin-coating

The spin-coater (Laurell) uses a vacuum chuck to secure samples. To avoid aspirating the free-standing membranes, the chip (typically $\sim 1.5 \text{ cm} \times 1.5 \text{ cm}$ containing 9 devices) is mounted on a $\sim 5 \times 5 \text{ cm}$ carrier Si piece with adhesive wax. ZEP520A resist is diluted in anisole with a 1:2 ratio to lower viscosity, thus granting access to thinner layers. The procedure to dispense resist on the sample while minimizing the risk of contamination is the following. First, the Si carrier piece is secured in the center of the vacuum chuck. Second, after the bottle containing the diluted ZEP520A resist has been gently agitated by hand, $\sim 1 \text{ ml}$ is extracted with a disposal pipette. Third, the resist is transferred to a disposable plastic beaker. Fourth, the resist is extracted from the beaker with a 3 ml syringe while making sure bubbles do not form. Fifth, a $0.2 \text{ }\mu\text{m}$ particle filter is fixed to the tip of the syringe, and the resist is dispensed over the total area of the chip. A few cm size chip requires $\sim 0.5 \text{ ml}$ of resist. The spin-coating recipe is: dispense 5 s at 500 rpm, spin 45 s at 3000 rpm, and decelerate 5 s. For every step, the acceleration is 1305 rpm/s. This results into a $\sim 150 \text{ nm}$ thick resist layer (measured with a reflectometer, Nanospec), which is a compromise between thin layers offering better EBL resolution, and thick layers offering better dry etch protection. Indeed, for layers with a thickness below 150 nm, we observed that the majority of our membranes broke during dry etching (step 7 \rightarrow 8). Afterwards, the carrier is placed on a hot plate at 60°C for a few seconds to melt the wax and detach the chip. The chip is then baked for 40 min in an oven at 180°C . An oven is used instead of a hotplate for better heat transfer to the thin dielectric membranes. Fig. 3.5 shows a chip after it has been spin-coated with ZEP520A resist.

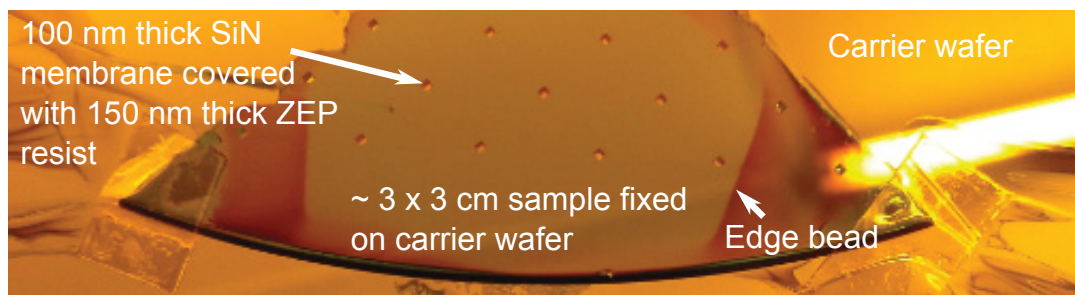


Figure 3.5: Sample fixed on a Si carrier piece after it has been spin-coated with ZEP520A resist.

3.2.3 Defining the Photonic Crystal with Electron Beam Lithography

In the following, we cover step 6 \rightarrow 7 of the process flow illustrated in Fig. 3.2. In Sec. 3.2.3.1 we present the optimal EBL settings and the involved trade-offs for patterning a PhC into the resist covering the suspended membranes. Then, in Sec. 3.2.3.2 we describe the files which constitute the exposure pattern, and the preparation of the sample for EBL. Furthermore, Sec. 3.2.3.3 outlines the procedure followed for focusing, alignment, and positioning during EBL. Finally, we report the recipe to develop the resist after exposure in Sec. 3.2.3.4.

3.2.3.1 Optimized Settings

When writing a pattern on the EBL machine, we have control over the following parameters: beam current, dose, and step size. In the first paragraph, we introduce the settings that determine the beam current. In the second paragraph, we define dose and step size, and present their relation to beam current as well as the role they play in pattern writing.

A typical electron beam writer works by accelerating electrons emitted from a hot filament down a column, through some focusing elements and an aperture, and finally onto the sample. The beam current is defined by the column filament, the acceleration voltage, and the aperture of the column. The column filament is a component of the EBL machine over which (as a user) we do not have control on. However, we can modify the acceleration voltage and the aperture of the column. The acceleration voltage sets the energy of the electrons incident on the resist. Low voltages lead to more forward scattering of the electrons as they come in contact with the resist, increasing both resist sensitivity and beam broadening (see Fig. 3.6a). Sensitivity can be thought of in terms of dwell time, which is the time required to expose an area given a dose and a beam current, as discussed in the next paragraph. Low acceleration voltages provide fast writing times. On the other hand, high voltages have the advantage of decreasing beam broadening at the expense of introducing back scattered electrons off the substrate (see Fig. 3.6a) that are responsible for most of the proximity effect [56]. The proximity effect is the phenomenon by which the scanned structure is different from the developed structure due to the interaction of the back scattered electrons with the resist and the incident electrons, resulting in over-exposure. Since ZEP520A is a sensitive resist, we could not go below acceleration voltages of 10 kV because the associated low dose

entails dwell times that are unachievable by the machine. To minimize the proximity effect, the acceleration voltage is set to 10 kV. The next parameter to choose is the aperture. Current increases with aperture size whereas depth of field (DOF) decreases with aperture size (see Fig. 3.6b). A small DOF offers tight focus but is sensitive to height variations. Since the resist layer is relatively thin (~ 150 nm) an aperture of $30\text{ }\mu\text{m}$ is used to produce a small DOF. Finally, the distance between the column and the sample is set to 10 mm (see Fig. 3.6b), which is a standard working distance for the machine we use. Together with the particularities of the machine's filament, these parameters produce a current of ~ 0.23 nA.

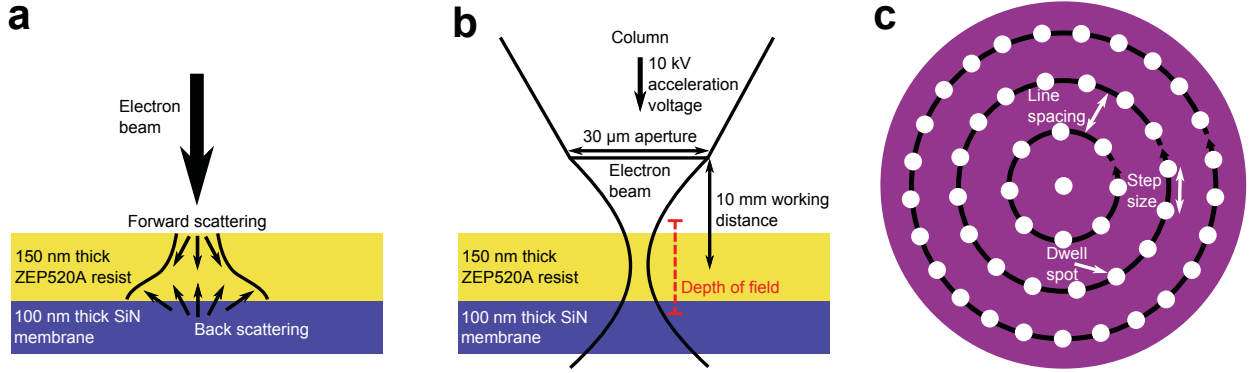


Figure 3.6: **a**, Resolution-limiting effect. When entering the resist, electrons experience forward scattering which leads to beam broadening. Electrons also reflect off the substrate, and can further expose the resist or interact with the incident electrons. This can lead to over-exposure, a phenomenon known as the proximity effect. **b**, Beam parameters used for exposure. **c**, Method to write smooth holes. The beam dwells on the white dots, and takes steps along concentric rings. The pattern is written outwardly, with the line spacing setting the distance between the rings.

The dose is defined by the resist type, substrate, pattern geometry, and beam current. Eq. 3.3 relates the dose (D) to the beam current (I), dwell time (T), and area to be exposed (A) [56]:

$$D = \frac{I \times T}{A}. \quad (3.3)$$

The area A is the product of the “step size” s and “line spacing” l (see Fig. 3.6c). The step size is the distance between two points at which the beam pauses for the dwell time. The line spacing is the distance between the lines used to expose the pattern. To pattern an array of holes with a ratio of radius to lattice constant of $\frac{r}{a} \sim 0.2$, the optimal dose is $\sim 50\text{ }\mu\text{C}/\text{cm}^2$. For the machine we are using, the parameter “beam speed” should be kept under 10 mm/s, which limits the achievable step size and line spacing. Indeed, given a dose and

a beam current, smaller steps translate to shorter dwell times and increase the beam speed parameter. With $D = 50 \mu\text{C}/\text{cm}^2$ and $I = 0.23 \text{ nA}$, we set $s = 25 \text{ nm}$ and $l = 50 \text{ nm}$ to achieve a beam speed of $\sim 9 \text{ mm/s}$. We found that the optimum method to write smooth holes is to follow concentric rings outwardly, as shown in Fig. 3.6c. This gives the beam time to settle initially in the center without distorting the outermost edge of the circle. The chosen parameters are compatible with a magnification of $500\times$, corresponding to a write-field (i.e. the maximum area that can be exposed without moving the stage) of $200 \times 200 \mu\text{m}^2$. Moving the stage leads to “stitching”, which is the positioning error associated with tiling of write-fields. In our case, this error is comparable to the lattice constant of the PhC. Since guided resonances in PhC slabs are very sensitive to disorder in lattice periodicity [57], stitching is not performed. This limits the PhC area to $200 \times 200 \mu\text{m}^2$, since the write-field size cannot be increased without decreasing the achievable resolution. For $a \sim 1500 \text{ nm}$ and $r \sim 300 \text{ nm}$, there are typically $\sim 10 - 30 \text{ nm}$ variations randomly across a given lattice.

3.2.3.2 Mask Files and Sample Preparation

The first step is to prepare the GSDII format files that the tool uses to write geometries. With Raith NanoSuite, a hole can be readily created with a pattern like that of Fig. 3.6c. As for the PhC, it is obtained by duplicating a single hole with a matrix function. The number of holes ($\sim 1.7 \times 10^3$) is set by the write-field area and the lattice constant. A file also contains a dose factor which allows for varying the dose around a nominal value. For a typical run, 3 samples containing 4 to 9 dies each are exposed. For each sample, the radius is varied from die to die, and so a file is prepared for each die.

Since the substrate is non-conductive, focusing can be a difficult task. In addition, ZEP520A is so sensitive that at high magnifications it literally melts. The presence of a metal grid under the resist is not sufficient to allow for careful focusing. Consequently, silver paint is manually added on top of the resist layer near the membranes, as shown in Fig. 3.7a. We carry out EBL at École Polytechnique de Montréal, so the samples are transported by hand in opaque Gel-Paks (BD series, X0 retention level).

3.2.3.3 Procedure

After the samples are loaded in the machine, the working distance is set to 10 mm . To navigate, one must define a coordinate system. This is done by defining two points P_1, P_2 which link sample coordinates (u, v) to the absolute coordinate system of the tool (x, y) . P_1

and P_2 are chosen to be the bottom left corner of two adjacent membranes, as shown in Fig. 3.7b. It is important to pick points that are separated by a few millimeters so that the determination of the angle θ (see Fig. 3.7b) relating the two coordinate systems is accurate. Afterwards, focusing, aperture alignment, and stigmation corrections are achieved using a metal chessboard engraved on the stage for this purpose.

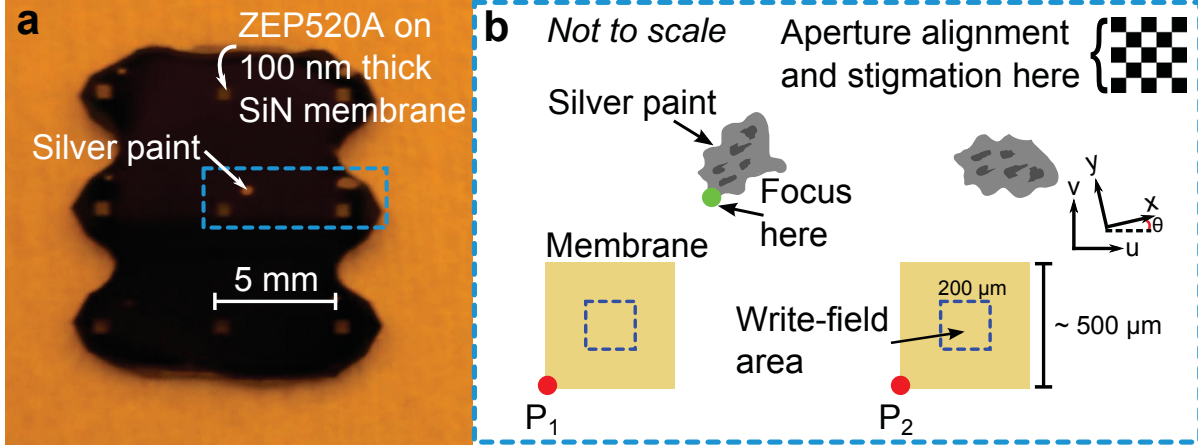


Figure 3.7: **a**, Silver paint is added near the membranes to facilitate focusing during EBL. **b**, Sketch of the relevant landmarks involved with the focusing, alignment and positioning procedures. P_1 and P_2 are points defined to link sample coordinates (u, v) to the absolute coordinate system of the tool (x, y) . Aperture alignment and stigmation adjustments are carried out with a metal chessboard engraved on the tool's stage, while focusing is performed closer to the membrane with the help of silver paint.

Now, the following steps are repeated for each die. The beam is moved to the silver paint near the die to be exposed, and the beam is re-focused to compensate for height changes. Then, a write-field alignment procedure is executed. This procedure requires the identification of distinct features, and so it is convenient to use the silver paint which appears grainy at this scale. To center the PhC pattern to the membrane, the size and position of the membrane is measured by positioning the beam at two corners of the membrane and recording the coordinates. Note that this maneuver must be done as quickly as possible to avoid exposing the resist; the stage is moved around the membrane, and the beam is not left unblanked at a fixed location for more than a few seconds. At this point, the die in question is ready to be patterned. For each die, patterning takes a few minutes.

3.2.3.4 Development

After the electrons have exposed the resist, the chip must be developed in a solution to remove the exposed areas. For ZEP520A, the developer is ZED-N50 (Zeon Chemicals). Held with tweezers, the chip is immersed vertically and gently immersed in the solution for 60 s. Afterwards, the chip is rinsed for 15 s in an IPA beaker, and dried with a N_2 spray gun. The liquid flow is directed so that the silver paint residues are projected away from the membranes. At this point, we have an etch mask to define the PhC, as shown in Fig. 3.8.

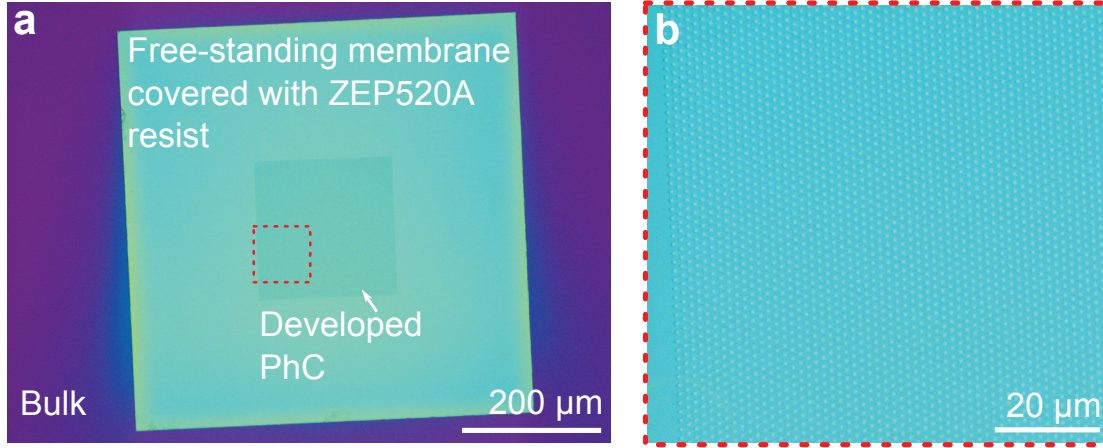


Figure 3.8: **a**, Free-standing SiN membrane with a PhC defined into the 150 nm thick ZEP520A resist. **b**, Zoom-in of the red-dashed region.

3.2.4 Dry Etching of the Photonic Crystal

In this section, we cover step 7 \rightarrow 8 of Fig. 3.2. The chips ought to be fixed on a carrier wafer to enter the RIE chamber. This is achieved by using a narrow strip of Kapton tape which leaves a gap between the chip and the carrier wafer, as shown in Fig. 3.9a. This is crucial otherwise the membranes break due to the pressure difference between trapped air under the membrane and chamber vacuum. The holes are etched through a 100-nm-thick membrane that is under ~ 1 GPa of tensile stress, compounding the fragility of the structure. The recipe presented in Table 3.1 inevitably leads to the PhC membrane breaking, as shown in Fig. 3.9b. To address this issue, we developed a low power recipe (Table 3.2) which has a $\sim 75\%$ yield and a SiN:ZEP250A selectivity of $\sim 3:1$.

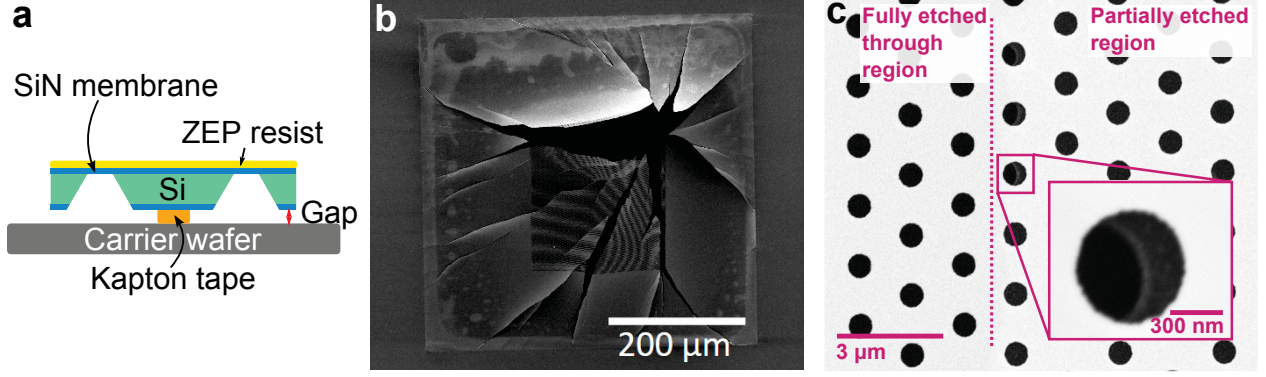


Figure 3.9: Dry etching of the PhC. **a**, A chip is fixed to a carrier wafer with Kapton tape to avoid trapping high-pressured air under the membrane, which would lead to its destruction in the low-pressured RIE chamber. **b**, A soft RIE recipe must be used to avoid breaking the PhC membrane. **c**, The softness of the RIE recipe can lead to regions of the PhC which are fully etched through, and regions which are not fully etched through. The inset shows the boundary between full etching and partial etching.

Etch time (s)	Power (W)	B-field (G)	Chamber pressure (mTorr)
200	100	0.0	30
Gas	CHF ₃	CF ₄	Ar
Flow (sccm)	30	70	7

Table 3.2: Parameters of the RIE recipe used in step 6 \rightarrow 7.

After RIE, the majority of the resist is stripped in Remover 1165 for 30 min at 60 °C. To remove resist remains, a more aggressive cleaning is accomplished with a 3:1 (H₂SO₄:H₂O₂) piranha solution for a duration of 15 min. A similar procedure as the one outlined in Sec. 3.2.2.1 is followed to manipulate the chips. In addition, the chips are rigidly fixed to the sample holder with screws to prevent them from floating around in the piranha solution. This two-step removal process is adopted because piranha reacts strongly with organic materials, and we observed that thick resist layers decrease device yield due to the resulting turbulence. Finally, the samples are dipped in HF and dried with methanol, as described in Sec. 3.2.2.1.

Once cleaned, the PhC membranes are inspected with an optical microscope and a scan-

ning electron microscope (SEM). Inspection of SEM images such as Fig. 3.9c reveal that samples are sometimes not completely etched through, which is attributed to the softness of the RIE recipe. Increasing power, magnetic field or etch time prohibitively decrease device yield. In the first two cases, the low yield is attributed to the fragility of the structure being etched. In the last case, it may be due to etching of the membrane from below when the majority of the holes are etched through. This phenomenon is observed in about half the samples, and the fully etched area typically exceeds 75 %. Further HF cleaning ensures that areas where the holes are not completely etched through are eliminated since HF etches SiN at a rate of ~ 1.8 nm/min. Figure 3.10a shows a SEM image of the patterned resist prior to stripping, whereas Fig. 3.10b shows an optical image of the PhC membrane after cleaning. The left inset is a SEM image of the PhC area, and the right inset is a zoom on a hole. Now that we have a PhC membrane with features that have a decent roughness compared to literature, the next step is to test the optical properties to which Chapter 4 is devoted.

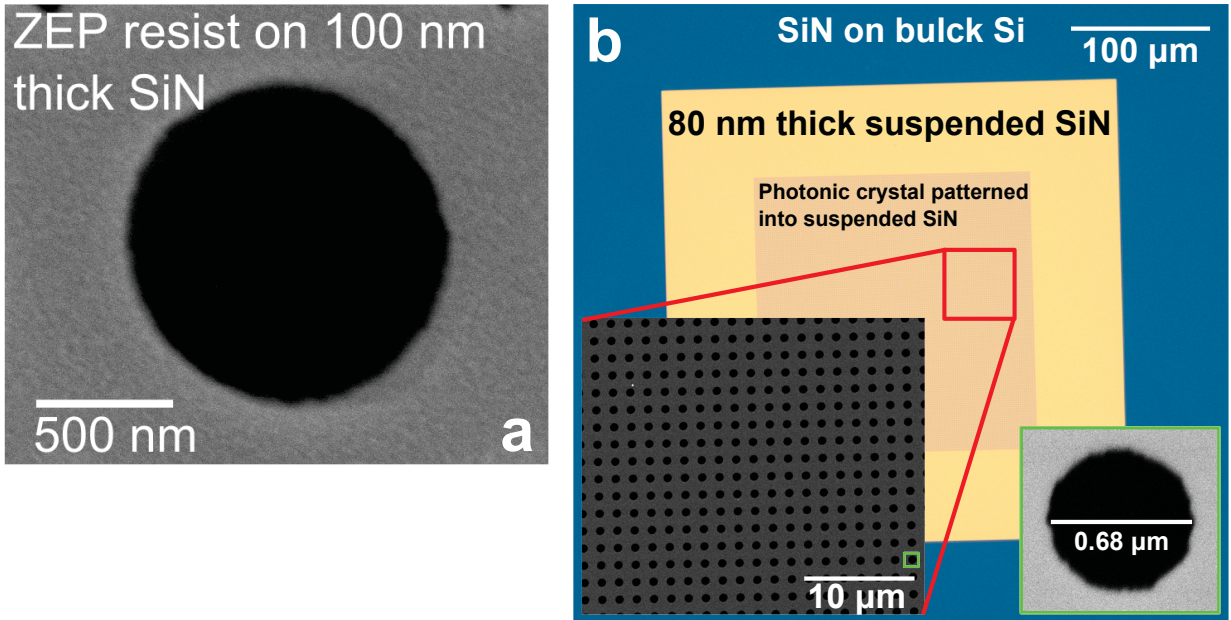


Figure 3.10: **a**, SEM image of a hole patterned in ZEP520A resist after it has been dry etched. **b**, Optical image of a PhC membrane after cleaning, with SEM insets showing the PhC area and hole roughness.

3.3 Alternative and Improvements

We take this opportunity to mention that we can also fabricate the PhC prior to releasing the membrane. In this case, the holes are patterned between stages 4 and 5 of Fig. 3.2. The advantage of this method is that it could in principle be compatible with the fabrication process flow of a device having the geometry considered in Ref. [10]. The disadvantage of this alternative is that the holes are patterned on a thicker substrate which introduces more back scattering of the electrons, thereby increasing the hole roughness. One way to tackle this issue is to deposit a Cr film (~ 5 nm) on top of the electron beam resist that acts as a discharge layer. In addition, we plan to further improve the current RIE recipe.

Chapter 4

Photonic Crystal Membrane Optical Characterization

In this chapter, we present the experimental setup and method used to extract the PhC membrane's transmission and reflection spectra at normal incidence, and we report our results. In Sec. 4.1 we introduce the experimental setup and walk through the different stages of the apparatus. Then, we move on to Sec. 4.2 where we outline the procedure followed to acquire data. Finally, in Sec. 4.3 we describe how the acquired data is treated to obtain the transmission and reflection spectra. This will set the stage for the discussion of our results in Sec. 4.4.

4.1 Experimental Setup

The experimental setup is shown in Fig. 4.1. The idea is to focus a laser beam onto the PhC membrane, and sweep the laser wavelength while its intensity is measured by a photodiode in three different arms (transmission, reflection, and calibration). From these three data sets, we retrieve the transmission and reflection spectra of the PhC membrane.

4.1.1 Beam Shape Control

The components are fixed on a low vibration optical table. The light source is a tunable diode laser (New Focus model 6328) with a cavity formed by a high-reflectivity coating at one end of a diode, a collimating lens, a diffraction grating, and a tuning mirror. The wavelength is set by a motor which controls the angle of the tuning mirror [58]. The motor can achieve a coarse tuning resolution of 0.02 nm with a repeatability of 0.1 nm. A piezoelectric allows for finer wavelength tuning resolution. The bandwidth of the laser is 1510 - 1584 nm, and it typically outputs ~ 9 mW. The laser's output beam is not Gaussian shaped. Scanning slit optical beam profiler measurements reveal that the $\frac{1}{e^2}$ diameter of the beam may differ up to a factor of 2 for orthogonal axes. To correct for this, the beam is coupled into a single-mode optical fiber which acts as a spatial filter with a Gaussian profile. The fiber mode field

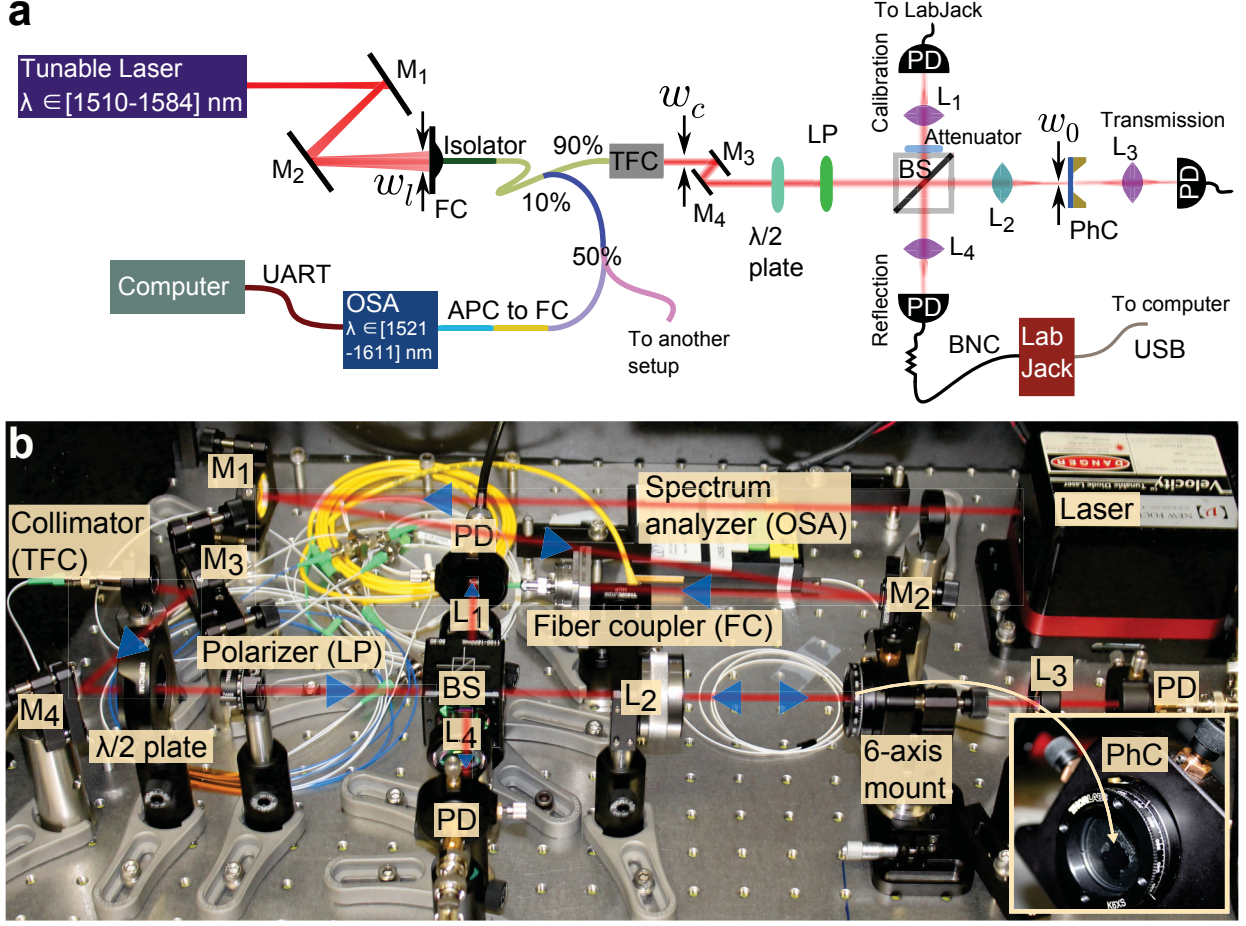


Figure 4.1: **a**, Schematic of the experimental setup used to characterize the PhC membrane. Light from a tunable laser is coupled into an optical fiber and divided toward an optical spectrum analyzer (OSA, Optoplex C+L band) and a TFC. The OSA measures the laser wavelength, and the TFC produces a collimated Gaussian shaped beam. The beam is split between a calibration arm, a transmission arm and a reflection arm. The intensity of the beam is measured with photodiodes, and the resulting voltage is recorded by a LabJack. **b**, Photograph of the experimental setup. The inset shows a mounted chip containing four PhC membranes.

diameter D and free space input beam diameter w_l are related to the focal length f of the collimating lens within the fiber coupler (FC) via [59]

$$f = \frac{\pi D w_l}{4 \lambda}, \quad (4.1)$$

where λ is the wavelength of the input beam. The fiber coupler is positioned at a location where the free space beam diameter satisfies Eq. 4.1. Mirrors M_1 and M_2 control the angle of arrival of the beam at the fiber coupler. The coupling is maximized by adjusting these mirrors

and the orientation of the lens within the fiber coupler.¹ The achieved coupling efficiency is 0.4. Once the light is in the fiber, it passes through an isolator to prevent reflected light from further optical components to attain the laser, and a splitter which sends it toward a triplet fiber collimator (TFC) and a OSA with a 90:10 ratio. The OSA measures the wavelength of the laser, and can be used to determine whether or not the laser is mode hopping. The TFC uses air-spaced triplet lenses to minimize beam divergence and wavefront error. Upon leaving the TFC, the collimated beam has a diameter of $w_c = 2.0$ mm. Mirrors M_3 and M_4 then steer the beam so that the latter hits subsequent optics at normal incidence. The role of these optics is to focus the beam within the PhC area on the membrane with a well-defined polarization and to collect the transmitted and reflected light, which we turn to in the next section.

4.1.2 Beam Path

The light emitted by the laser is not linearly polarized, and its polarization changes as the wavelength is swept. In contrast, the results of the simulations of Chapter 2 are obtained under the assumption of a linear polarization that is independent of the wavelength. Therefore, a half-wave plate followed by a linear polarizer is added so that the polarization of the light landing on the PhC membrane is linear, and can be rotated in the plane of the PhC membrane. The half-wave plate mirrors the polarization vector through the plane formed by its fast axis and the direction of propagation whereas the linear polarizer absorbs light that is polarized perpendicularly to its transmission axis with an extinction ratio of 100 000:1.

The linearly polarized light is separated ($\sim 50:50$) via a non-polarizing beam splitter (BS) toward a calibration arm and a transmission arm. Upon reflection onto the PhC membrane, light is sent backwards to the beam splitter, and separated between the reflection arm and the original path. The calibration arm serves as a reference to allow for a relative measurement of the PhC membrane's transmission and reflection spectra, and monitors drifts in the laser power. Section 4.3 discusses how the transmission and reflection spectra are derived from the signals obtained with the three different arms. For each arm, a photodiode converts the electric field intensity into an electric current, which is in turn converted to a voltage via a resistor. The photodiode is made of InGaAs semiconductor, and has a responsivity of $\mathcal{R} \simeq 1.1$ A/W over the laser's tunable range [60]. For a load resistance R_L and incident

¹In this case the number of degrees of freedom is over-specifying the adjustment of the beam position, but we adopt this technique for its practicality.

power P , the output voltage is given by [60]

$$V = P \times \mathcal{R} \times R_L. \quad (4.2)$$

The voltage is recorded with a LabJack U6-Pro, a multifunction DAQ connected to a computer with a USB port. The LabJack is set with a $\times 10$ gain, which is compatible for signals up to 1 V. Lenses L_1 , L_3 and L_4 have a focal length of 3 cm, which is sufficient for converging the beam within an area $< 0.79 \text{ mm}^2$, corresponding to the active area of the photodiode. The calibration arm has a 10^{-3} absorptive attenuator to prevent unwanted reflections of its photodiode from reaching the photodiode located in the reflection arm. The photodiode in the transmission arm also poses this problem. To avoid minimizing the signal with an attenuator, the transmission photodiode is instead slightly tilted.

The laser light is focused upon the PhC using L_2 , a UV fused silica bi-convex lens designed to minimize wavefront distortion and scattering. It has an anti-reflection coating optimized for 1.00 - 1.55 μm , and a focal length $f = 9.5 \text{ cm}$. The beam waist at the PhC membrane, $\frac{w_0}{2}$, is estimated by solving [61]

$$w_c^2 - w_0^2 \left(1 + \left(\frac{4 \lambda f}{\pi w_0^2} \right) \right) = 0. \quad (4.3)$$

The confocal parameter b is twice the distance from the beam waist to the place where the area of the beam cross section is doubled, and is given by [14]

$$b = \frac{\pi w_0^2}{2\lambda}. \quad (4.4)$$

For $w_c = 2.0 \text{ mm}$ and $\lambda = 1550 \text{ nm}$, this translates to $w_0 = 45 \text{ }\mu\text{m}$ and $b = 0.5 \text{ mm}$. The confocal parameter gives the range within which the PhC membrane should be positioned along the beam axis. Optical beam profiler measurements yield $w_0 = 60 \text{ }\mu\text{m}$ (with at most 2 % asymmetry for orthogonal axes), and show that the peak position of the beam fluctuates by at most 10 μm at its waist. These fluctuations are attributed to the beam profiler itself (it has a rotating component that shakes) rather than to the laser beam. For comparison, the PhC area on the membrane is $200 \times 200 \text{ }\mu\text{m}^2$. Polarimeter measurements reveal that the ellipticity of the polarization is smaller than 2° .

4.2 Method

In this section, we summarize the steps followed to acquire the signal from the three arms discussed above. We will show in Sec. 4.3 that these signals can be used to determine the

fraction of incident light that is transmitted, reflected, and lost by the PhC membrane.

4.2.1 Laser Control

The laser power is most stable by setting the diode temperature to 16 °C, whereas the cavity temperature is factory regulated to 30 °C. For a fixed wavelength, power fluctuates ~ 0.5 % around its mean value, although it can drift away by ~ 1 % over a longer period of time (20 min). To avoid power drift, the laser employs a constant power mode which involves a ~ 20 ms feedback loop. Furthermore, the laser can either be set in “track” mode (wavelength actively controlled by tuning motor), or in “ready” mode (open loop operation). The wavelength is more stable in ready mode than in track mode [58] with the drawback that it cannot be swept.² Therefore, the laser is operated in track mode when the wavelength is swept. In the next paragraph, we investigate the parameters which control the sweeping of the wavelength.

A laser sweep is defined by four parameters: start / stop wavelengths, step size, and sleep time in between steps (i.e. time given to the laser to settle before it moves on to the next wavelength). The effect of the laser settings are investigated in Fig. 4.2, where no PhC membrane is present for all the curves shown. Figure 4.2a shows the recorded voltage from the photodiode in the transmission arm when the combination of the half-wave plate and linear polarizer is absent. The signal exhibits a slow and a fast modulation. The slow modulation is attributed to the wavelength dependence of the laser power due to residual etalon effects from reflections at the facet of the diode laser [58]. This slow modulation can be avoided by setting the laser to a different temperature for different wavelengths. However, it is impractical to change the temperature when sweeping the wavelength, as temperature requires a stabilization time of ~ 30 min. It will be shown in Sec. 4.3 that this slow modulation can be accounted for by comparing with the power monitored at the calibration arm diode. The fast modulation may be due to an interference effect within the beam pathway. Although precautions are taken (fiber isolator, anti-reflection coated optical components, tilted photodiodes), it appears that standing waves still form. The period of the fast modulation (~ 2 nm) translates to a standing wave with a length scale of ~ 1 mm, which could correspond to several components in the setup. For example, the distance between the photodiode’s detector and protecting glass is about 1 mm. Now, the effect of

²For technical reasons, the laser automatically sets itself into track mode when it is remotely addressed for a wavelength sweep.

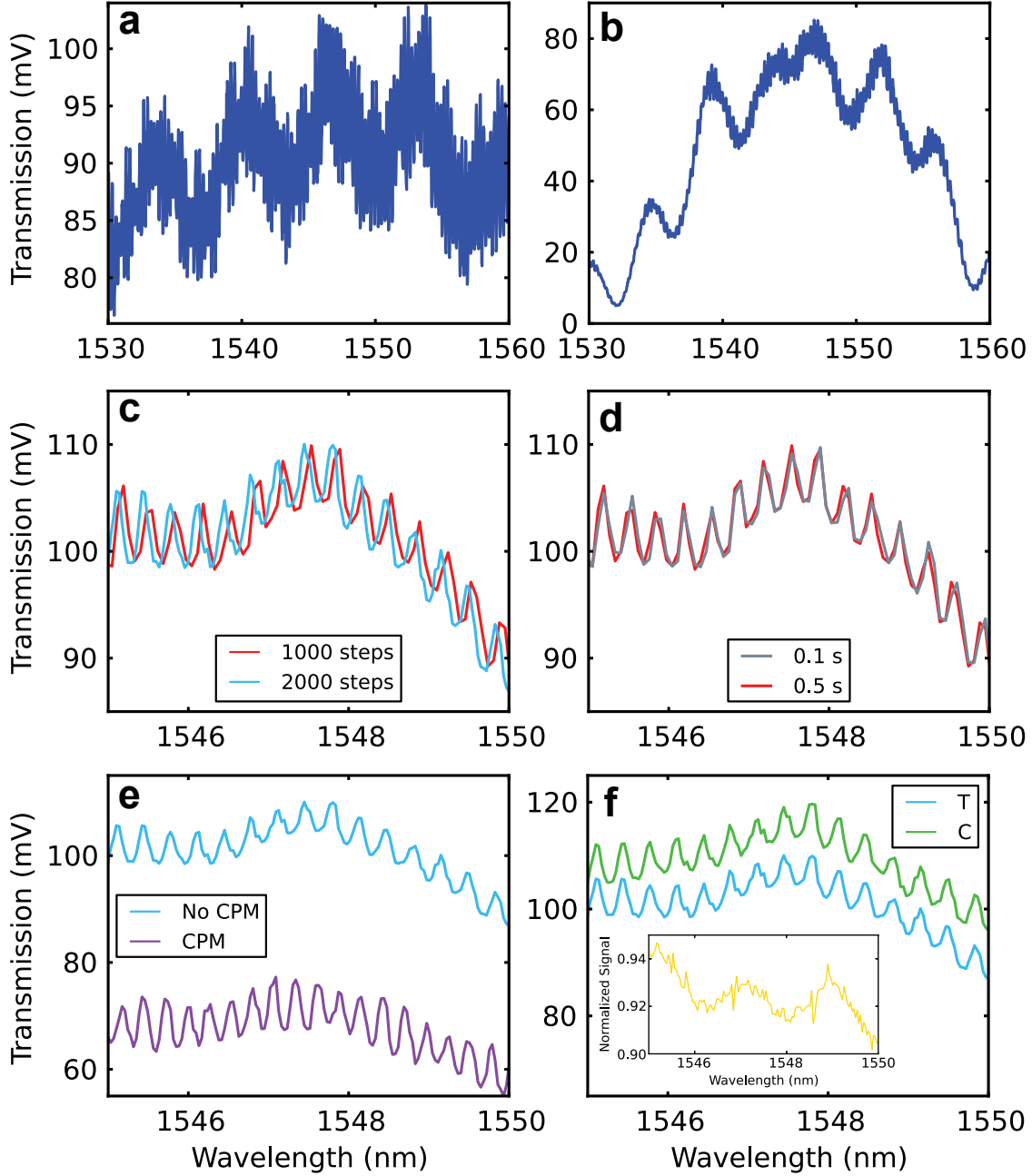


Figure 4.2: **a**, Transmission arm voltage in the absence of a PhC membrane, a half-wave plate, and a linear polarizer. **b**, Same signal as in **a**, with the addition of a half-wave plate and a linear polarizer. **c**, Transmission arm voltage for two different number of laser steps, corresponding to a resolution of 0.70 nm/step and 0.35 nm/step respectively. **d**, Transmission arm voltage for two different sleep time values. **e**, Comparison between the laser operated in CPM, and in non-CPM. **f**, Voltage acquired simultaneously in the transmission arm (T) and calibration arm (C). The inset shows the ratio of the two curves ($\frac{T}{C}$).

adding the combination of a half-wave plate and a linear polarizer to the setup is shown in Fig. 4.2b. For certain wavelengths, the voltage approaches zero, which is due to the laser’s changing polarization as its wavelength is swept through the combination of the half-wave plate and linear polarizer. Some wavelengths have a polarization such that upon passage through the half-wave plate, the latter is rotated 90° away from the transmission axis of the linear polarizer, thereby suppressing their transmission. The signal to the amplitude of the fast modulation ratio is constant from Fig. 4.2a to Fig. 4.2b. The transmission arm voltage is plotted for two different step size values in Fig. 4.2c. For the wavelength range shown, 1000 steps and 2000 steps correspond to a resolution of 0.70 nm/step and 0.35 nm/step respectively. Increasing the number of steps does not improve the signal to fast modulation ratio. The phase difference between the two curves indicates laser drift between the two measurements. In Fig. 4.2d, the transmission arm voltage is plotted for two different sleep time values. Again, there is no significant difference between the two signals. The signals plotted in Fig. 4.2e are measured under the same conditions, with the exception of the laser being set with or without constant power mode (CPM). In this case, the signal to fast modulation ratio is higher without CPM, and the period of the modulation is longer without CPM. Consequently, the laser is not operated under CPM. Fig. 4.2f shows the voltage acquired simultaneously in the transmission arm (T) and calibration arm (C). The offset between the two curves indicates that the beam splitter is not exactly 50:50, and that the modulation is correlated from arm to arm. In addition, the inset shows the ratio of the two curves ($\frac{T}{C}$). A modulation with a different period emerges, and the decreasing slope of the curve suggests that the beam splitter is dispersive or that the collection efficiency of the photodiodes is wavelength dependent. These effects can also be accounted for (see Sec. 4.3). The upshot of Fig. 4.2 is that increasing step resolution and sleep time after a certain point does not improve the quality of the signal, and that modulations are always present.

4.2.2 Graphical User Interface

The experimental setup is interfaced through a program written with Spinmob, a Python library designed for visualizing and handling ASCII data files, and for generating GUIs. Spinmob is available at <https://github.com/Spinmob/spinmob/wiki>. Figure 4.3 displays the essential features of the program. The top panel shows the voltages recorded from the three arms. The signals are recorded live and simultaneously. The settings portion allow for communication with the laser, LabJack and OSA. When data is saved, the information contained in the settings is automatically written to a file. The bottom panel shows ratios

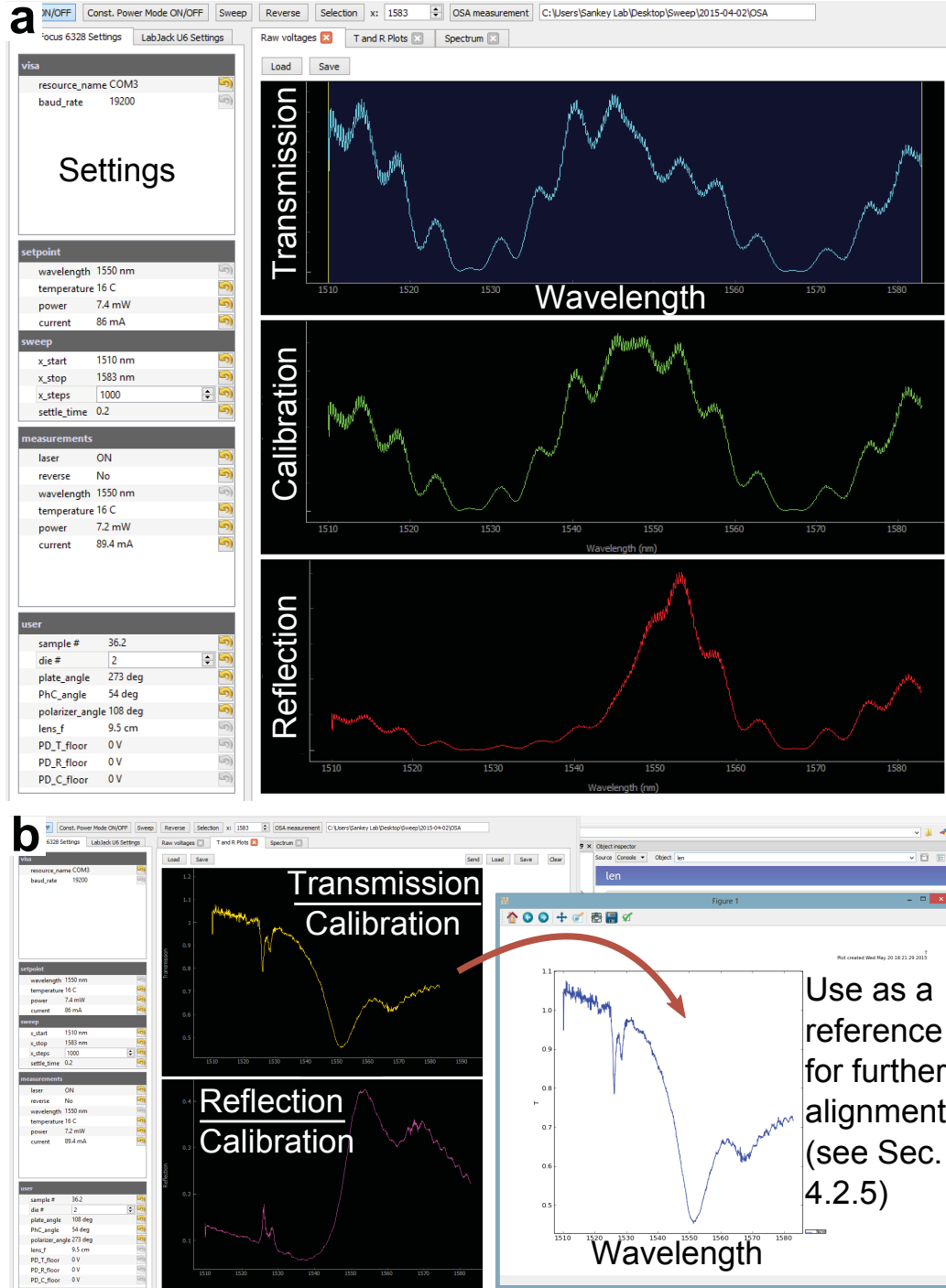


Figure 4.3: GUI of the experiment. **a**, For each arm, the signal from the photodiode is recorded live. The settings area interfaces the laser, LabJack, and OSA. **b**, Ratios of the signals presented in the top panel constitute a crude approximation to the transmission and reflection of the PhC membrane. The reference graph on the right allows for systematic alignment described in Sec. 4.2.5.

of the measured voltages. It is a crude approximation to the transmission and reflection of the PhC membrane. After a sweep is done, the data can be plotted onto a reference graph, which is handy when systematic alignment is performed (see Sec. 4.2.5). Finally, the GUI offers a tab which plots and saves the OSA spectra as the wavelength is swept. An OSA spectrum allows to measure the laser's wavelength, and to make sure the laser is operating correctly.

4.2.3 Optical Spectrum Analyzer

During a sweep, the OSA takes a spectrum each time the laser is stepped to measure its wavelength. Figure 4.4 shows a spectrum acquired over the full bandwidth of the OSA (black curve) for a given laser wavelength. The gray curve is the noise floor of the OSA. To

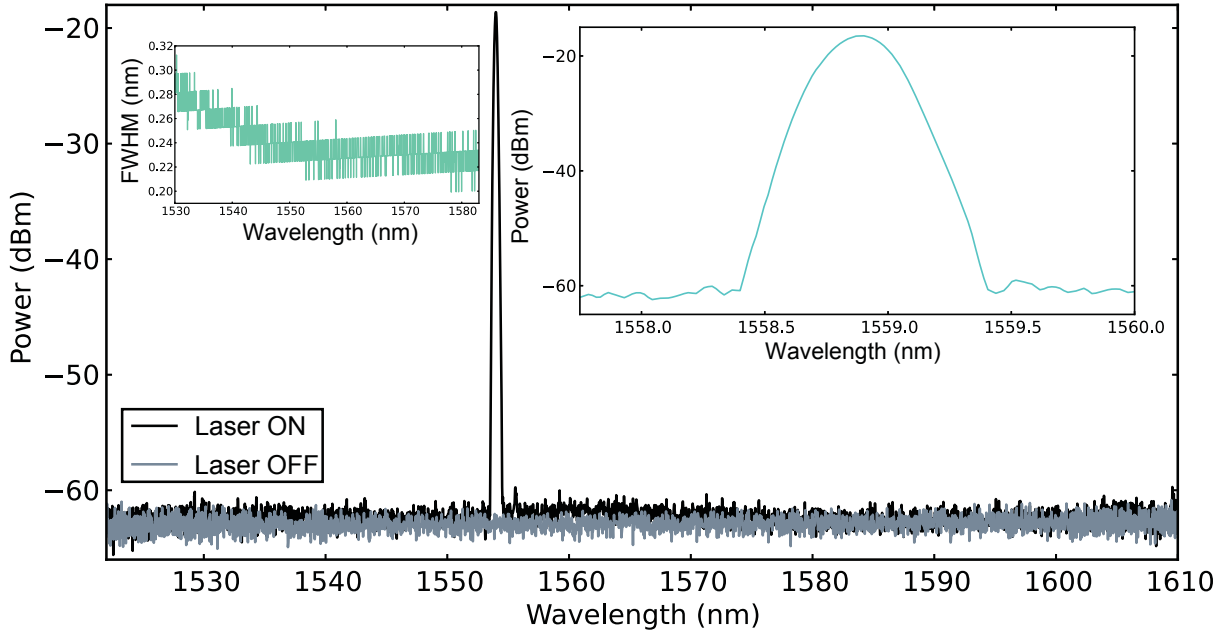


Figure 4.4: OSA spectrum over its full bandwidth for a given laser wavelength (black), and noise floor of the OSA (gray). The left inset plots the FWHM of the peak as a function of wavelength. The right inset shows a typical spectrum used to measure the laser wavelength.

estimate the off-peak power contribution, the difference between the area under the black curve and the area under the gray curve (DA_{total}) is compared to the difference between the area under the black curve and the area under the gray curve away from the peak (DA_{away}). The ratio $\frac{DA_{away}}{DA_{total}}$ indicates that the fractional power originating from wavelengths away from the peak is 0.18 %. In addition, an upper bound for the laser noise power contribution can be obtained from the ratio of the area under the gray curve to the area under the black curve:

$\frac{A_g}{A_b} = 1.2\%$. The left inset of Fig. 4.4 shows the full width at half maximum (FWHM) of the laser peak as a function of wavelength. The FWHM is obtained from a high-resolution OSA scan in the vicinity of the laser wavelength, as depicted in the right inset. The largest FWHM is 0.3 nm, and occurs for small wavelengths. The peak position of the right inset constitutes the measurement of the laser wavelength.

Figure 4.5 relates the laser wavelength setpoint to the difference between the laser wavelength setpoint and the wavelength measured by the OSA. This calibration curve is useful in the event that the OSA is unavailable; one can use the fit to relate the laser wavelength setpoint to the true wavelength. The fit residuals are displayed in the bottom inset. The top inset shows the laser step size obtained from the OSA by taking the peak wavelength difference between consecutive spectra. For the data shown, the laser is set to a sweep of 2000 steps over 1530 - 1584 nm, which translates to a step size of 0.027 nm. This number corresponds roughly to the mean value of the blue curve, which features a slightly positive slope. With this technique we can determine the wavelength to within < 0.05 nm, which is sufficient to resolve the few-nanometers features of the PhC's resonance.

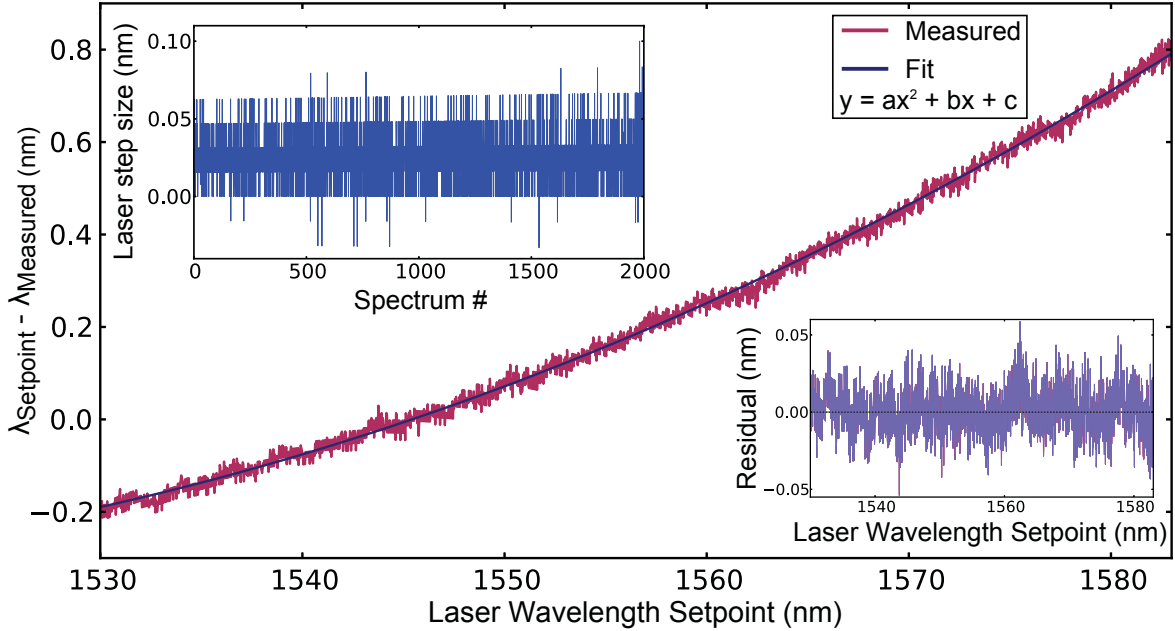


Figure 4.5: Difference between the laser wavelength setpoint and the wavelength measured by the OSA as a function of laser wavelength setpoint (burgundy). The navy blue curve is a quadratic fit to the data. The bottom inset shows the fit residuals. The top inset shows that the step size written to the laser is not always equal to the difference in wavelength from consecutive OSA spectra.

4.2.4 Photonic Crystal Membrane Mounting

The PhC membrane is mounted on a 6-axis stage (Thorlabs K6XS). Three knobs allow for adjusting tip and tilt ($0.3^\circ/\text{rev}$), and for translating the PhC membrane along the beam axis (referred to as the z -axis, $318\text{ }\mu\text{m}/\text{rev}$ ³, 6.35 mm travel range). Two translation screws ($254\text{ }\mu\text{m}/\text{rev}$, 2 mm travel range) allow for movement along the x and y -axes forming the plane perpendicular to the beam axis. Finally, the stage cell allows for 360° rotation. The PhC membrane is mounted into the cell with a hollow cylindrical adapter. A sample typically contains four $5 \times 5\text{ mm}$ dies. The sample is fixed onto the adapter with SEM tape, and with the PhC membrane to be investigated centered above the hollow part of the cylinder. The inset of Fig. 4.1b shows a close-up of the PhC membrane's chip mounted upon the stage. However, we later decided to flip the cylinder so that the membrane faced backwards; this positioned it closer to the plane of the three knobs and somewhat decoupled tilt from x - y movement. In practice, rotating the three knobs by exactly the same amount to exclusively produce z movement is inefficient, and so the 6-axis stage is mounted on a z translational stage (Thorlabs MS1S) which is actuated by a travel micrometer ($0.5\text{ mm}/\text{rev}$, 6.5 mm travel range).

4.2.5 Photonic Crystal Membrane Alignment

During this process, the photodiodes are connected to an oscilloscope to obtain immediate feedback. The first step to find the PhC membrane's resonance is to set the laser wavelength to the one predicted by the simulation. Then, the membrane is found by aligning by hand the sample and observing the transmission channel. Once this is completed, the stage is fixed to the optical table approximately at the focal length of L_2 (marked on the table). The next step is to roughly align the membrane perpendicular to the beam using the tip/tilt knobs to maximize the reflection signal. Afterwards, the PhC area is found by translating the sample along the x and y -axes. On the oscilloscope, the PhC area manifests itself by a drop on the transmission channel, and an increase on the reflection channel. At this point, the beam roughly hits the PhC area in its center at normal incidence, and the latter is positioned within $\sim 2\text{ mm}$ of the waist. Next, the laser wavelength is swept (with the photodiodes connected to the LabJack) to narrow down the location of the resonance. For finer alignment of the PhC, one must take a systematic approach. This is done by sweeping the laser in the region close to the resonance, and subsequently vary a parameter (i.e. a knob or a screw). This is performed iteratively until no further improvement is observed. An example step of the

procedure is illustrated in Fig. 4.6. The plotted transmission corresponds to the ratio of the voltage measured from the transmission arm to the calibration arm, as in the inset of Fig. 4.2f. Contrary to our expectations and the measured beam waist, we did not observe

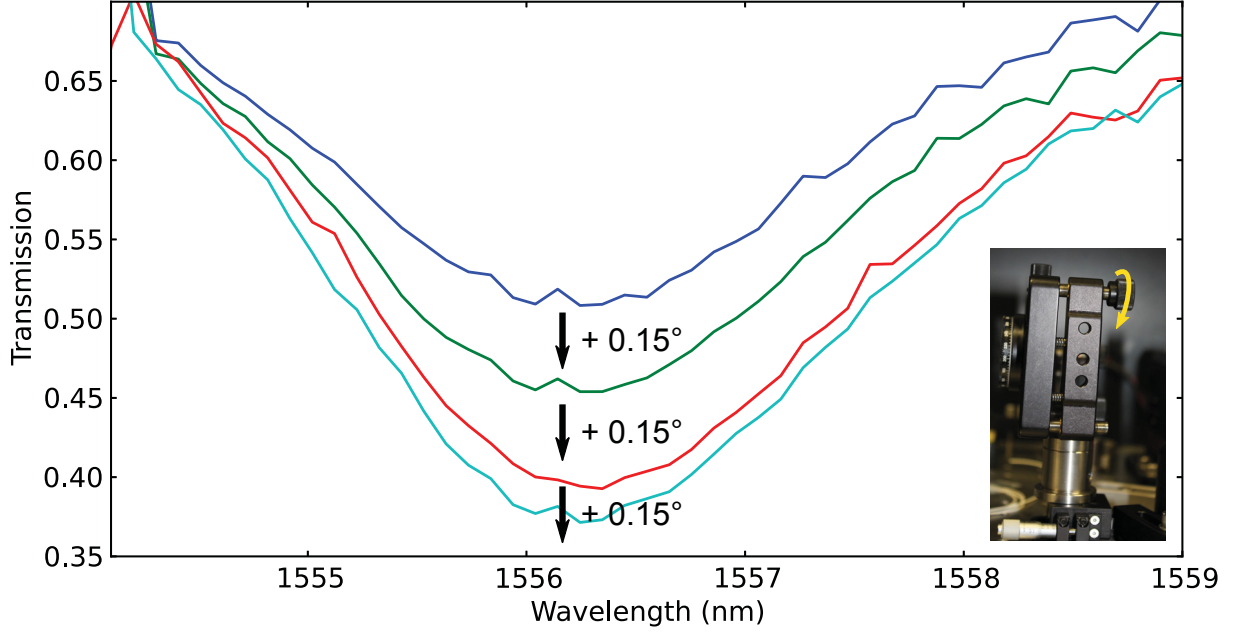


Figure 4.6: The PhC membrane is aligned by varying systematically a parameter until no further improvement is observed. For the curves shown, the PhC membrane is tilted by turning a knob halfway each time, which translates to a $\sim 0.15^\circ$ tilt.

a sharp transition between high and low-transmission regions of the membrane so there is likely room for improvement to this setup.

4.3 Data Treatment

This section describes how the data is treated to obtain normalized transmission and reflection of the PhC membrane as a function of wavelength. The relevant part of the setup is shown in Fig. 4.7. To obtain the normalized transmission, four signals are measured:

- A_{PhC} : voltage from transmission arm in the presence of a PhC membrane
- C_{PhC} : voltage from calibration arm in the presence of a PhC membrane
- A_{empty} : voltage from transmission arm in the absence of a PhC membrane
- C_{empty} : voltage from calibration arm in the absence of a PhC membrane

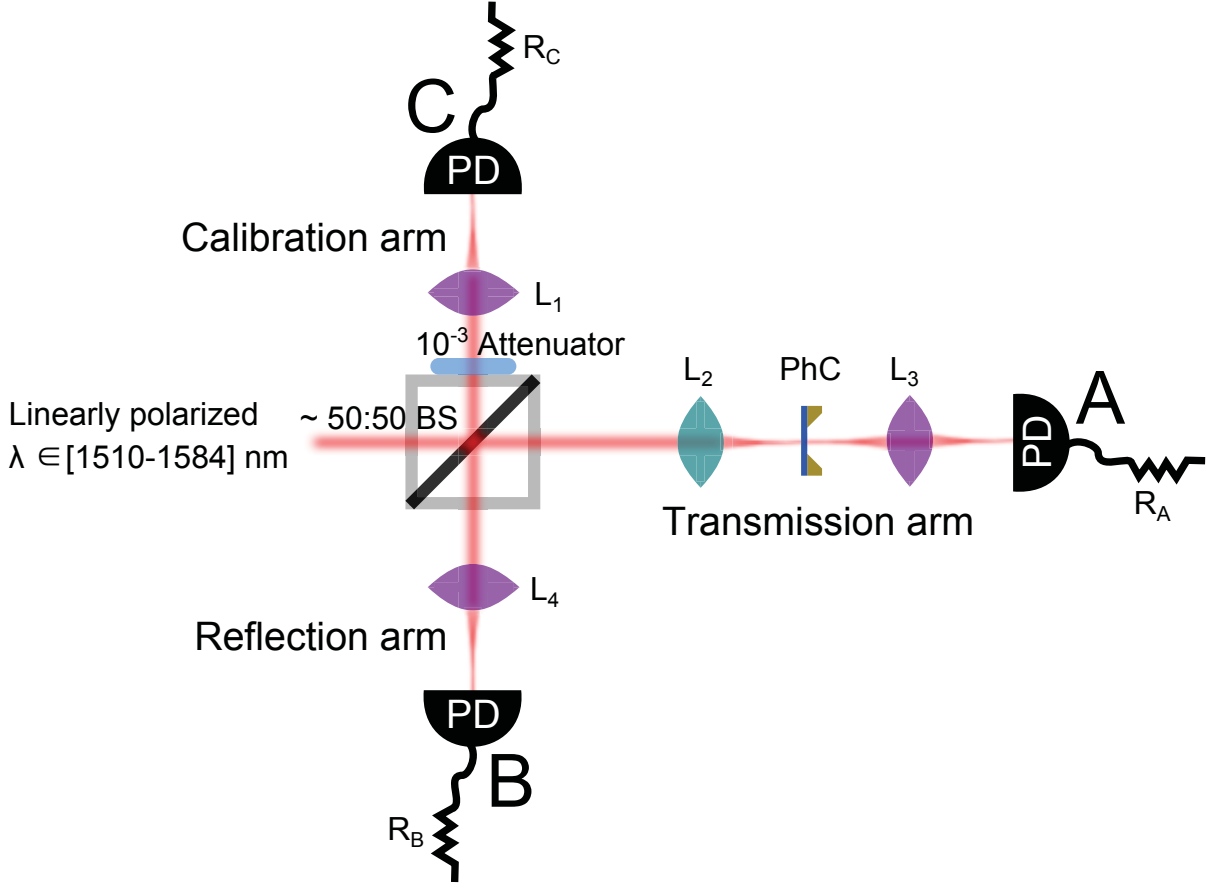


Figure 4.7: Data acquisition portion of the setup. The intensity of the beam is recorded with a photodiode at the end of each arm. The signals mentioned in the text are associated with the letters A , B and C .

A_{PhC} and C_{PhC} can be measured simultaneously, and A_{empty} and C_{empty} can be measured simultaneously. Figure 4.8 shows A_{PhC} (blue curve), C_{PhC} (gray curve), and B_{PhC} (red curve), the voltage from the reflection arm in the presence of a PhC membrane. As noted in Sec. 4.2.1, the slow modulation is due to the combination of the wavelength dependence of the laser power and polarization, whereas the fast modulation may be an interference effect along the beam pathway. For certain wavelengths, the voltage for the three arms simultaneously approaches zero, as explained in Sec. 4.2.1. At these wavelengths, the signal can be indistinguishable from the photodiode's dark voltage. To correct for this, the quantities A_{PhC} , C_{PhC} , A_{empty} and A_{empty} are also measured with the half-wave plate rotated by 45° , thereby shifting the wavelengths for which the voltage is essentially zero. This effect is displayed in the top panel of Fig. 4.9. The quantities measured with the half-wave plate rotated by 45° are referred to with the superscript “45”. The sum of the two signals of the

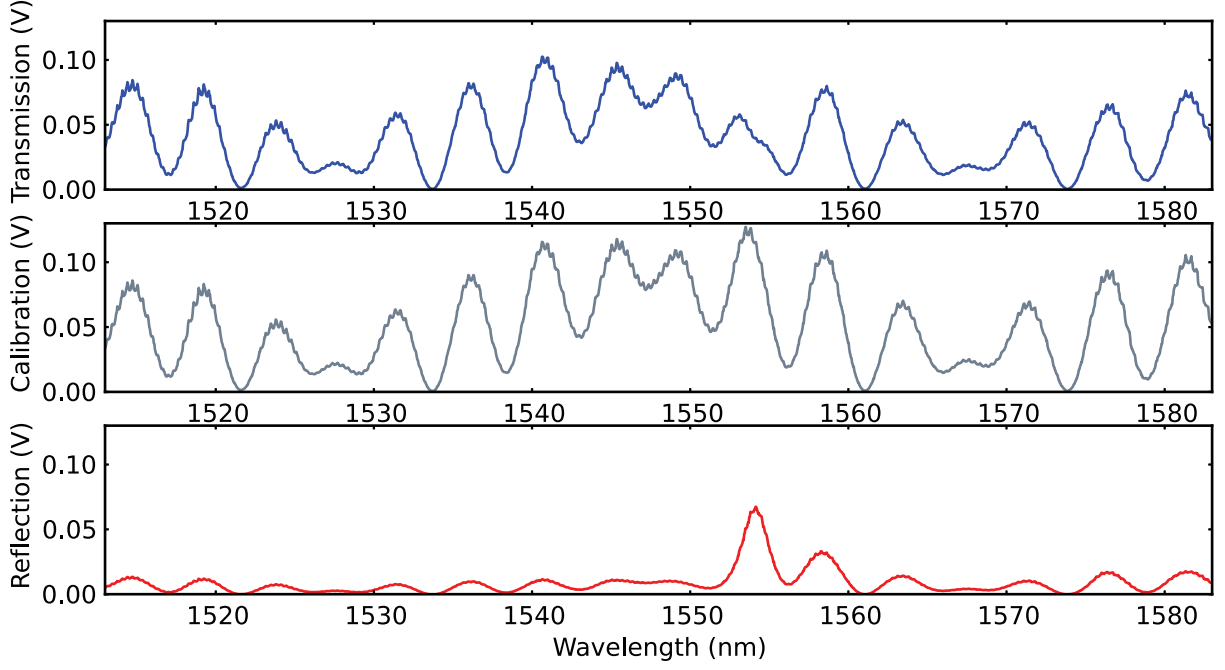


Figure 4.8: Voltage recorded simultaneously in the transmission arm (blue), calibration arm (gray), and reflection arm (red) as a function of wavelength, when a PhC membrane is present.

top panel is plotted in the bottom panel. The ratio of the amplitude of the fast modulation to the signal is approximately the same for all curves shown in Fig. 4.9. However, for the case of the slow modulation, it is simply a power modulation so that the sum of these two complementary signal improves the signal to noise ratio.

Now, A_{PhC} can be written as (see Fig. 4.7)

$$A_{PhC} = \{\mathcal{I}(t_1, \lambda) \times BS_A(\lambda) \times L_2(\lambda) \times T(\lambda) \times L_3(\lambda)\} \times \{PD(\lambda, R_A)\} + A_0 + \mathcal{N}_A(t_1), \quad (4.5)$$

where $\mathcal{I}(t_1, \lambda)$ is the electric field intensity impinging on the beam splitter. The effect of an optical component on the electric field intensity is modeled through a response function, which relates the input electric field intensity to the output electric field intensity. It is assumed that these response functions are time independent. $BS_A(\lambda)$ is the response function of the beam splitter for the transmission arm, and L_2, L_3 are the response functions for the lenses. $T(\lambda)$ is the response function for the PhC membrane, and is the quantity to be extracted. $PD(\lambda, R_A)$ denotes the response function of the photodiode, and depends on the resistor chosen to terminate it. It converts electric field intensity to a voltage. A_0 is the dark voltage of the photodiode. $\mathcal{N}_A(t_1)$ is random noise introduced in the voltage signal from the transmission arm and the laser at time t_1 . It is assumed to be frequency independent, and

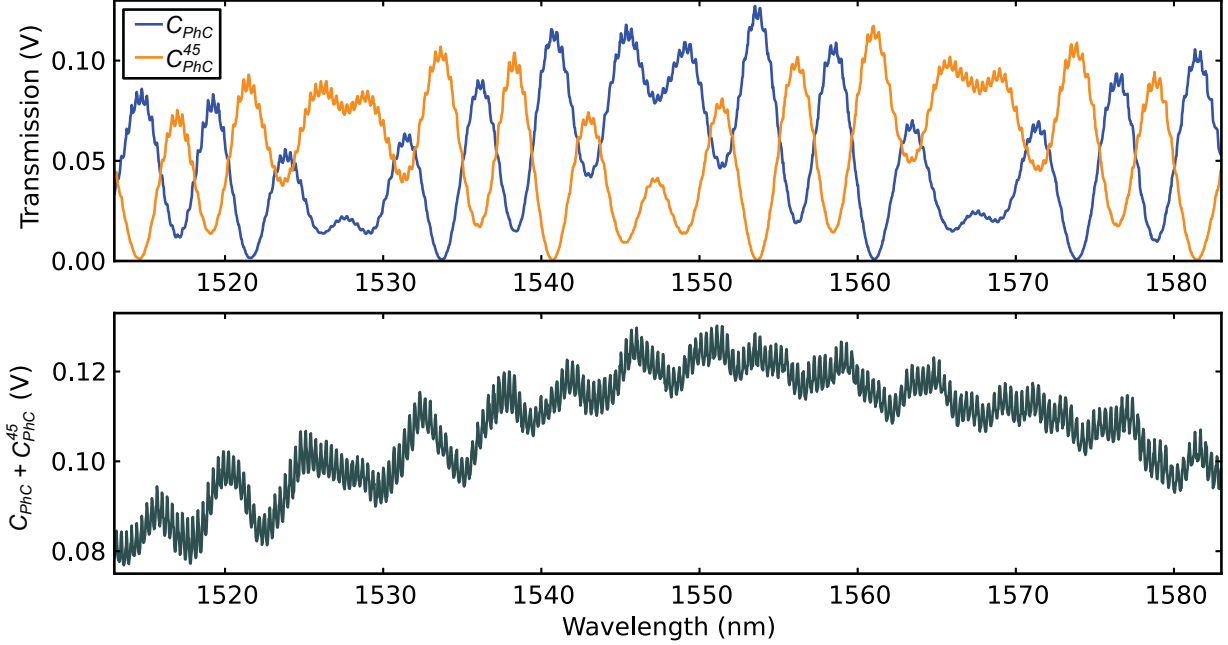


Figure 4.9: The top panel shows the voltage recorded in the calibration arm for a difference of 45° in the half-wave plate rotation. The bottom panel plots the sum of the curves in the top panel.

to have a Gaussian probability distribution centered at 0 V.

Similarly, C_{PhC} is written

$$C_{PhC} = \{\mathcal{I}(t_1, \lambda) \times BS_C(\lambda) \times \mathcal{A}(\lambda) \times L_1(\lambda)\} \times \{PD(\lambda, R_C)\} + C_0 + \mathcal{N}_C(t_1), \quad (4.6)$$

where $\mathcal{A}(\lambda)$ is the response function of the attenuator. Since A_{PhC} and C_{PhC} are measured simultaneously, the time is the same in Eqs. 4.5 and 4.6. As described earlier, A_{PhC} and C_{PhC} are also measured with the half-wave plate rotated by 45° to avoid $\mathcal{I} \sim 0$, and are written

$$A_{PhC}^{45} = \{\mathcal{I}(t_2, \lambda) \times BS_A(\lambda) \times L_2(\lambda) \times T(\lambda) \times L_3(\lambda)\} \times \{PD(\lambda, R_A)\} + A_0 + \mathcal{N}_A(t_2), \quad (4.7)$$

$$C_{PhC}^{45} = \{\mathcal{I}(t_2, \lambda) \times BS_C(\lambda) \times \mathcal{A}(\lambda) \times L_1(\lambda)\} \times \{PD(\lambda, R_C)\} + C_0 + \mathcal{N}_C(t_2). \quad (4.8)$$

A_0 and C_0 can be eliminated from Eqs. 4.5, 4.6, 4.7, and 4.8 by measuring the dark voltage of the photodiodes. Figure 4.10 shows the voltage for the three arms when the beam is blocked. For each curve, the average over the time taken by the laser to sweep the wavelength is computed and subtracted from the corresponding arm signal. After subtracting the dark

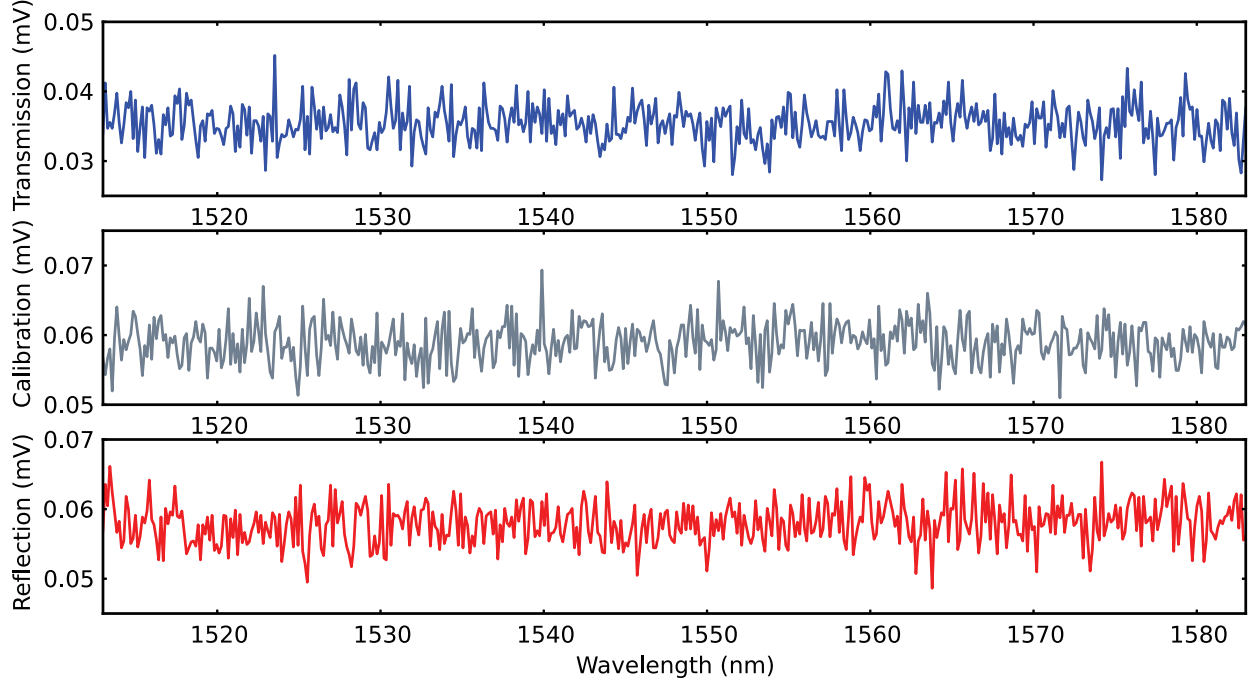


Figure 4.10: Dark voltage from the photodiodes in the transmission arm (blue), calibration arm (gray), and reflection arm (red).

voltage, taking the ratio of the transmission arm signal to the calibration arm signal yields

$$\frac{A_{PhC} + A_{PhC}^{45}}{C_{PhC} + C_{PhC}^{45}} = \frac{\{\mathcal{I}(t_1, \lambda) + \mathcal{I}(t_2, \lambda)\} \times BS_A(\lambda) \times L_2(\lambda) \times T(\lambda) \times L_3(\lambda) \times PD(\lambda, R_A) + \mathcal{N}_A(t_1) + \mathcal{N}_A(t_2)}{\{\mathcal{I}(t_1, \lambda) + \mathcal{I}(t_2, \lambda)\} \times BS_C(\lambda) \times \mathcal{A}(\lambda) \times L_1(\lambda) \times PD(\lambda, R_C) + \mathcal{N}_C(t_1) + \mathcal{N}_C(t_2)}. \quad (4.9)$$

Similarly,

$$\frac{A_{empty} + A_{empty}^{45}}{C_{empty} + C_{empty}^{45}} = \frac{\{\mathcal{I}(t_3, \lambda) + \mathcal{I}(t_4, \lambda)\} \times BS_A(\lambda) \times L_2(\lambda) \times L_3(\lambda) \times PD(\lambda, R_A) + \mathcal{N}_A(t_3) + \mathcal{N}_A(t_4)}{\{\mathcal{I}(t_3, \lambda) + \mathcal{I}(t_4, \lambda)\} \times BS_C(\lambda) \times \mathcal{A}(\lambda) \times L_1(\lambda) \times PD(\lambda, R_C) + \mathcal{N}_C(t_3) + \mathcal{N}_C(t_4)}. \quad (4.10)$$

For clarity, rewriting Eqs. 4.9 and 4.10 with $\alpha = \{\mathcal{I}(t_1, \lambda) + \mathcal{I}(t_2, \lambda)\} \times BS_A(\lambda) \times L_2(\lambda) \times T(\lambda) \times L_3(\lambda) \times PD(\lambda, R_A)$, and β, γ, ζ accordingly gives:

$$\frac{A_{PhC} + A_{PhC}^{45}}{C_{PhC} + C_{PhC}^{45}} = \frac{\alpha + \mathcal{N}_A(t_1) + \mathcal{N}_A(t_2)}{\beta + \mathcal{N}_C(t_1) + \mathcal{N}_C(t_2)}, \quad (4.11)$$

$$\frac{A_{empty} + A_{empty}^{45}}{C_{empty} + C_{empty}^{45}} = \frac{\gamma + \mathcal{N}_A(t_3) + \mathcal{N}_A(t_4)}{\zeta + \mathcal{N}_C(t_3) + \mathcal{N}_C(t_4)}. \quad (4.12)$$

Assuming that the signal to noise is large, $\frac{\mathcal{N}_A(t_1)+\mathcal{N}_A(t_2)}{\alpha} \ll 1$ (and similarly for corresponding quantities), taking the ratio of Eqs. 4.11 and 4.12 and keeping only leading order terms, one obtains

$$\frac{A_{PhC} + A_{PhC}^{45}}{C_{PhC} + C_{PhC}^{45}} \times \frac{C_{empty} + C_{empty}^{45}}{A_{empty} + A_{empty}^{45}} = \frac{\alpha}{\beta} \frac{\zeta}{\gamma} \times \left(1 + \frac{\mathcal{N}_A(t_1) + \mathcal{N}_A(t_2)}{\alpha} + \frac{\mathcal{N}_C(t_3) + \mathcal{N}_C(t_4)}{\zeta} - \frac{\mathcal{N}_C(t_1) + \mathcal{N}_C(t_2)}{\beta} - \frac{\mathcal{N}_A(t_3) + \mathcal{N}_A(t_4)}{\gamma} \right). \quad (4.13)$$

Notice that $\frac{\alpha}{\beta} \frac{\zeta}{\gamma} = T(\lambda)$, and (ignoring noise) we have recovered the transmission of just the PhC membrane. Now, terms like $\frac{\mathcal{N}_A(t_1)+\mathcal{N}_A(t_2)}{\alpha}$ go to zero in two limits. Firstly, one can time average. For example, this is done to some extent by the built-in amplifier in the LabJack. One can also record several voltages in a given time window for each wavelength step, and take the average of that bin. Secondly, terms like $\mathcal{N}_A(t_1) + \mathcal{N}_A(t_2)$ add proportionally to \sqrt{N} whereas terms like α add proportionally to N , where N is the number of times a signal of the form $A_{PhC} + A_{PhC}^{45}$ is recorded. Therefore, one can repeat the same measurement several times, or equivalently make the measurement at several half-wave plate angles. Consequently, Eq. 4.13 is a good approximation to the PhC membrane's transmission spectrum $T(\lambda)$ when the noise terms are made small using the techniques mentioned above.

To obtain the PhC membrane's reflection spectrum $R(\lambda)$, the same treatment is applied to the voltage signal recorded in the reflection arm (designated by the letter B). Effectively, this amounts to replacing the A 's by B 's in the above equations. However, it is important to note that B_{empty} is not the voltage from the reflection arm in the absence of a PhC membrane, but the voltage from the reflection arm in the presence of a mirror. The non-perfect reflectivity of the mirror is taken into account by dividing B_{empty} by the average reflectivity of the mirror (97 %) over the investigated bandwidth [62]. The following section shows the results for $T(\lambda)$ and $R(\lambda)$.

4.4 Transmission Spectrum of Photonic Crystal Membranes

In this section, we report on the optical characterization of our devices. In Sec. 4.4.1, we present the transmission spectrum of a hexagonal slab, and analyze discrepancies between our measurement and our simulation. Then, we demonstrate tuning of the spectral position

of the PhC's resonance in Sec. 4.4.2. Finally, we discuss the preliminary reflection spectrum of one of our devices in the Appendix.

4.4.1 Hexagonal Slab

Figure 4.11 shows the transmission spectrum of a hexagonal slab, which was our first sample displaying a pronounced transmission dip, thus establishing the presence of a guided resonance near 1517 nm. This sample also confirmed that the spectral position and shape of the measured resonance matches reasonably well with simulation. However, the transmission dip does not go as low as the simulation predicts. This type of discrepancy has been observed

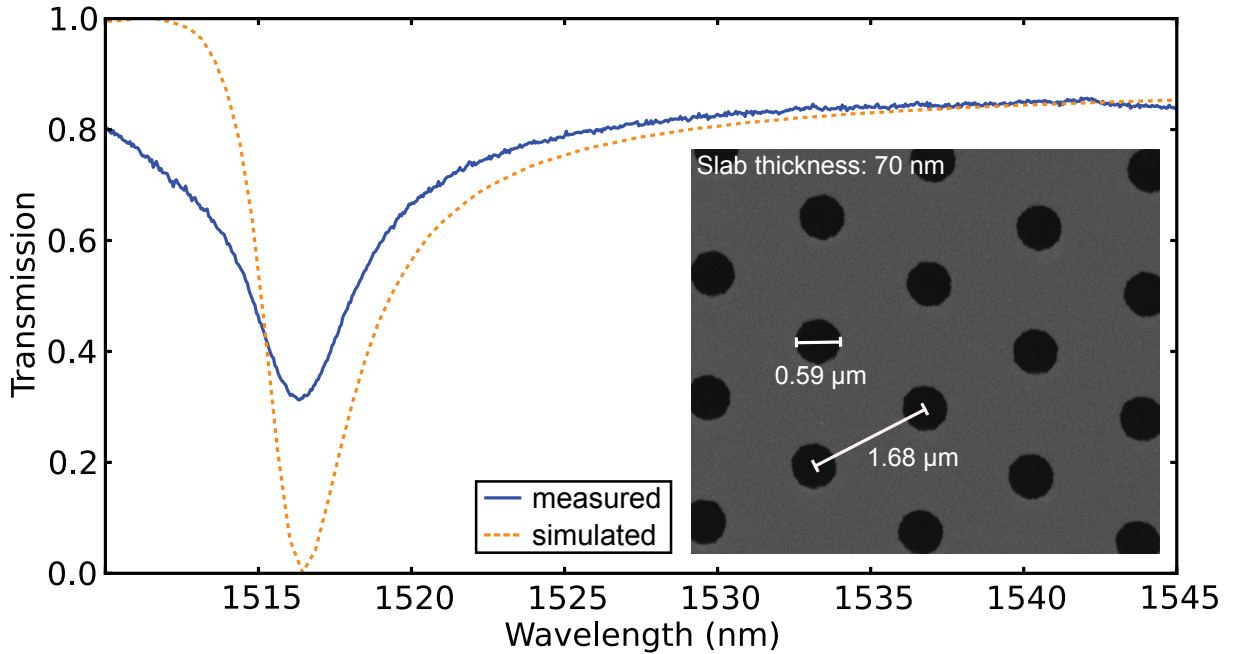


Figure 4.11: Measured (blue) and simulated (gold) normal incidence transmission spectrum of a hexagonal slab. The inset shows the fabricated device.

before [27, 28, 38], and is attributed to three factors. First, fabrication related disorder tends to average out guided resonances in PhC membranes [26, 57], increasing the linewidth of the resonance and decreasing its depth. In particular, guided resonances are found to be robust against disorder in the hole radius and roughness, but extremely sensitive to disorder in the lattice periodicity [30, 35, 38]. A sample typically display deviations of $\sim 1\%$ in the lattice constant. Second, the simulations assume plane wave illumination, whereas the experiment is carried out with focused-beam illumination. For our setup, the angular spread of the Gaussian beam is given by [14] $\theta_0 = \frac{2}{\pi} \frac{\lambda}{w_0} \simeq 1^\circ$, where w_0 is the beam spot size at the PhC

membrane. Previous work show that a few degree angular spread of the Gaussian beam results into shallower depths in the guided resonances [35]. Third, the investigated guided resonance is very sensitive to the incident angle of illumination, as shown in Fig. 4.6, and confirmed by Ref. [28]. In particular, we did not observe a sharp transition between high and low-transmission regions of the membrane, which is what would be expected for $w_0 = 60 \mu\text{m}$ and a $200 \times 200 \mu\text{m}^2$ PhC. We believe that the combination of these three factors is responsible for the broadening and shallower depth of the resonance.

For the measurement shown in Fig. 4.11, the polarization of the light is along \hat{y} , with the coordinates defined as in Fig. 2.4. We did not investigate other polarizations since the sample was lost after this measurement. At that point in time, we developed the ability to fabricate a square lattice geometry by thinning the membrane. As discussed in Sec. 2.2.1, the square lattice is polarization independent and defeats the need to align the lattice with the polarization vector to achieve the lowest possible transmission. In the next section, we present our results for tuning the spectral position of the resonance of a square lattice PhC membrane.

4.4.2 Resonance Tuning

Immersing a PhC membrane in HF acid simultaneously thins the membrane and widens the holes. As discussed in Sec. 2.3.1.3, this has the effect of displacing the PhC's resonance toward smaller wavelengths. Therefore, PhC membranes are intentionally fabricated with parameters that yield a resonance at $\lambda \simeq 1565 \text{ nm}$. This way, it is possible to approach the target wavelength $\lambda = 1550 \text{ nm}$ by subsequently dipping the device in HF acid, and measuring its transmission spectrum, as shown in Fig. 4.12. This figure represents the main result of this thesis, which is our ability to tune the location of the resonance in the vicinity of 1550 nm. The shift associated with the resonance is not constant, and varies between ~ -4.4 and $\sim -8.2 \text{ nm/min}$ for the measurements (solid curves) shown. Furthermore, the linewidth of the measured resonance decreases with time spent in HF acid ($\gamma = \{4.51, 4.36, 3.80, 3.55\} \text{ nm}$), an observation predicted in Sec. 2.3.1.3. In all cases, the linewidth of the measured resonance is $\sim \times 1.7$ greater than the simulated one (dashed curve), and the depth of the resonance does not go below 0.32. This is ascribed to the factors discussed in Sec. 4.4.1. In addition, there is an offset between the simulated and measured spectral positions of the resonance. This could be explained by the extreme sensitivity of the resonance to the membrane thickness ($t = \{66, 61, 59, 57\} \text{ nm}$), and the uncertainty associated with the measurement of

the membrane thickness. Using this method, we approached our target wavelength to ~ 0.2 nm. In the next paragraph, we examine the implications of this result in the context of the membrane-in-the-middle setup discussed in Sec. 1.2.

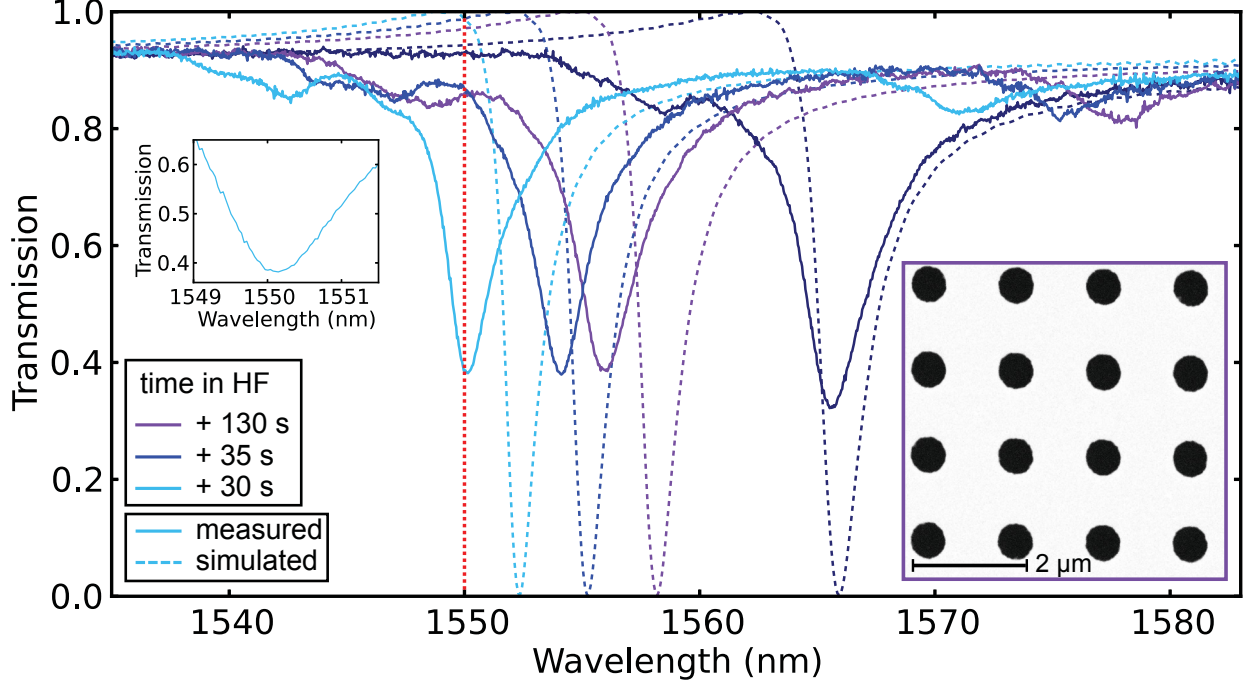


Figure 4.12: Measured (solid) and simulated (dashed) transmission spectrum of a square lattice PhC membrane successively immersed in HF acid to tune the spectral position of the resonance. The left inset shows that the resonance occurs ~ 0.2 nm away from our target wavelength (indicated by the red vertical dashed line). The right inset shows the fabricated device at the stage of the purple curve.

Assuming negligible absorption by the SiN membrane [19, 25, 44], the cyan curve corresponds to a reflectivity $|r_{PhC}|^2 \simeq 0.62$ at $\lambda = 1550$ nm. Away from the resonance, the spectrum coincides to that of an unpatterned membrane [33] with a reflectivity $|r_m|^2 \simeq 0.1$. From Eqs. 1.15 and 1.16, this yields a $\times 2.5$ improvement for the linear optomechanical coupling (when the membrane is away from a node or antinode), and a $\times 4$ improvement for the quadratic optomechanical coupling (when the membrane sits at an antinode).

Finally, we present a preliminary reflection spectrum in the Appendix. At the moment, we do not believe that this measurement is an accurate description of our sample's reflectivity. For reasons discussed in the Appendix, this measurement motivates the migration from

the current experimental setup to a cavity-based setup to extract a better estimate of the PhC membrane's reflection spectrum. A possible approach is to use the membrane-in-the-middle configuration [25] so that the PhC membrane's reflectivity can be determined from the cavity's frequency dependence to the membrane's position (see Fig. 1.2), small losses can be more readily inferred from cavity finesse measurements, and it is the actual environment in which it is expected to perform. An alternative approach is to form an optical cavity with a curved mirror and to use the PhC membrane as the other mirror [24]. For this configuration, the waist of the cavity mode (i.e. where light behaves the most as plane waves) naturally occurs at the PhC membrane. Knowing the reflectivity of the curved mirror, the PhC membrane's reflectivity can be obtained from a finesse measurement.

Chapter 5

Conclusions and Outlook

In this work we demonstrated a gentle and predictable technique for tuning the spectral position of a guided resonance supported in PhC membranes. Using this technique, we tuned the resonance within ~ 0.2 nm of our target wavelength. This method relaxes the stringent requirements of fabrication by allowing one to iteratively tune the location of the resonance after the PhC has been patterned into the membrane.

We designed the PhC membranes via numerical simulations, where we examined the square and hexagonal lattice geometries. We investigated the effects of structural tuning on the guided resonance, which led us to consider HF acid as a method to thin the SiN membrane and widen the holes of the PhC. Based on the results of the simulations, we developed a successful process flow to fabricate SiN PhC membranes.

At the moment, our experimental setup allows for the determination of the spectral position of the resonance, but does not provide a good estimate of the reflectivity of the PhC membrane. The next step is to construct a cavity-based setup to better characterize the reflection spectrum of our devices, and potentially perform optomechanics experiments with them. As we proceed, we will continue to optimize the electron beam lithography parameters and dry etching recipe used to define the PhC into the membrane, and carry out a deeper analysis than that of Sec. 2.3.1.4 for material absorption. We also envisage to use silicon to fabricate a high-reflectivity disc to explore the cavity enhanced torsional levitation predicted by our group [10]. Ultimately, all directions pursued by our group (see Sec. 1.2) will benefit from our work.

Appendix

Reflection Spectrum

Figure A.1a shows the reflection spectrum of a sample displaying a resonance near 1550 nm. The striking feature is that the loss ($1 - R - T$) is relatively high near the resonance. This cannot be solely attributed to the absorption of the ultra-thin SiN membrane near 1550 nm [19,25,44]. Moreover, fabrication related disorder should not be responsible for this loss. Indeed, as mentioned in Sec. 4.4.1, guided resonances are tolerant to roughness [30,35,38], and our sample displays a similar roughness to Refs. [35,38]. Therefore, it is unlikely that scattering yields such a high loss. At the moment, we do not understand this behavior, and speculate that it is related to our setup. For this reason, we are planning to instead perform a cavity-based measurement, as discussed in Sec. 4.4.2.

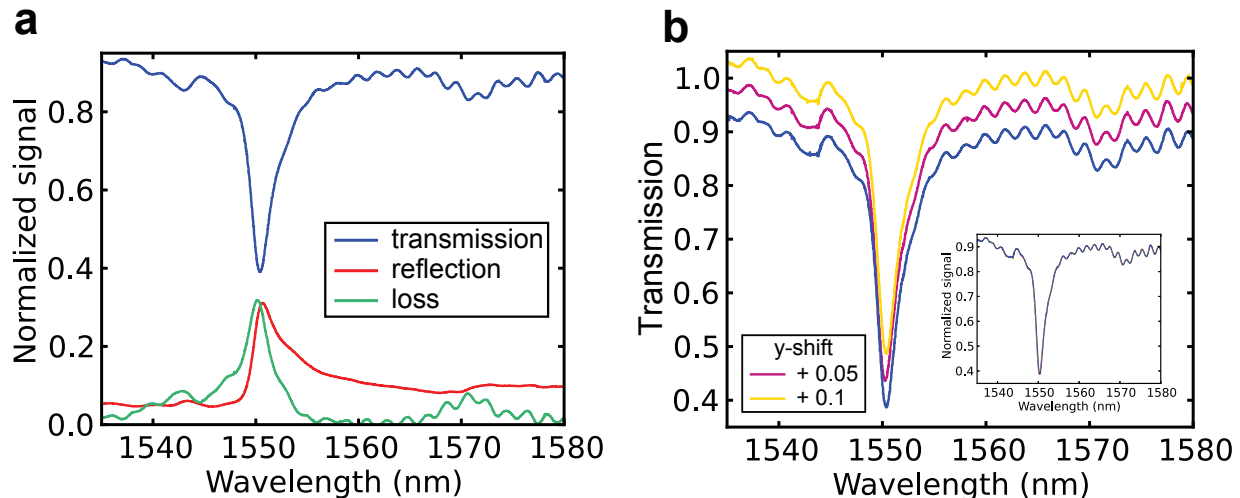


Figure A.1: **a**, Measured transmission, reflection, and loss ($1 - T - R$) of a square lattice PhC membrane displaying a resonance near $\lambda = 1550$ nm. The loss is higher than what we expect, and we plan to perform a measurement with a cavity-based setup to obtain a better estimate of the PhC membrane's reflectivity. **b**, Repeated measurement of the transmission. The overlapping of the curves suggest that the modulation is due to laser drift (see details below).

Another feature of Fig. A.1a is the modulation in the transmission curve. This modulation is absent for the curves plotted in Figs. 4.11 and 4.12. The measurement in Fig. A.1a took place over a longer period of time in an attempt to improve the signal to noise ratio

by taking several spectra with different half-wave plate angles, and increasing the number of steps taken by the laser. Although this method did improve the signal to noise ratio, it introduced a modulation that is likely due to laser drift (apparent in Fig. 4.2c). To support this lead, Fig. A.1b shows a measurement that was carried out in the following manner: the signal in the presence of a PhC membrane was recorded three times (each time corresponds to a different curve) in a short interval of time, whereas the signal in the absence of a PhC membrane was recorded the next day. Obtaining the transmission spectrum involves taking the ratio of these two signals (see Sec. 4.3). The overlapping of the curves suggests that the laser drifted overnight, bringing the two signals slightly out of phase to produce a modulation. The reflection curve in Fig. A.1a does not display this modulation because the signal without a PhC membrane (i.e. with a mirror, see Sec. 4.3) was taken right before the signal in the presence of a PhC membrane.

Bibliography

- [1] M. Aspelmeyer, T. J. Kippenberg, and F. Marquardt, *Cavity optomechanics*, Rev. Mod. Phys. **86** (2014), 1391–1452. [1](#), [2](#), [6](#)
- [2] T. J. Kippenberg and K. J. Vahala, *Cavity Optomechanics: Back-Action at the Mesoscale*, Science **321** (2008), no. 5893, 1172–1176. [1](#)
- [3] J. D. Teufel, T. Donner, D. Li, J. W. Harlow, M. S. Allman, K. Cicak, A. J. Sirois, J. D. Whittaker, K. W. Lehnert, and R. W. Simmonds, *Sideband cooling of micromechanical motion to the quantum ground state*, Nature **475** (2011), 359–363. [1](#)
- [4] J. Chan, T. P. Mayer Alegre, A. H. Safavi-Naeini, J. T. Hill, A. Krause, S. Gröblacher, M. Aspelmeyer, and O. Painter, *Laser cooling of a nanomechanical oscillator into its quantum ground state*, Nature **478** (2011), 89–92. [1](#)
- [5] A. Ashkin, J. M. Dziedzic, J. E. Bjorkholm, and S. Chu, *Observation of a single-beam gradient force optical trap for dielectric particles*, Opt. Lett. **11** (1986), no. 5, 288–290. [1](#)
- [6] D. E. Chang, C. A. Regal, S. B. Papp, D. J. Wilson, J. Ye, O. Painter, H. J. Kimble, and P. Zoller, *Cavity opto-mechanics using an optically levitated nanosphere*, Proc. Nat. Acad. Sci. **107** (2010), no. 3, 1005–1010. [1](#)
- [7] T. Li, S. Kheifets, D. Medellin, and M. G. Raizen, *Measurement of the instantaneous velocity of a brownian particle*, Science **328** (2010), no. 5986, 1673–1675. [1](#)
- [8] D. E. Chang, K. K. Ni, O. Painter, and H. J. Kimble, *Ultrahigh-Q mechanical oscillators through optical trapping*, New J. Phys. **14** (2012), no. 4, 045002. [1](#)
- [9] K. K. Ni, R. Norte, D. J. Wilson, J. D. Hood, D. E. Chang, O. Painter, and H. J. Kimble, *Enhancement of Mechanical Q Factors by Optical Trapping*, Phys. Rev. Lett. **108** (2012), 214302. [1](#), [6](#), [8](#)
- [10] T. Müller, C. Reinhardt, and J. C. Sankey, *Enhanced optomechanical levitation of minimally supported dielectrics*, Phys. Rev. A **91** (2015), 053849. [1](#), [8](#), [43](#), [65](#)

- [11] K. Stannigel, P. Rabl, A. S. Sørensen, P. Zoller, and M. D. Lukin, *Optomechanical Transducers for Long-Distance Quantum Communication*, Phys. Rev. Lett. **105** (2010), 220501. [2](#)
- [12] C. A. Regal and K. W. Lehnert, *From cavity electromechanics to cavity optomechanics*, Journal of Physics: Conference Series **264** (2011), no. 1, 012025. [2](#)
- [13] Y.-D. Wang and A. A. Clerk, *Using Interference for High Fidelity Quantum State Transfer in Optomechanics*, Phys. Rev. Lett. **108** (2012), 153603. [2](#)
- [14] B. E. A. Saleh and M. C. Teich, *Fundamentals of Photonics*, Second ed., Wiley, 2007. [2](#), [47](#), [61](#)
- [15] F. Marquardt and S. M. Girvin, *Optomechanics*, Physics **40** (2009), no. 2. [6](#)
- [16] T. Corbitt, Y. Chen, E. Innerhofer, H. Müller-Ebhardt, D. Ottaway, H. Rehbein, D. Sigg, S. Whitcomb, C. Wipf, and N. Mavalvala, *An All-Optical Trap for a Gram-Scale Mirror*, Phys. Rev. Lett. **98** (2007), 150802. [6](#)
- [17] J. D. Thompson, B. M. Zwickl, A. M. Jayich, F. Marquardt, S. M. Girvin¹, and J. G. E. Harris, *Strong dispersive coupling of a high-finesse cavity to a micromechanical membrane*, Nature **452** (2008), 72–75. [7](#), [9](#)
- [18] A. M. Jayich, J. C. Sankey, B. M. Zwickl, C. Yang, J. D. Thompson, S. M. Girvin, A. A. Clerk, F. Marquardt, and J. G. E. Harris, *Dispersive optomechanics: a membrane inside a cavity*, New J. Phys. **10** (2008), no. 9, 095008. [7](#), [8](#)
- [19] J. C. Sankey, C. Yang, B. M. Zwickl, A. M. Jayich, and J. G. E. Harris, *Strong and tunable nonlinear optomechanical coupling in a low-loss system*, Nat. Phys. **6** (2010), 707–712. [9](#), [17](#), [25](#), [63](#), [66](#)
- [20] F. Elste, S. M. Girvin, and A. A. Clerk, *Quantum Noise Interference and Backaction Cooling in Cavity Nanomechanics*, Phys. Rev. Lett. **102** (2009), 207209. [9](#)
- [21] T. Chen and X.-B. Wang, *Fast cooling in dispersively and dissipatively coupled optomechanics*, Scientific Reports **5** (2015), 7745. [9](#)
- [22] A. Xuereb, C. Genes, and A. Dantan, *Strong Coupling and Long-Range Collective Interactions in Optomechanical Arrays*, Phys. Rev. Lett. **109** (2012), 223601. [9](#)

- [23] M. Ludwig, B. Kubala, and F. Marquardt, *The optomechanical instability in the quantum regime*, New J. Phys. **10** (2008), no. 9, 095013. [9](#)
- [24] U. Kemiktarak, M. Durand, M. Metcalfe, and J. Lawall, *Cavity optomechanics with sub-wavelength grating mirrors*, New J. Phys. **14** (2012), no. 12, 125010. [9](#), [10](#), [64](#)
- [25] C. Stambaugh, H. Xu, U. Kemiktarak, J. Taylor, and J. Lawall, *From membrane-in-the-middle to mirror-in-the-middle with a high-reflectivity sub-wavelength grating*, arXiv:1407.1709 (2014). [9](#), [10](#), [17](#), [63](#), [64](#), [66](#)
- [26] O. Kilic, S. Kim, W. Suh, Y. A. Peter, A. S. Sudbo, M. F. Yanik, S. H. Fan, and O. Solgaard, *Photonic crystal slabs demonstrating strong broadband suppression of transmission in the presence of disorders*, Opt. Lett. **29** (2004), no. 23, 2782–2784. [9](#), [18](#), [61](#)
- [27] V. Lousse, W. Suh, O. Kilic, S. Kim, O. Solgaard, and S. H. Fan, *Angular and polarization properties of a photonic crystal slab mirror*, Opt. Express **12** (2004), no. 8, 1575–1582. [9](#), [18](#), [61](#)
- [28] C. H. Bui, J. Zheng, S. W. Hoch, L. Y. T. Lee, J. G. E. Harris, and C. W. Wong, *High-reflectivity, high-Q micromechanical membranes via guided resonances for enhanced optomechanical coupling*, Appl. Phys. Lett. **100** (2012), 021110. [10](#), [13](#), [18](#), [25](#), [61](#), [62](#)
- [29] O. Kilic, M. Dignonnet, G. Kino, and O. Solgaard, *External fibre Fabry–Perot acoustic sensor based on a photonic-crystal mirror*, Measurement Science and Technology **18** (2007), no. 10, 3049. [10](#)
- [30] W. Suh, M. F. Yanik, O. Solgaard, and S. Fan, *Displacement-sensitive photonic crystal structures based on guided resonance in photonic crystal slabs*, Appl. Phys. Lett. **82** (2003), no. 13, 1999–2001. [10](#), [61](#), [66](#)
- [31] J. D. Joannopoulos, S. G. Johnson, J. N. Winn, and R. D. Meade, *Photonic crystals: Molding the flow of light*, Second ed., Princeton University Press, 2008. [10](#), [15](#), [25](#)
- [32] S. G. Johnson, S. Fan, P. R. Villeneuve, J. D. Joannopoulos, and L. A. Kolodziejski, *Guided modes in photonic crystal slabs*, Phys. Rev. B **60** (1999), 5751–5758. [10](#)
- [33] S. Fan and J. D. Joannopoulos, *Analysis of guided resonances in photonic crystal slabs*, Phys. Rev. B **65** (2002), 235112. [10](#), [13](#), [20](#), [21](#), [27](#), [63](#)

- [34] S. Fan, W. Suh, and J. D. Joannopoulos, *Temporal coupled-mode theory for the Fano resonance in optical resonators*, J. Opt. Soc. Am. A **20** (2003), no. 3, 569–572. [10](#), [27](#)
- [35] K. Crozier, V. Lousse, O. Kilic, S. Kim, S. Fan, and O. Solgaard, *Air-bridged photonic crystal slabs at visible and near-infrared wavelengths*, Phys. Rev. B **73** (2006), no. 11, 115126. [10](#), [13](#), [20](#), [21](#), [25](#), [27](#), [61](#), [62](#), [66](#)
- [36] R. Harbers, S. Jochim, N. Moll, R. F. Mahrt, D. Erni, J. A. Hoffnagle, and W. D. Hinsberg, *Control of Fano line shapes by means of photonic crystal structures in a dye-doped polymer*, Appl. Phys. Lett. **90** (2007), no. 20. [10](#)
- [37] T. Antoni, A. G. Kuhn, T. Briant, P. Cohadon, A. Heidmann, R. Braive, A. Beveratos, I. Abram, L. Le Gratiet, I. Sagnes, and I. Robert-Philip, *Deformable two-dimensional photonic crystal slab for cavity optomechanics*, Opt. Lett. **36** (2011), no. 17. [13](#)
- [38] T. Prasad, V. L. Colvin, and D. M. Mittelman, *Dependence of guided resonances on the structural parameters of terahertz photonic crystal slabs*, J. Opt. Soc. Am. B **25** (2008), no. 4, 633–644. [13](#), [20](#), [21](#), [23](#), [61](#), [66](#)
- [39] N. Ou, J. H. Shyu, H. M. Lee, and J. C. Wu, *Diameter-dependent guided resonance of dielectric hole-array membrane*, J. Vac. Sci. Technol. B **27** (2009), 3183. [13](#)
- [40] A. F. Oskooi, D. Roundy, M. Ibanescu, P. Bermel, J. D. Joannopoulos, and S. G. Johnson, *MEEP: A flexible free-software package for electromagnetic simulations by the FDTD method*, Comput. Phys. Commun. **181** (2010), 687–702. [13](#), [14](#), [15](#), [16](#), [19](#)
- [41] Meep Introduction - AbInitio, Accessed 05 May 2015, http://ab-initio.mit.edu/wiki/index.php/Meep_Introduction. [14](#), [15](#), [16](#), [17](#)
- [42] A. Taflove, *Computational Electrodynamics: The Finite-Difference Time-Domain Method*, First ed., Artech House, 1995. [14](#)
- [43] Yee lattice - AbInitio, Accessed 08 May, 2015, http://ab-initio.mit.edu/wiki/index.php/Yee_lattices. [14](#), [15](#)
- [44] D. J. Wilson, C. A. Regal, S. B. Papp, and H. J. Kimble, *Cavity Optomechanics with Stoichiometric SiN Films*, Phys. Rev. Lett. **103** (2009), no. 20, 207204. [17](#), [63](#), [66](#)
- [45] Z. X. Qiang, H. J. Yang, L. Chen, H. Q. Pang, Z. Q. Ma, and W. D. Zhou, *Fano filters based on transferred silicon nanomembranes on plastic substrates*, Appl. Phys. Lett. **93** (2008), 061106. [18](#)

- [46] S. J. Orfanidis, *Introduction to signal processing*, Prentice Hall, 1996. 18
- [47] Meep Reference - AbInitio, Accessed 16 June, 2015, http://ab-initio.mit.edu/wiki/index.php/Meep_Reference. 18
- [48] Meep Tutorial - AbInitio, Accessed 16 June, 2015, http://ab-initio.mit.edu/wiki/index.php/Meep_Tutorial. 19
- [49] V. A. Mandelshtam and H. S. Taylor, *Harmonic inversion of time signals*, J. Chem. Phys. **107** (1997), no. 17, 6756–6769. 19, 25
- [50] P. E. Barclay, K. Srinivasan, O. Painter, B. Lev, and H. Mabuchi, *Integration of fiber-coupled high- Q SiN_x microdisks with atom chips*, Appl. Phys. Lett. **89** (2006), 131108. 23
- [51] Materials in Meep - AbInitio, Accessed 25 June, 2015, http://ab-initio.mit.edu/wiki/index.php/Conductivity_in_Meep. 24
- [52] Harminv - AbInitio, Accessed 24 June, 2015, <http://ab-initio.mit.edu/wiki/index.php/Harminv>. 25
- [53] S. Franssila, *Introduction to microfabrication*, Second ed., John Wiley & Sons, 2010. 29, 33
- [54] B. D. Pant and U. S. Tandon, *Etching of Silicon Nitride in CCl_2F_2 , CHF_3 , SiF_4 , and SF_6 Reactive Plasma: A Comparative Study*, Plasma Chemistry and Plasma Processing **19** (1999), no. 4, 545–563. 32
- [55] Y. Kondo, K. Ishikawa, T. Hayashi, Y. Miyawaki, K. Takeda, H. Kondo, M. Sekine, and M. Hor, *Silicon nitride etching performance of CH_2F_2 plasma diluted with argon or krypton*, Japanese Journal of Applied Physics **54** (2015), 040303. 32
- [56] Raith, *NanoSuite Software Reference*. 36, 37
- [57] T. Prasad, V. L. Colvin, and D. M. Mittleman, *The effect of structural disorder on guided resonances in photonic crystal slabs studied with terahertz time-domain spectroscopy*, Opt. Express **15** (2007), no. 25, 16954. 38, 61
- [58] Artisan Technology Group, *Model 6300 User's Manual: The Velocity Tunable Diode Laser*, New Focus. 44, 48

- [59] Thorlabs, *PAF-X-7-C specifications sheet*. [45](#)
- [60] Thorlabs, *SM05PD4A specifications sheet*. [46](#), [47](#)
- [61] H. Kogelnik and T. Li, *Laser beams and resonators*, Appl. Opt. **5** (1966), no. 10, 1550–1567. [47](#)
- [62] Thorlabs, *PF10-03-P01 specifications sheet*. [60](#)